Jesse K. Mee

Candidate

Electrical Engineering

Department

This dissertation is approved, and it is acceptable in quality
and form for publication:

Approved by the Dissertation Committee:

Luke Lester, Chairperson

Daniel Feezell

Ganesh Balakrishnan

Jean-Claude Diels

_____

_____

_____

_____

_____

TIME DOMAIN CHARACTERIZATION OF MONOLITHIC QUANTUM DOT PASSIVELY MODE-LOCKED LASERS

by

JESSE K. MEE

B.S., Electrical Engineering, University of New Mexico, USA, 2009
M.S., (*distinction*) Electrical Engineering, University of New Mexico, USA, 2010

DISSERTATION

Submitted in Partial Fulfillment of the
Requirements for the Degree of

**Doctor of Philosophy
Engineering**

The University of New Mexico
Albuquerque, New Mexico

July, 2013

<u>DEDICATION</u>

I dedicate this work to my wife Hannah, my son Trevor, and my daughter Lillian.

ACKNOWLEDGEMENT

I would like to extend my deepest appreciation to my committee chair professor, Dr. Luke F. Lester. His encouragement and guidance has greatly assisted my professional development, throughout the duration of this study. The work presented in this dissertation would not have been possible without his extraordinary effort.

I would also like to thank my committee members, Dr. Daniel Feezell, Dr. Ganesh Balakrishnan, and Dr. Jean-Claude Diels. Their valuable recommendations and insightful comments greatly assisted in completion of this dissertation.

Additionally, I am grateful to Dr. Mark Crowley, Ravi Raghunathan, David Murrell, Nishant Patel, Jeremy Write, Dr. Alexandre Braga and Dr. Antonio Hurtado for their valuable assistance with conceptual understanding and experimental development. I gratefully acknowledge Dr. Hua Li for supplying the devices used in this dissertation. I would like to especially thank my friends and colleagues at the Air Force Research Lab for their continuous support through the duration of my graduate studies.

Finally, I would like to thank my wife Hannah for her unfailing support and sacrifice over these years, and my children Trevor and Lillian who bring me so much joy.

**TIME DOMAIN CHARACTERIZATION OF MONOLITHIC
QUANTUM DOT PASSIVELY MODE-LOCKED LASERS**

by

Jesse K. Mee

B.S., Electrical Engineering, University of New Mexico, 2009

M.S., (*distinction*) Electrical Engineering, University of New Mexico, 2010

Ph.D., Engineering, University of New Mexico, 2013

ABSTRACT

Passively mode-locked lasers based on InAs/GaAs quantum dots have benefited from the unique properties pertaining to this material system, leading to the demonstration of wide mode-locking operational maps, and reconfigurable repetition rates, as well as low rms timing jitter. Applications of these passively mode-locked lasers include optical clock distribution, the generation of RF signals and high bit rate optical time division multiplexing. In addition to their utility for terrestrial applications, quantum dot mode-locked lasers have the strong potential to support applications in intra-satellite data transmission. Owing to their compact size and low power consumption properties, coupled with the potential to achieve enormous aggregate bandwidth from a single transmitter, desirable size, weight and power (SWaP) metrics can be achieved while simultaneously

increasing the capacity. Supporting applications in space data transmission architectures requires a strong understanding of the evolution of the device characteristics over a broad range of operating conditions. The temperature-dependent operation of a passively mode-locked laser typically relies on the mutual interdependence of the saturable absorber and amplifying gain section in a two-section device, and therefore it is not readily apparent how these devices will perform over broad temperature excursions.

In this dissertation, a detailed study is presented on a series of quantum dot passively mode-locked lasers with variable absorber to gain-section length ratios. Inputs into an analytical model used for predicting regions of mode-locking stability for a given cavity geometry, are derived from measurements of modal gain and absorption on a multi-section single pass emitter. The effects of temperature on the operational range of pulses emitted from the quantum dot ground and excited states are experimentally examined on a set of two-section mode-locked lasers having variable absorber lengths. A comparison is drawn between the experimental observations and the analytical model predictions. It is found that the model correctly predicts the temperature of maximum operability in each of the devices studied for a variety of absorber voltages. Prediction of the regimes of excited-state operation from the quantum dots is also included and experimentally verified. The quality of pulse generation from pure ground-state operation, pure excited-state operation and a simultaneous lasing of ground and excited states is examined. For the first time, the unsaturated absorption is identified as a key parameter that strongly influences the range of biasing conditions that produce stable mode-locked pulses. This is shown to be directly responsible for improvement in mode-locking characteristics at elevated temperature; a previously observed effect that was not well understood.

Finally, while the range of pulsed operation from a semiconductor mode-locked laser can be determined using a digital sampling oscilloscope or an auto-correlator, true verification of mode-locking stability requires simultaneous measurements of the temporal and frequency domains. In this dissertation we examine device characteristics with a Frequency Resolved Optical Gating (FROG) pulse measurement system. This allows for direct measurement of pulse asymmetry and chirp. This measurement technique is used to examine the evolution of device characteristics with increasing temperature, whereby the time bandwidth product over temperature is studied. Additionally, FROG is used to examine a regime of operation where non-linear double pulsing occurs (two pulses per round trip). It is shown for the first time that the observed double pulsing is in fact a stable effect, thus mode-locked operation at twice the fundamental repetition rate can be reliably achieved by simply electrically biasing the device in the appropriate manner. This data set offers valuable insight into to design of future mode-locked laser devices for maximum optical pulse quality over a large range of temperature and biasing conditions. Furthermore, the results are promising for the development of temperature-insensitive pulsed sources for uncooled applications such as data multiplexing and optical clocking; this is particularly attractive for space applications as active cooling consumes a large portion of the power budget.

TABLE OF CONTENTS

LIST OF FIGURES

LIST OF TABLES

Chapter 1 – Introduction

1.1 The History of Quantum Dot Semiconductor Lasers

Coherent light from a semiconductor material was first demonstrated in 1962 by Hall *et. al.* [1] in a GaAs p-n junction. Shortly after, Holonyak *et. al.* [2], demonstrated visible coherent emission at a slightly shorter wavelength in a $GaAs_{1-x}P_x$ p-n junction. Owing to their homostructure design, these legacy demonstrations had very poor radiative recombination efficiency as there was no means of confining the carriers to the active region. In wasn't until the late 1960's, when Alferov *et. al.* [3], and Hayashi *et. al.* [4] developed the Double Heterostructure (DH) laser, that continuous wave operation at room temperature was achieved in a semiconductor laser. The DH forms potential barriers on both sides of the p-n junction that limits the distance over which minority carriers can diffuse, thus improving the electrical confinement as well as optical confinement by virtue of the refractive index step between the center and outer layers.

In 1974, Dingle *et. al.* demonstrated discrete quantum levels associated with the confinement of carriers in a very thin AlGaAs-GaAs-AlGaAs heterostructure [5]. As the dimensions of the active region are reduced, the electrons are confined in one dimension and freely move in the other two dimensions. This causes the density of states function to exhibit step-like discrete transitions, compared to the continuous transitions associated with a bulk semiconductor; this is often called the quantum size effect. This acts to improve the carrier confinement thus increasing the efficiency of radiative recombination. In 1978, the first quantum well laser was demonstrated by Dupuis *et. al* [6], who used the technique of metal-organic chemical vapor deposition (MOCVD) to grow quantum wells as thin as

20 nm. In 1979, Tsang *et. al.* [7] demonstrated a multiple quantum well laser grown with molecular-beam epitaxy (MBE). This laser had a threshold current density of 2 kA/cm^2. By 1981, a threshold current density as low as 250 A/cm^2 had been demonstrated in a quantum well laser [8].

In 1982, Arakawa and Sakai published the first theory of the quantum dot laser [9]. Therein, they proposed and analyzed a new type of laser, which they called the multidimensional (2D or 3D) quantum well (MD-QW), as an extension of the conventional quantum well lasers. In this new laser the dimensionality of the free-electron motion was decreased from 2D (quantum well), to 1D (quantum wire) or 0D (quantum dot) [9], as a means of reducing the temperature sensitivity of the threshold current density. It would be more than 10 years before the first quantum dot lasers were demonstrated. In 1994, Leonard *et. al.* [10] demonstrated a method to grow high density quantum dots in a semiconductor. The method exploited the compressive strain of MBE-deposited InGaAs on GaAs to induce a transition from the two-dimensional growth mode to the three-dimensional growth mode. Petroff *et. al.* [11] extended this to include InP/InGaP structures with MBE and MOCVD growth techniques. In August of 1994, the first quantum dot lasers where reported [12] with fully quantized energy levels in both bands and a strongly inhomogeneously-broadened gain spectrum. Due to un-optimized growth conditions this first quantum dot laser had a threshold current density of 980 A/cm^2 at room temperature. By the early 2000's, a group at the University of New Mexico that was developing optimized quantum dot growth techniques, had reduced the threshold current density to around 10 A/cm^2 [13,14] using the "dots-in-a-well" or DWELL structure. Finally, in May of 2001 the first

quantum dot passively mode-locked laser was demonstrated [15]. Pulse widths of 17 ps were observed at a repetition rate of 7.4 GHz. Since then, pulse characteristics have been considerably improved through optimization of growth conditions, cavity geometry and waveguide geometry design. Never-the-less, there is still much to learn about the relative impact of temperature and current excursion on the mode-locking stability, as well as the physical mechanisms that influence the measured pulse characteristics.

1.2 <u>Background and Motivation</u>

In recent years increasing challenges in electronic charge transport due to electro-magnetic interference effects, fundamental limitations of capacity, and increased power dissipation have led to the investigation of integrating photonics into the backplane of high-speed communication network architectures [16-18]. This realization has fueled competition between different lasers structures aimed at determining which technology possesses the most superior properties to support these high-speed applications. Although quantum well devices are considered to be at the forefront of this discussion, structures based on quantum dots actually possess many superior properties over their quantum well counterparts. These include low linewidth enhancement factor [19], low threshold current densities, wide gain bandwidth, easily saturated gain and absorption, and temperature-resistant operation [20-22]; each of these will be discussed in detail in section 1.4. As a result, generation of ultra-short, ultra-high repetition rate, optical pulses have been demonstrated in mode-locked lasers based on quantum dot materials [23,24]. Some of the particular advantages of these quantum dot mode-locked lasers include their compact size, lower power consumption, broad operational maps, and improved temperature operation

[25]. These attributes have attracted considerable attention in the space electronics community. Satellite missions are often tightly constrained by their power budget. At the same time mission payloads, such as hyper-spectral imagers for example, can produce 10's of Gbps of uncompressed data [26]. The maturity of the quantum dot mode-locked laser technology to the point of integration with the data transmission architecture on a satellite could represent a significant reduction in the size, weight, and power (SWaP), while simultaneously improving the capacity. In addition, these devices have the potential to support many terrestrial applications from high bit rate optical time division multiplexing (OTDM) for use in data center network architectures [27], to the generation of tunable microwave signals [28].

The directly-modulated Vertical Cavity Surface Emitting Laser (VCSEL) is currently capable of reliably delivering ~25 Gb/s of bandwidth [29,30], and the path toward ~40 Gb/s is actively being pursued [30]. Alternatively, there are unique properties pertaining to quantum dot mode-locked lasers that could potentially allow them to outperform state-of-the-art VCSEL technology in terms of SWaP performance for equivalent capacity. One particular advantage is related to the in-plane geometry of the two-section lasers, which makes them favorable for integration with silicon photonics. The potential to achieve high capacity from a single, efficient transmitter is strongly supported by the prospects of combining the mode-locked laser with silicon photonics. The optical output from the laser can be focused into a silicon-based waveguide wherein optical time division multiplexing (OTDM) and wavelength division multiplexing (WDM) techniques, combined with efficient electro-optical modulators, can be realized to achieve large

aggregate bandwidths from a single efficient transmitter [27,31-33]. In Fig. 1-1 the OTDM/WDM hybrid architecture is captured schematically, and is shown to achieve an aggregate bandwidth of 200 Gb/s from a single 5 Gb/s source [31]. In this illustration, the optical pulsed output is divided into 10 different paths, each with a different delay. The delayed signals are then recombined resulting in an increase in the optical repetition rate by the number of original paths; 10X in this case. Furthermore, given the wide inhomogenousely broadened gain bandwidth, a characteristic of the quantum dot medium [34,35], the aggregate capacity can be increased by dividing the optical 3-dB bandwidth into multiple channels each having different wavelength. These channels can be modulated exclusive of one another. In Fig. 1-1, four-channels of wavelength selection is accomplished using 3 μm diameter ring resonators. These act as the wavelength filters for the different WDM channels [31]. Overall, a final aggregate bandwidth of 200 Gb/s can be achieved from the 5 Gb/s source. The advantage of this approach in comparison to the directly modulated VCSEL approach is related to scalability. The projected critically-damped 3-dB bandwidth of the 980 nm VCSEL is around 60 GHz [36]. By integrating the quantum dot mode-locked laser with silicon photonics, the limit to the bandwidth is not related to how fast the carrier signal can be modulated, but rather to the wavelength separation between adjacent WDM channels, and the repetition rate of the optical pulse train after OTDM. This enables un-matched capability and offers an efficient means of data transmission with scalable capacity to support the growing demand on bandwidth in future systems.

One of several objectives of this dissertation is to explore the regimes of operation where narrow pulse generation occurs, and to examine methods for improving optical pulse

characteristics though various biasing schemes. This study directly impacts the aforementioned OTDM/WDM hybrid architecture as the optical pulse Full Width Half Maximum (FWHM) determines the upper-limit of the pulse repetition rate that can be achieved through OTDM. Consequently, improvements in optical pulse quality increase the potential to achieve high aggregate bandwidth from the transmitter.
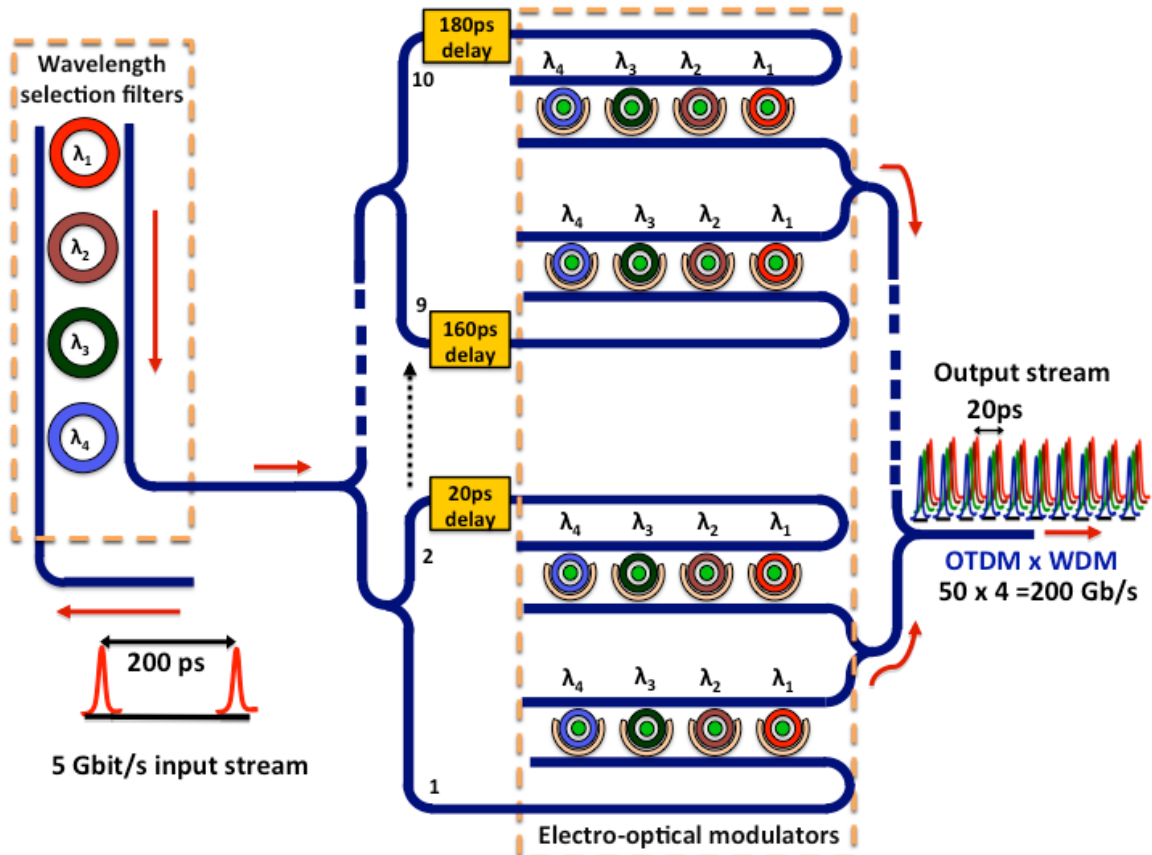
Figure 1-1. Optical time division multiplexing/wavelength division multiplexing hybrid architecture. This architecture enables 200 Gb/s aggregate capacity from a single efficient 5 Gb/s source. [31]

1.3 <u>Passive Mode-Locking in a Semiconductor Laser</u>

Mode-locking occurs when a stable phase relationship is established between adjacent longitudinal cavity modes; this produces an equidistant pulse train with a period defined by the round trip time inside the laser cavity. The generated optical pulse train can be on the order of picoseconds to femtoseconds [37]. Mode-locking of adjacent transverse modes to create a scanning laser beam has also been explored but is not within the scope of this dissertation [38]. There are many different techniques for locking the phase of the axial cavity modes, all of which fall into one of two categories, active mode-locking or passive mode-locking.

a. Active mode-locking

Active mode-locking techniques are externally driven. These methods introduce sinusoidal loss or phase modulations into the laser cavity at a period given by the cavity round trip time [37]. A common technique for active mode-locking involves placing an acousto-optic modulator within the cavity. By driving the modulator with the appropriate signal, a standing acoustic wave is generated within the modulator at a frequency that is equal to the cavity mode spacing. As the laser light passes through the modulator, the acoustic wave deflects the light and imparts side bands on the optical signal with frequency spacing equal to the cavity mode spacing. These sidebands, which correspond to adjacent cavity modes, are now phase-locked to the center mode. As this beam is reflected back into the cavity, it stimulates the emission of identical photons with equal phase. When the photons at the frequency of the sidebands enter the modulator, they incur another frequency

shift corresponding to the next adjacent mode. This continues until all axial cavity modes are locked in phase.

b. *Passive mode-locking in a semiconductor laser*

In contrast to active mode-locking, passive mode-locking techniques do not require an external RF signal, but rather depend on the amplitude variations of the photons within the laser cavity to induce changes in the absorption and gain properties within the gain medium [37-40]. The devices used in this dissertation are passively mode-locked semiconductor lasers. Passive mode-locking within a semiconductor laser is achieved through the use on an intra-cavity element called the saturable absorber. In Fig. 1-2 the schematic of the elements within the cavity of the passively mode-locked laser is shown. The absorber and gain dynamics that lead to optical pulse generation are also shown in Fig.1-2 [39]. The saturable absorber applies selective loss to optical emission as a function of optical intensity. Passive mode-locking begins with a spontaneous emission event that has enough energy to match the saturation fluence of the saturable absorber. This will bleach the absorber and consequently the energetic light will be more efficiently amplified on each round trip through the cavity. The unique gain and absorption dynamics of the quantum dot material strongly affect the pulse characteristics of the mode-locked laser. As the leading edge of the optical pulse enters the absorber, the absorption quickly saturates and drops below the gain. However, within 60 to 300 fs the excited carriers begin to thermalize and this leads to partial recovery of the absorber [40]. As seen in Fig. 1-2, this results in a narrow net gain window wherein amplification can occur and cavity losses can be offset. As the absorption recovers the trailing edge of the pulse is trimmed leading to

9

the typical "fast leading edge" – "slow trailing edge" pulse shape. In chapter 5, the effects of varying absorber and gain recovery dynamics will be used to explain different observed pulse shapes.
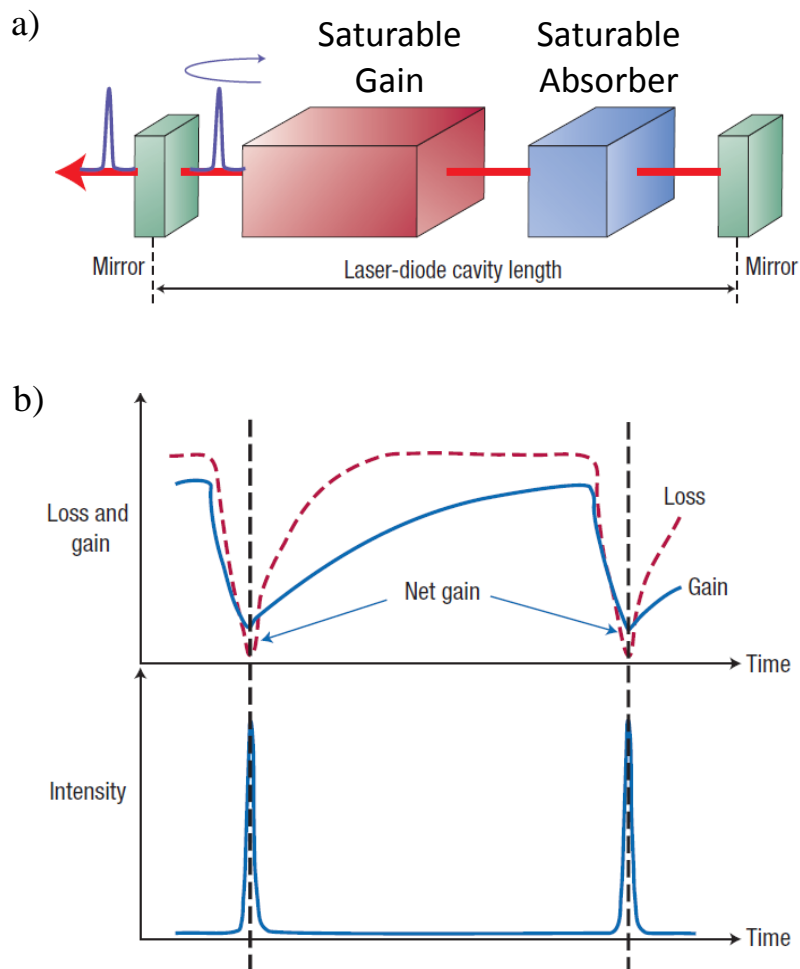
Figure 1-2. Passive mode-locking in semiconductor laser diode. (a) Illustration of the saturable absorber section (blue), gain section (red), and facet mirrors (green). (b) Gain and loss dynamics that occur when the high intensity pulse enters the saturable absorber. [39]

1.4 <u>Advantages of Quantum Dots</u>

In terms of favorable properties for mode-locking, quantum dots have a significant advantage over their quantum well counterparts. In this section the advantages of quantum dots are outlined and discussed. As described above the efficiency of the pulse trimming mechanisms in passive mode-locking are highly related to absorber and gain saturation and recovery times. A prerequisite requirement for the net gain window discussed in Fig. 1-2 is that the absorption must saturate more rapidly than the gain. Accordingly, the ratio of the saturation energy of the gain section to that of the absorber section must be greater than 1. This forms the commonly cited stability parameter given by [41]:

$$S = \frac{E_{sat,g}}{E_{sat,a}} = \left(N_{tr} \Gamma \frac{dg}{dN} \right)^{-1} > 1$$

(1-1)

where $E_{sat,g}$ is the saturation energy of the gain section, $E_{sat,a}$ is the saturation energy of the absorber section, N_{tr} is the transparency carrier density, Γ is the optical confinement factor and dg/dN is the differential gain with respect to carrier density. From Eqn. (2-1) it is seen that low optical confinement factor, low transparency carrier density and low differential gain are desirable for passive mode-locking. In Fig. 1-3 the normalized modal gain as versus carrier density is given for quantum dot, quantum well and bulk material systems [42]. For a given carrier density the quantum dot material system is shown to have the highest values of modal gain. Additionally, owing to the finite reduced density of states in the quantum dot per unit area, the modal gain strongly saturates with increasing carrier density. This leads to low values of differential gain (dg/dN) as the maximum gain value

of the quantum dot medium is approached. These factors considered, quantum dots are clearly prime candidates for stable pulse generation according to Eqn. (2-1). There are a number of other attributes related to the quantum dot material system that make it highly for generation of optical pulses. Those were briefly mentioned in section 1.2 but are restated in more detail below.
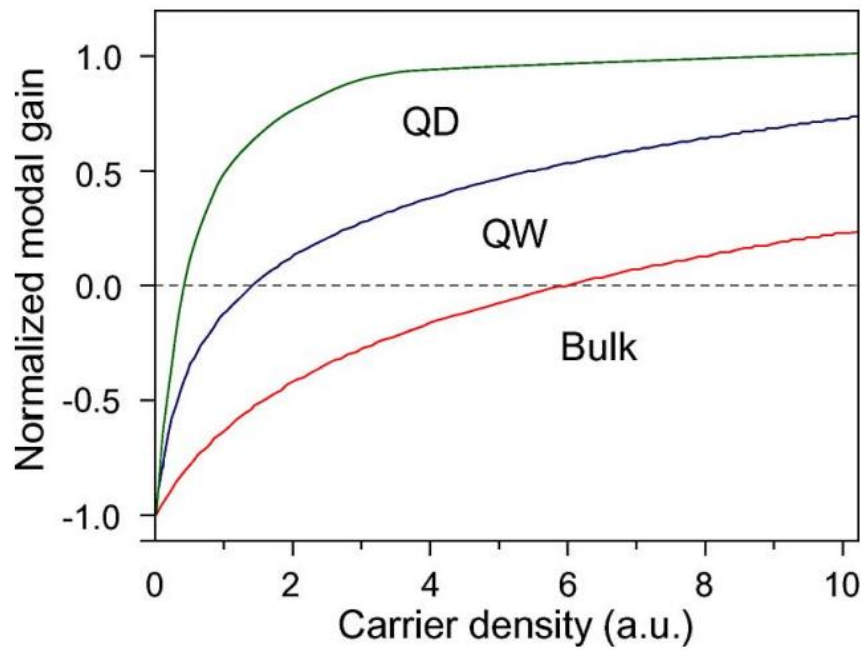
Figure 1-3. Normalized modal gain versus carrier density, in bulk (red), quantum well (blue) and quantum dot (green) material systems [42].

a. Fast gain and absorber dynamics

As mentioned to above, owing to the reduced density of states, quantum dots have *lower saturation fluence* than quantum well devices. Additionally, *ultra fast absorber recovery times* have been demonstrated [43,44]. Absorber recovery times from 62 ps, with 0 V applied to the absorber, to 700 fs, with -10V applied to the absorber have been measured [44]. From Fig. 1-2, it was shown that the leading edge of the pulse is strongly dependent on the absorption saturation time, while the absorber recovery time is the mechanism by which the trailing edge of the pulse is trimmed. It then follows that the ultra fast gain and absorber dynamics associated with quantum dots are very advantageous for narrow pulse generation and ultimately mode-locking stability.

b. Low (or negative) linewidth enhancement factor

The linewidth of a laser results from fluctuations in the phase of the optical field arising from spontaneous emission events that alter the phase and intensity of the laser emission [45]. One of the desirable characteristics associated with quantum dots is the observation of *low linewidth enhancement factors*. The linewidth enhancement factor, often called the α-parameter, depends on the ratio of the change in the real part of the refractive index with respect to carrier density (*dn/dN*) to the differential gain (*dg/dN*) of the material α=-4π/λ(dn/dN)(dg/dN)$^{-1}$ [45]. In theory, the refractive index will not change with increasing carrier density at the peak of a symmetric gain profile with energy [46,47]. This follows from the Kramers-Kronig relation. In a quantum dot medium, strong symmetry of the gain spectrum results from the δ-like density of states, thus the refractive index change is small with increasing carrier density. Furthermore, the differential gain in

13

a quantum dot is very high prior to gain saturation. These factors considered, near zero α-parameters have been demonstrated in quantum dot lasers [48]. These values are significantly less than those measured in quantum well devices. This is an important feature as high values of α can lead to a number of undesirable effects such as self-focusing and chirp under modulation [48]. There have been also been studies that showed negative α-parameter [49] is achievable. This stimulates the idea of intra-cavity chirp compensation, which can potential improve time domain characteristics of the mode-locked laser. This will be discussed in the future work section of chapter 6.

c. Low threshold current density

Ultra-low threshold current density arises from the small physical volume of the active region coupled with the reduced density of states resulting from 3 dimensions of carrier confinement. Because of the tight confinement of carriers, the probability of radiative recombination is high. Additionally, there are fewer carriers required for population inversion. These factors act to significantly reduce the threshold current density. Operation at lower values of forward injection current offers advantages such as lower spontaneous emission noise and lower power consumption.

d. Potential for Temperature Insensitive Operation

Finally, the *temperature insensitive* properties of quantum dots make them very attractive candidates for uses in satellite optical interconnect applications where wide temperatures excursions are present. The temperature sensitivity of a semiconductor laser is often expressed by its characteristic temperature, T_o. The exponential of the ratio T/T_o

14

describes the empirically observed temperature dependence of the threshold current of the laser. Accordingly, low values of T_o indicate there will be strong variation in the threshold current over temperature. The temperature insensitive properties of quantum dots result from discrete nature of the density of states. T_o values as high as 650 K have been reported in high power 1.3 μm quantum dot lasers [50].

1.5 <u>Dissertation Objectives and Organizational Structure</u>

Supporting terrestrial and space applications alike, it is expected that the quantum dot mode-locked lasers will need to operate reliably over a variety of environmental conditions. The objective of this dissertation is to develop analytical and experimental capabilities in order to gain a clearer understanding of the physical mechanisms that influence the efficiency of stable pulse generation in a quantum dot mode-locked laser, and to examine biasing techniques that can be utilized to optimize the optical pulsed output. This ultimately supports the transition of this technology, either for terrestrial applications, or applications within a satellite. In particular, we focus on understanding and improving the *time-domain* pulse characteristics of two-section quantum-dot passively mode-locked lasers operating over broad temperature excursions and biasing conditions.

In chapter 2 (*Devices and Fabrication*), the details of the quantum dot mode-locked lasers used throughout the dissertation are given. Therein, the cavity geometry, ridge waveguide geometry and the epitaxial structure of the devices are presented and discussed in detail. In chapter 3 (*Analytical Model of the Mode-Locking Stability)*, an analytical model is discussed and shown to enable accurate prediction of the regions where mode-

locking stability is expected to occur as a function of the device cavity geometry. The strength of this approach lies in the fact that all the parameters appearing in the analytic expressions can be measured; namely, the static gain and loss characteristics. The segmented contact method [51] is utilized to measure the loss and gain spectra over a wide temperature range up to 120 ℃ and over a wide range of gain-section current and saturable absorber section reverse voltages. This comes as a prerequisite to examining the experimental operational range of the two-section lasers. The theoretical range of mode-locked operation is given for each of the devices used in this dissertation across the full range of examined temperatures. In chapter 4 (*Experimental Study of the Operational Range*), the construction of the experimental operational maps is given. These maps represent the range biasing conditions where the laser exhibits narrow pulse generation as measured by a high speed digital sampling oscilloscope. The maps are generated for the set of devices having different absorber to gain length ratios, and compared to the predictions of the analytical model discussed in chapter 3. It is shown that excellent agreement between experimental results and analytical theory is achieved. In chapter 5 (*The Evolution of Device Performance with Increasing Temperature and Current*), the influence of temperature-dependent unsaturated absorption on the optical pulse width is discussed Additionally, in this chapter the stability of the mode-locked lasers is examined with frequency resolved optical gating (FROG) pulse measurements. This method is used to study the evolution of the pulse time-bandwidth product for increasing temperature, as well as the double pulsing effect; a common non-linearity that can occur within these semiconductor mode-locked lasers. Lastly, in chapter 5 the waveguide geometry and its relative impact on the effective current density and ultimately the range of pulsed operation

16

is discussed. Chapter 6 (*Conclusion and Future Work*), is the final chapter of this dissertation. Here the key results from this study are restated and the future work is presented. This includes the development of the experimental methodology for the three-section mode-locked laser wherein differential pumping of two electrically isolated gain sections can be used to improve the time-domain characteristics of the mode-locked laser.

REFERENCES FOR CHAPTER 1

[1] R.N.Hall, G.E.Fenner, et al, "Coherent Light Emission From GaAs Junctions" Phys. Rev. Lett. 9,366, 1962

[2] N. Holonyak, Jr. and S. F. Bevacqua, "Coherent (visible) light emission from a (As1-xPx) junctions," Appl. Phys. Lett., vol 1, pp. 82-83 (1962).

[3] Z. I. Alferov, V. M. Andreev, V. I. Korol'kov, E. L. Portnoi, and D.N. Tret'yakov, "Injection properties of n-Al Ga As-p-GaAs hetero-junctions", Fiz. Tekh. Poluprovodn., vol. 2, pp. 1016 1017, 1968. Sov. Phys.-Semicond., vol. 2, p. 843-844, (1969)

[4] I. Hayashi, M. B. Panish, P. W. Foy, and S. Sumski, "Junction lasers which operate continuously at room temperature" Appl. Phys. Lett., vol.17, pp. 109-111, (1970)

[5] R. Dingle, W. Wiegmann, and C. H. Henry, "Quantum States of Confined Carriers in Very Thin $Al_xGa_{1-x}As$-GaAs-$Al_xGa_{1-x}As$ Heterostructures," Phys. Rev. Lett. vol. 33, pp. 827 – 830 (1974).

[6] R. D. Dupuis, P. D. Dapkus, N. Holonyak Jr., E. A. Rezek, R. Chin, "Room Temperature operation of quantum-well Ga1-xAlxAs-GaAs laser diodes grown by metalorganic chemical vapor deposition," Appl. Phys. Lett. vol. 32, pp. 295-297 (1978).

[7] W. T. Tsang, C. Weisbuch, R. Miller, R. Dingle, "Current Injection GaAs-AlxGa1-XAs Multi-Quantum-Well Heterostructure Lasers Prepared By Molecular-Beam epitaxy"Applied Physics Letters , vol. 35, no. 9 pp. 673-675, (1979)

[8] W. T. Tsang, "Extremely low threshold (AlGa)As modified multiquantum well heterostructure lasers grown by molecular-beam epitaxy," Appl. Phys. Lett. vol. 39, pp. 786-788 (1981)

[9] Y. Arakawa, and H. Sakaki, "Multidimensional quantum well laser and temperature dependence of its threshold current", Appl. Phys Lett., 40 (11), 939-941, 1982

[10] Leonard, D., Fafard, S., Pond, K., Zhang, Y. H., Merz, J. L., And Petroff, P. M., "Structural And Optical-Properties Of Self-Assembled Ingaas Quantum Dots," Journal Of Vacuum Science & Technology B, Vol. 12, No. 4, Pp. 2516-2520, (1994)

[11] Petroff, P. M. And Denbaars, S. P., "Mbe And Mocvd Growth And Properties Of Self-Assembling Quantum-Dot Arrays In Iii-V Semiconductor Structures," Superlattices And Microstructures, Vol. 15, No. 1, Pp. 15-21, (1994)

[12] N. Kirstaedter, N. N. Ledentsov, M. Grundmann, D. Bimberg, V. M. Ustinov, S. S. Ruvimov, M. V. Maximov, P. S. Kopev, Z. I. Alferov, U. Richter, P. Werner, U. Gosele, and J. Heydenreich, "Low-Threshold, Large T_0 Injection-Laser Emission From (InGa)As Quantum Dots," Electronics Letters, vol. 30, no. 17, pp. 1416-1417 (1994)

[13] Eliseev, P.G.; Li, H.; Stintz, A.; Liu, G. T.; Newell, T.C.; Malloy, K.J.; Lester, L.F., "Transition dipole moment of InAs/InGaAs quantum dots from experiments on ultralow-threshold laser diodes," Applied Physics Letters , vol.77, no.2, pp.262-264 (2000)

[14] Stintz, A.; Liu, G. T.; Li, H.; Lester, L.F.; Malloy, K.J., "Low-threshold current density 1.3-μm InAs quantum-dot lasers with the dots-in-a-well (DWELL) structure," Photonics Technology Letters, IEEE , vol.12, no.6, pp.591-593 (2000)

[15] Huang, Xiaodong; Stintz, A.; Li, Hua; Lester, L.F.; Cheng, Julian; Malloy, K.J., "Passive mode-locking in 1.3 μm two-section InAs quantum dot lasers," Applied Physics Letters , vol.78, no.19, pp.2825-2827 (2001)

[16] J. A. Davis, R. Venkatesan, A. Kaloyeros, M. Beylansky, S. J. Souri, K. Banerjee, K. C. Saraswat, A. Rahman, R. Reif, and J. D. Meindl, "Interconnect limits on gigascale integration (GSI) in the 21st century" Proc. IEEE, vol. 89, pp. 305–324 (2001)

[17] M. Haurylau, C. Q. Chen, H. Chen, J. D. Zhang, N. A. Nelson, D. H. Albonesi, E. G. Friedman, and P. M. Fauchet, B, "On-chip optical interconnect roadmap: Challenges and critical directions" IEEE J. Sel. Topics Quantum Electron., vol. 12, no. 6, pp. 1699-1705 (2006)

[18] Miller, D., "Device Requirements for Optical Interconnects to Silicon Chips," Proc. IEEE, vol. 97, no.7, pp. 1166-1185 (2009)

[19] A. Martinez, J. Provost, A. Lemaitre, O. Gautier-Lafaye, B, Dagens, K. Merghem, L. Ferlazzo, C. Dupuis, D. Le Gouezigou, A. Ramdane, "Static and dynamic measurements of the Henry factor of 5-quantum dot layer single mode lasers emitting at 1.3 μm on GaAs," Lasers and Electro-Optics, vol.3, no., pp. 1659- 1661 (2005)

[20] G.T. Liu, A. Stintz, H. Li, K.J. Malloy and L.F. Lester, "Extremely low room-temperature threshold current density diode lasers using lnAs dots in InGaAs quantum well" Elect. Lett., vol. 35, pp. 1163-1165, (1999)

[21] D. G. Deppe, H. Huang, and O. B. Shchekin, "Modulation characteristics of quantum-dot lasers: The influence of p-type doping and the electronic density of states on obtaining high speed," IEEE J. Quan. Elect., vol. 38, no. 12, pp. 1587–1593 (2002)

[22] M. T. Crowley, N. A. Naderi, H. Su, F. Grillot and L. F. Lester "GaAs-based Quantum Dot Lasers in Semiconductors and Semimetals" 86, Chapter 10: Advances in Semiconductor Lasers (New York: Academic, 2012)

[23] MG Thompson, AR Rae, M. Xia, RV Penty, and IH White, "InGaAs Quantum-Dot Mode-Locked Laser Diodes," IEEE J. Sel. Top. Quan. Elect., 15, 661–672 (2009)

[24] Y. Li, L. Furqan, Y-C Chiragh, C-Y Lin, K. Junghoon, C. Christodoulou, and L. F. Lester, "Harmonic mode-locking using the double interval technique in quantum dot lasers" Optics Express, vol. 18, Issue 14, pp. 14637-14643 (2010)

[25] J. K. Mee, M. T. Crowley, N. Patel, D. Murrell, R. Raghunathan, A. Aboketaf, A. Elshaari, S. F. Preble, P. Ampadu, and L. F. Lester, "A passively mode-locked quantum-dot laser operating over a broad temperature range" App. Phys. Lett. vol.101, no.7, pp.071112-1 − 071112-4 (2012)

[26] R. Wright, P. G. Lucey, K. A. Horton, M. Wood, H. Garbeil, and S. T. Crites. "The Thermal Hyperspectral Imager (THI): an instrument for remote sensing of Earth's surface from a micro-satellite platform" American Geophysical Union, SA31A-1946 (2011)

[27] A. Aboketaf, A. W. Elshaari, and S. F. Preble, "Optical time division multiplexer on silicon chip" Opt. Express 18, 13529-13535 (2010)

[28] A. Hurtado, J. K. Mee, M. Nami, I. D. Henning, M. J. Adams, and L. F. Lester, "Tunable microwave signal generator with an optically-injected 1310nm QD-DFB laser," Optics Express, vol. 21, no. 9, pp. 10772-10778 (2013)

[29] R. Safaisini, K. Szczerba, E. Haglund, P. Westbergh, J. S. Gustavsson, A. Larsson P. A. Andrekson, "22 Gb/s error-free data transmission beyond 1 km of multi-mode fiber using 850 nm VCSELs," Proc. SPIE Vertical-Cavity Surface-Emitting Lasers XVII, 86390T (2013)

[30] L. Karachinsky, S A Blokhin, I I Novikov, N A Maleev, G Kuzmenkov, M A Bobrov, J A Lott, N N Ledentsov, V A Shchukin, J-R Kropp, and D Bimberg "Reliability performance of 25 Gbit/s 850 nm vertical-cavity surface-emitting lasers," Semicond. Sci. Technol. vol. 28 pp. 065010 (2013)

[31] A. A. Aboketaf, L. Cao, D. Adams, A. W. Elshaari, S. F. Preble, M. T. Crowley, L. F. Lester and P. Ampadu, "Hybrid OTDM and WDM for multicore optical communication," IGCC, pp.1-5, (2012)

[32] L. Arissian and J-C. Diels, "A mode-locked laser as a combined radio-frequency and optical clock, stabilized to a reference cavity, and calibrated through coherent interaction with rubidium," SPIE vol. 483-161, pp. 161 (2002)

[33] Ladan Arissian and Jean-Claude Diels. Mode-locked laser as a combined radio-frequency and optical clock, stabilized to a reference cavity, and calibrated through coherent interaction with rubidium. SPIE Applications of Photonic Technology 6, vol. 5260-82, pp. 1-10, (2003)

[34] L. F. Lester, A. Stintz, H. Li, T. C. Newell, E. A. Pease, B. A. Fuchs, K. J. Malloy, "Optical characteristics of 1.24-μm InAs quantum-dot laser diodes," Photonics Technology Letters, IEEE , vol.11, no.8, pp.931-933 (1999)

[35] S W Osborne, P Blood, PM Smowton, Y C Xin, A Stintz, D Huffaker, and L F Lester, "Optical absorption cross-section of quantum dots," J. Phys. Condens. Matter, vol. 16, no. 35, pp. 3749-3756 (2004)

[36] K. L. Lear, A. N. Al-Omari, "Progress and issues for high-speed vertical cavity surface emitting lasers," Proc. SPIE 6484, Vertical-Cavity Surface-Emitting Lasers XI, 64840J (2007)

[37] H. A. Haus, "Mode-locking of lasers," Selected Topics in Quantum Electronics, IEEE Journal of , vol.6, no.6, pp.1173,1185, (2000)

[38] D. Auston, "Transverse mode locking," Quantum Electronics, IEEE Journal of , vol.4, no.6, pp.420-422 (1968)

[39] E. U. Rafailov, M. A. Cataluna and W. Sibett, "Mode-Locked quantum-dot laser" Nature Photonics, 1, 399, (2007)

[40] U. Keller, "Recent developments in compact ultrafast lasers," Nature, vol. 424, pp. 831-838 (2003).

[41] P. Vasil'ev, Ultrafast Diode Lasers: Fundamentals and Applications. Boston: Artech House, (1995).

[42] Thompson, M.G.; Rae, A.R.; Mo Xia; Penty, R.V.; White, I.H., "InGaAs Quantum-Dot Mode-Locked Laser Diodes," Selected Topics in Quantum Electronics, IEEE Journal of , vol.15, no.3, pp.661-672 (2009)

[43] P. Borri, S. Schneider, W. Langbein, and D. Bimberg, "Ultrafast carrier dynamics in InGaAs quantum dot materials and devices," J. Opt. A, vol. 8, pp. S33-S46 (2006).

[44] D. B. Malins, A. Gomez-Iglesias, S. J. White, W. Sibbett, A. Miller, and E. U. Rafailov, "Ultrafast electroabsorption dynamics in an InAs quantum dot saturable absorber at 1.3 μm," Appl. Phys. Lett., vol. 89, pp. 171111 (2006).

[45] C. H. Henry, "Theory of the Lindwidth of Semiconductor lasers," IEEE J. Quantum. Electronics. vol. QE18, no. 2 pp. 259-264 (1982)

 [46] Schneider, S., Borri, P., Langbein, W., Woggon, U., Sellin, R. L., Ouyang, D., and Bimberg, D., "Linewidth enhancement factor in InGaAs quantum-dot amplifiers," IEEE Journal of Quantum Electronics, vol. 40, no. 10, pp. 1423-1429 (2004)

[47] Saito, H.; Nishi, Kenichi; Kamei, A.; Sugou, Shigeo, "Low chirp observed in directly modulated quantum dot lasers," Photonics Technology Letters, IEEE , vol.12, no.10, pp.1298-1300 (2000)

[48] T. C. Newell, D. Bossert, A. Stintz, B. Fuchs, K. J. Malloy, and L. F. Lester, "Gain And Linewidth Enhancement Factor In InAs Quantum Dot Laser Diodes," IEEE Photon. Technol. Lett. 11, 1527 (1999)

[49] A. V. Uskov, E. P. O'Reilly, D. McPeake, N. N. Ledentsov, D. Bimberg, and G. Huyet, "Carrier-induced refractive index in quantum dot structures due to transitions from discrete quantum dot levels to continuum states," Appl. Phys. Lett., vol. 84, pp. 272–274 (2004)

[50] S. S. Mikhrin, A. R. Kovsh, I. L. Krestnikov, A. V. Kozhukhov, D. A. Livshits, N. N. Ledentsov, Yu. M. Shernyakov, I. I. Novikov, M. V. Maximov, V. M. Ustinov and Zh. I. Alferov, "High power temperature-insensitive 1.3 μm InAs/InGaAs/GaAs quantum dot lasers," Semicond. Sci. Technol. vol. 20, no. 5, pp. 340 (2005)

[51] Y.-C.Xin, Y. Li, A. Martinez, T. J. Rotter, H. Su, L. Zhang, A. L. Gray, S. Luong, K. Sun, Z. Zou, J. Zilko, P. M. Varangis, and L. F. Lester, "Optical gain and absorption of QD measured using an alternative segmented contact method" IEEE J. Quantum Electron. 42, 725 (2006)

Chapter 2 – Devices and Fabrication

In this chapter, the details of the quantum dot mode-locked lasers used throughout this dissertation are given. Sections 2.1 and 2.2 of this chapter describe the active layer composition and cavity geometry of the two-section mode-locked lasers and the multi-section single pass emitter, respectively. In chapter 3, the multi-section single pass emitter will be used to gather modal gain and absorption characteristics which serve as the primary inputs into an analytical model used for predicting operational capability for a given cavity geometry. In chapter 4, the two-section mode-locked lasers will be used for development of the experimental operational maps, and in chapter 5 they will be characterized with Frequency Resolved Optical Gating (FROG), which is a sensitive measurement of mode-locked stability. In the final section of this chapter, the impact of the effective current density on the threshold current density is calculated and experimentally examined.

2.1 Two-Section QD Mode-Locked Laser

The laser structures presented here were grown on a GaAs substrate by molecular beam epitaxy (MBE). The epitaxial cross-section for the growth of the laser structure is shown in Fig. 2-1. A complete description of the refractive index in each layer is given in Table 1. The active region for the devices used in these experiments is composed of 6-stacks of InAs quantum dots embedded in InGaAs quantum wells, separated by GaAs barriers, otherwise known as the Dots-in-a-Well (DWELL) laser structure [1]. The upper and lower cladding layers consists of a p-$Al_{0.2}Ga_{0.8}As$ and n-$Al_{0.2}Ga_{0.8}As$, respectively, with a "low-high" doping profile as shown in Fig. 2-1. This low-high design is very important for minimizing internal loss due to free-carrier absorption that occurs when the

optical mode interacts with a heavy doped cladding [2]. The relatively small refractive index step at the core-clad boundary of the waveguide was chosen to expand the optical mode in the transverse (growth) direction, which then lowers the photon density at a given optical output power. The total cladding thickness is 2.5 μm not including the intrinsic GaAs and graded index layers. Standard multi-section laser processing was used to fabricate the ridge waveguide and the anode/cathode metal contacts. There are two series of devices that have been studied in this dissertation, ZLG788A and ZLG788B, each having a different ridge waveguide width. A Scanning Electron-beam Microscope (SEM) was used to image the cross-section of the ZLG788A processed devices. These images are shown in Figs. 2-2 through 2-3, where it is seen that the width of the waveguide is 3.46 μm at the base of the ridge and the etch depth is 2.0 μm. The ZLG788B series of devices contains a 5-μm ridge width. It is important to distinguish between the different ridge widths because this directly affects the effective current density as seen by the active layer which in turn impacts the threshold current density as well as the operational range where narrow pulse generation occurs. From Fig. 2-2 it is noted that the ridge waveguide etch is not completely vertical such that the width is 2.94 μm at the top of the ridge compared to 3.46 μm at the base. This is a consequence of the inductive plasma etching process. Although this is a directional etching process, with increasing time the edges of the mask begin to degrade resulting in a small percentage of lateral etching. Never-the-less the resulting ridge angle of 82.7º is good in comparison to wet etching processes which typically result in ridge angles closer to 54º [3]. This will manifest as an increase in series resistance within the injection current circuit. Each device has an intra-cavity saturable absorber that is electrically isolated from the gain section via proton implantation. In Fig.

2-4 the isolation gap between the absorber and the gain section has been imaged. Electrical DC resistance has been measured to be approximately 8 MΩ.

The two section mode-locked lasers from the ZLG788A and ZLG788B series have an 8.0-mm cavity length and achieve a steady-state pulsed operation at a nominal fundamental repetition rate of 5 GHz corresponding to a 200 ps pulse interval. The length of the intra-cavity absorber (L_a) is varied among the different devices. In this dissertation, devices having L_a = 0.8-mm, 1.0-mm, 1.2-mm, 1.4-mm, and 1.6-mm are primarily examined. The resulting absorber to gain-section length ratios are 0.11, 0.14, 0.18, 0.21, and 0.25 respectively. In these two-section lasers, the facets are HR(95%)/AR(5%) coated with the absorber adjacent to the HR-coated facet. This facilitates the colliding pulse mechanism [4], wherein two counter propagating pulses interact within the saturable absorber to produce a mutual saturation of the absorber that narrows the optical pulse.
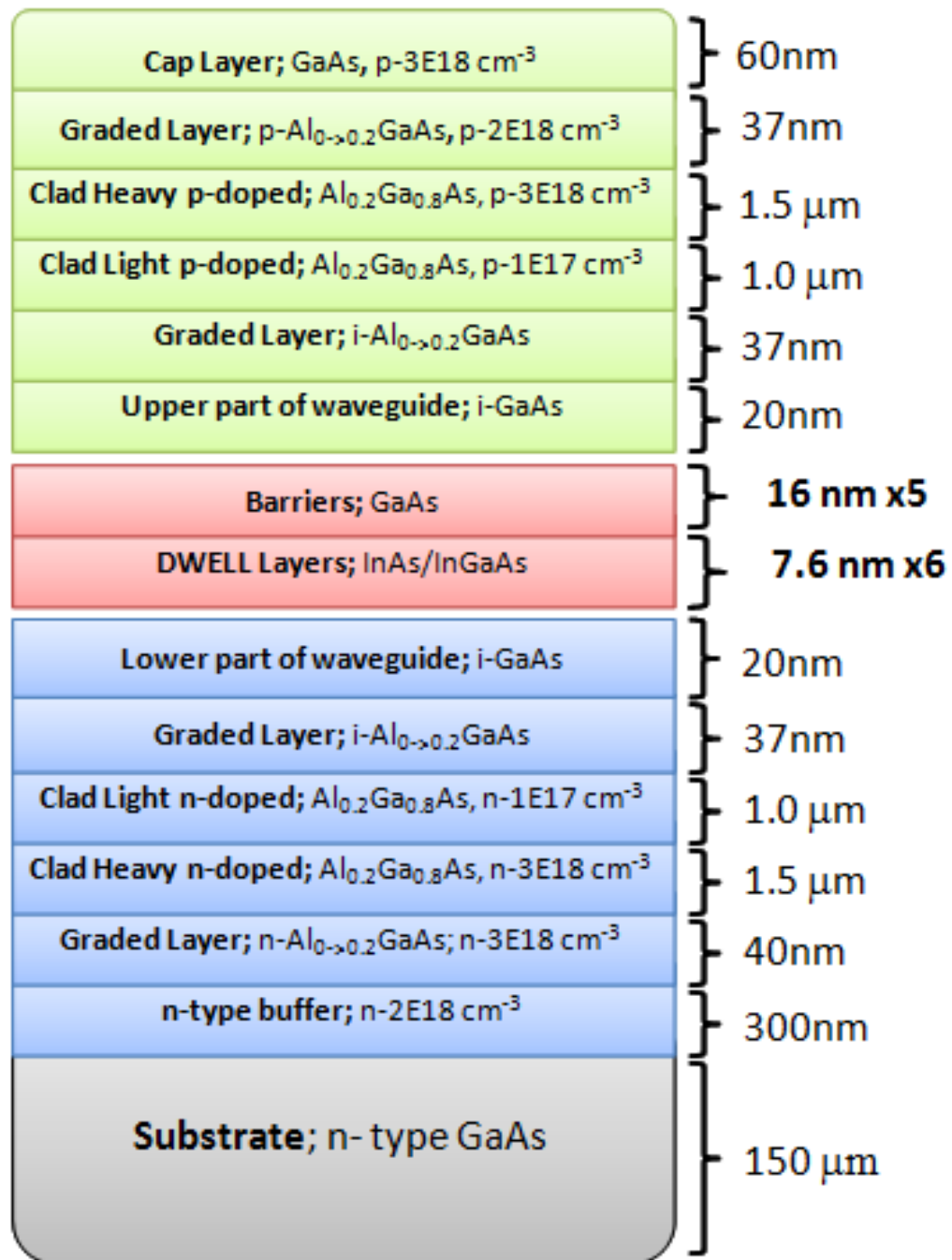
Figure 2-1. ZLG788 series epitaxial layer structure. Thickness, composition and doping concentration are shown. The devices have a 6-stack dots-in-a-well active region with 20% AlGaAs upper and lower cladding layers.

29

Table 1: ZLG788 - Layer thickness, description and refractive index at 1255 nm

Thickness	Description	Index @ 1255 nm
60 nm	cap layer	3.45546
40 nm	graded p-AlGaAs layer	3.35624-3.45546
1500 nm	upper clad, heavily p-doped	3.35624
1000 nm	upper clad, lightly p-doped	3.35624
37 nm	graded i-AlGaAs layer	3.45546-3.35624
20 nm	upper part of waveguide	3.45546
16 nm, 5X	barriers	3.45546
7.6 nm, 6X	DWELL layers	3.6
20 nm	lower part of waveguide	3.45546
37 nm	graded i-AlGaAs layer	3.35624-3.45546
1000 nm	lower clad, lightly n-doped	3.35624
1500 nm	lower clad, heavily n-doped	3.35624
40 nm	graded n-AlGaAs layer	3.45546-3.35624
300 nm	n-type buffer	
1.5 μm	substrate	`
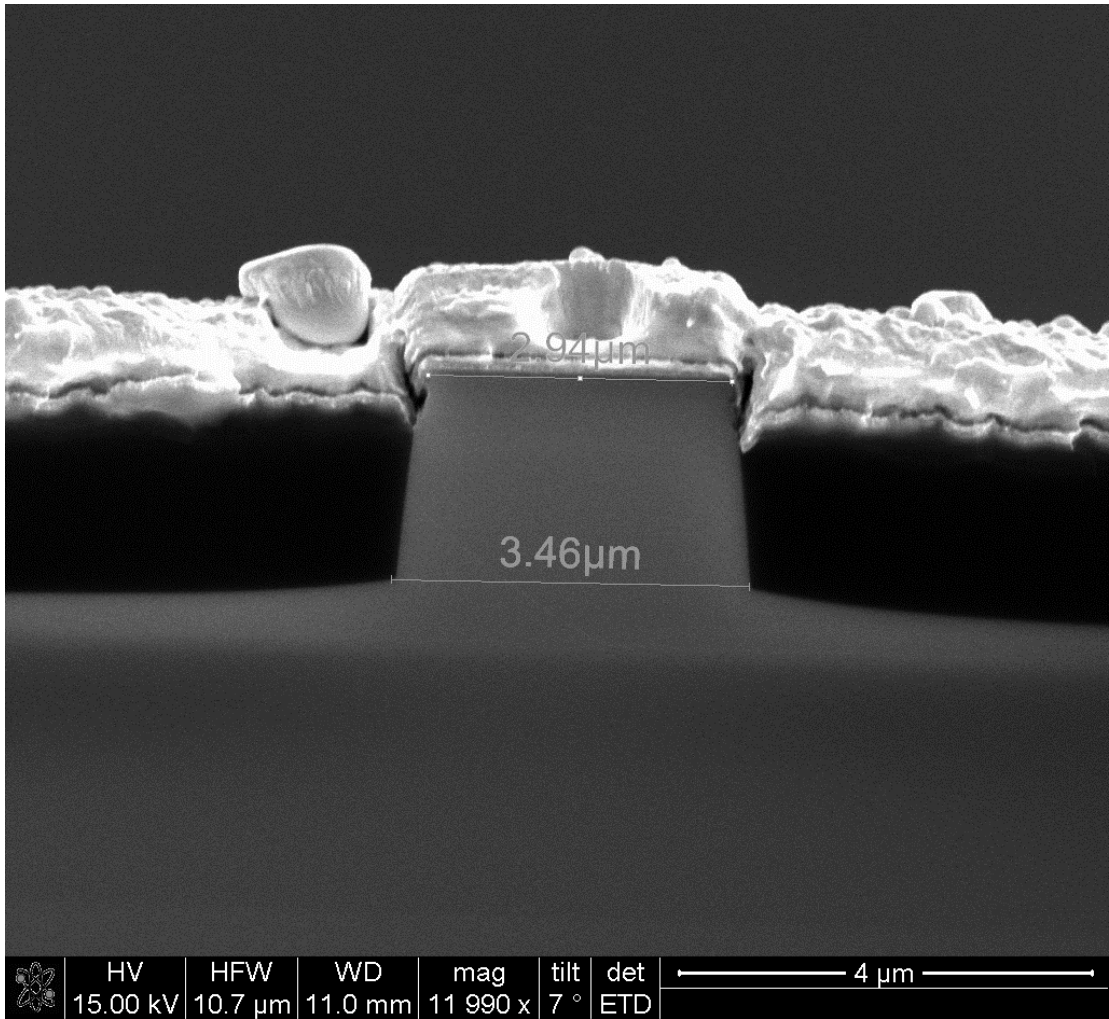
Figure 2-2. SEM cross-section of ZLG788A series device. The waveguide width is determined to be $w = 3.46$ μm at the base of the ridge, and $w = 2.94$μm at the top of the ridge.
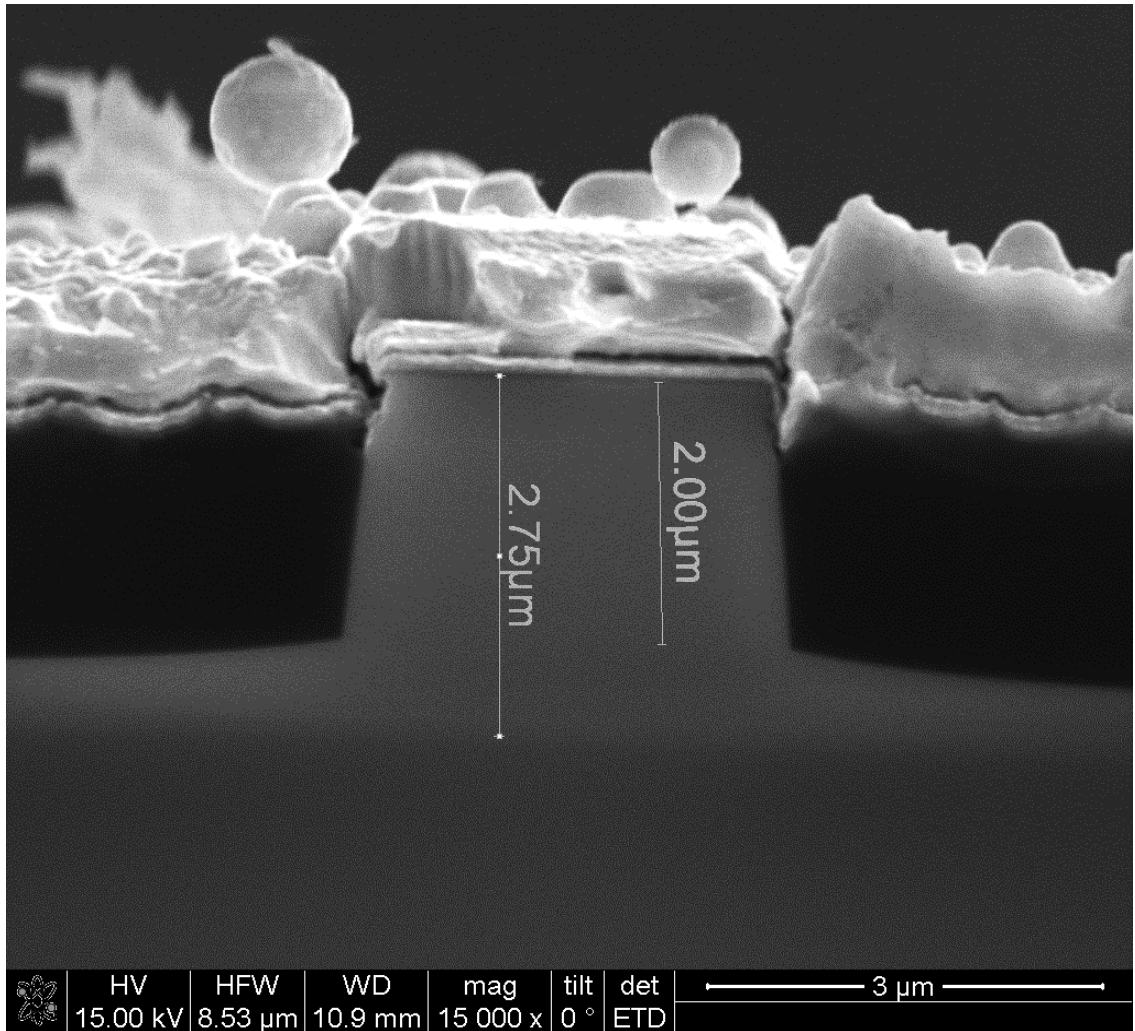
Figure 2-3. SEM cross-section of ZLG788A series device. The etch depth of the ridge waveguide is determined to be 2.00 µm. The thickness of the upper cladding layer plus the core waveguide is 2.75µm. The DWELL active region is contained within the core.
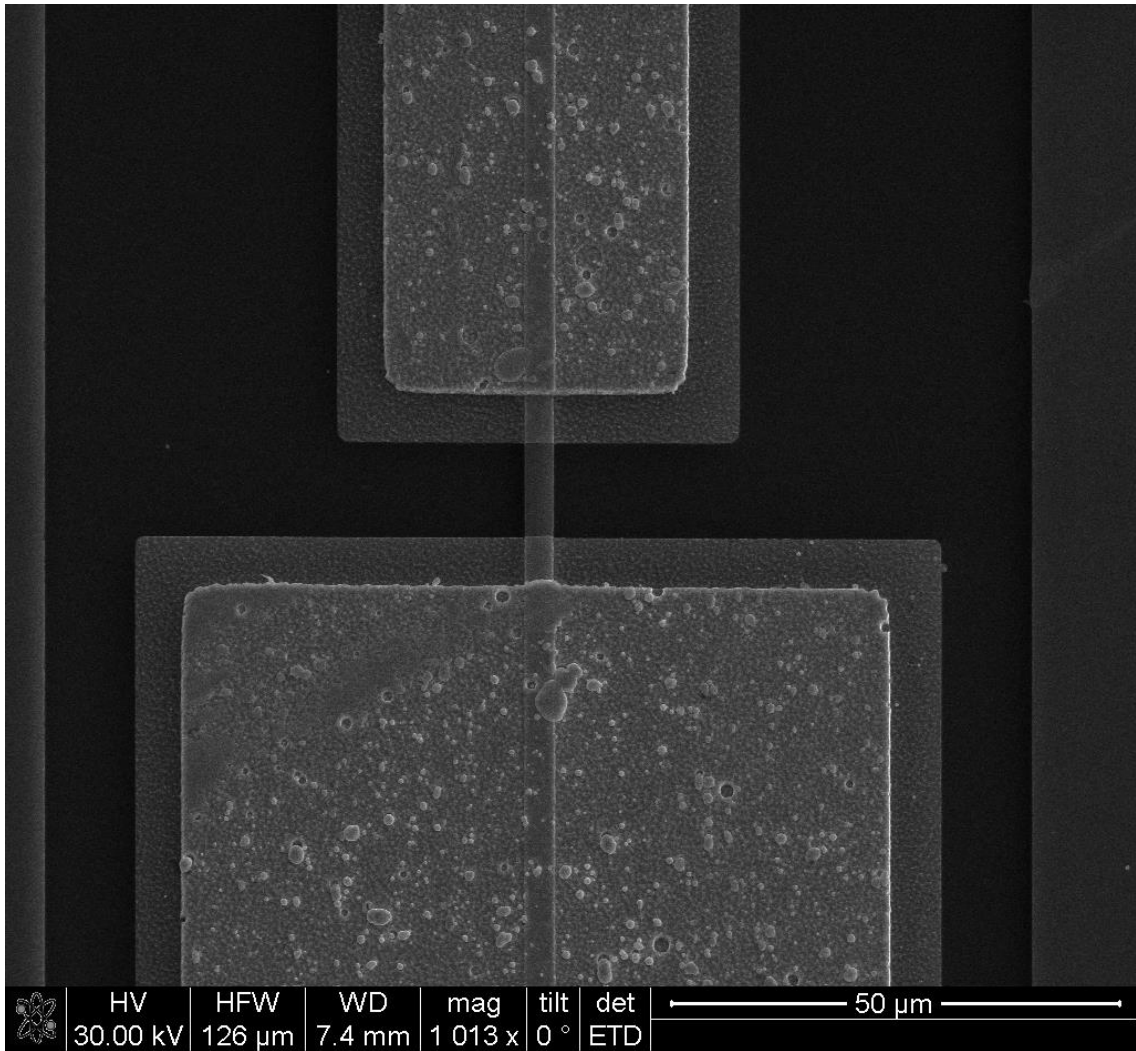
Figure 2-4. SEM image of ZLG788A series device. Isolation gap between the saturable absorber and gain section shown. A proton implantation at this gap creates approximately 8 MΩ electrical resistance. The internal loss in this short, 10-μm long section is estimated at 100 cm^{-1}.

As a final step, the processed lasers are cleaved and mounted onto an AlN carrier, where the absorber and gain contacts of the laser are wire bonded to the larger gold contacts on the AlN carrier. This not only adds mechanical stability but also improves the thermal conductivity as well. An image of the laser mounted onto the AlN carrier is shown in Fig. 2-5. For robustness, this device-on-carrier could then be placed into an industry standards 14-pin butterfly package, which incorporates active thermal sensing and control within a compact form factor. This package further increases mechanical stability and reduces environmental noise [5]. In this mode, coupling of the laser emission into a single-mode polarization-maintaining fiber is accomplished internally using two lenses to circularize the highly elliptical beam of the laser diode. On the other hand, the devices used for the experiments presented in this study are actually not mounted in the butterfly. In this case the gold contact pads on the AlN carrier are directly probed and laser emission is captured with a lens tipped fiber, or the optical head described in chapter 4. Although less convenient, this arrangement gives us far more flexibility to modify the electrical pumping as seen in Chapter 6 of this dissertation.

The contrast between the upper and lower cladding layers is noted in Figs. 2-2 and 2-3; however, the active region in not readily apparent. The measurement in Fig. 2-3 is actually the thickness of the upper cladding layers and the core waveguide combined. The active region is contained within the core region. Accordingly, in Fig. 2-6 a higher contrast image of the device is shown and reveals that the core layer thickness is 225 nm, and the lower cladding layers combine for a thickness is 2.5 μm. From Fig. 2-1, it is seen that the targeted core thickness was 7.6 nm x 6 DWELL layers, plus 16 nm x 5 barrier layers. This

is equal to 125.6 nm, thus it is concluded that the contrast between the core region, the intrinsic GaAs layers and graded index layers cannot be discerned. These included, the targeted thickness equals 239.6 nm, which is within the measurement error of the SEM. Furthermore, taking 225 nm from 2.75 μm, the upper cladding layers have a measured thickness of 2.525 μm. This is critical information for calculations of effective current density which will be discussed in section 2.3

The relatively low index step waveguide design, $\Delta n = 0.244$, decreases the photon density, which is desirable for reducing the deleterious effect of optical non-linearities at a given power level. This is an important consideration for pulsed lasers with peak power such as the quantum dot mode-locked laser. However, the side effect of this approach is to reduce the optical confinement factor of the active region, and, therefore, increase the threshold current density of the laser. This tradeoff has been studied extensively in the context of high power laser diodes built in the AlGaAs/GaAs waveguide system for wavelengths such as 980 nm [6,7]. Thus, the 20% Al composition used in the cladding layers of the devices examined here is rather typical. The optical confinement factor of the 6-layer DWELL active region is calculated to be 7.4% at 1255 nm using the thicknesses and refractive indices for MBE growth run ZLG788 shown in Fig. 2-1 and Table 1.

2.2 Multi-section single pass emitter

The analytical model discussed in chapter 3 requires measurements of modal gain and absorption. The method for extracting gain and absorption characteristics requires measurements of amplified spontaneous emission under different pump

lengths [8,9]. In order to perform these measurements a multi-section single pass emitter has been processed on the ZLG788A series devices. This test structure contains 16 electrically-isolated sections of 500 μm length each. Not all of these sections are actually used in the gain/absorption measurement. The extra ones are reverse biased to eliminate unwanted back reflections. Like the two-section devices, the multi-section emitter is mounted onto an AlN carrier for increased mechanical rigidity and thermal conductivity. An illustration of the multi-section device is given in Fig. 2-7 bellow. Also shown in Fig. 2-7 is the setup for the segmented contact method used for measuring the device modal gain and absorption characteristics. Three separate current supplies are used to bias the device at different pump lengths. The resulting spontaneous emission is captured by the optical head and measured with an optical spectrum analyzer. Measurements of I1, I2 and I3 are converted into the modal gain profile using the formulism given in [8]. The absorption profile is determined in a similar manner, but with the second section reverse biased rather than driven with a forward current. The resulting spectra from these measurements will be presented in chapter 3.
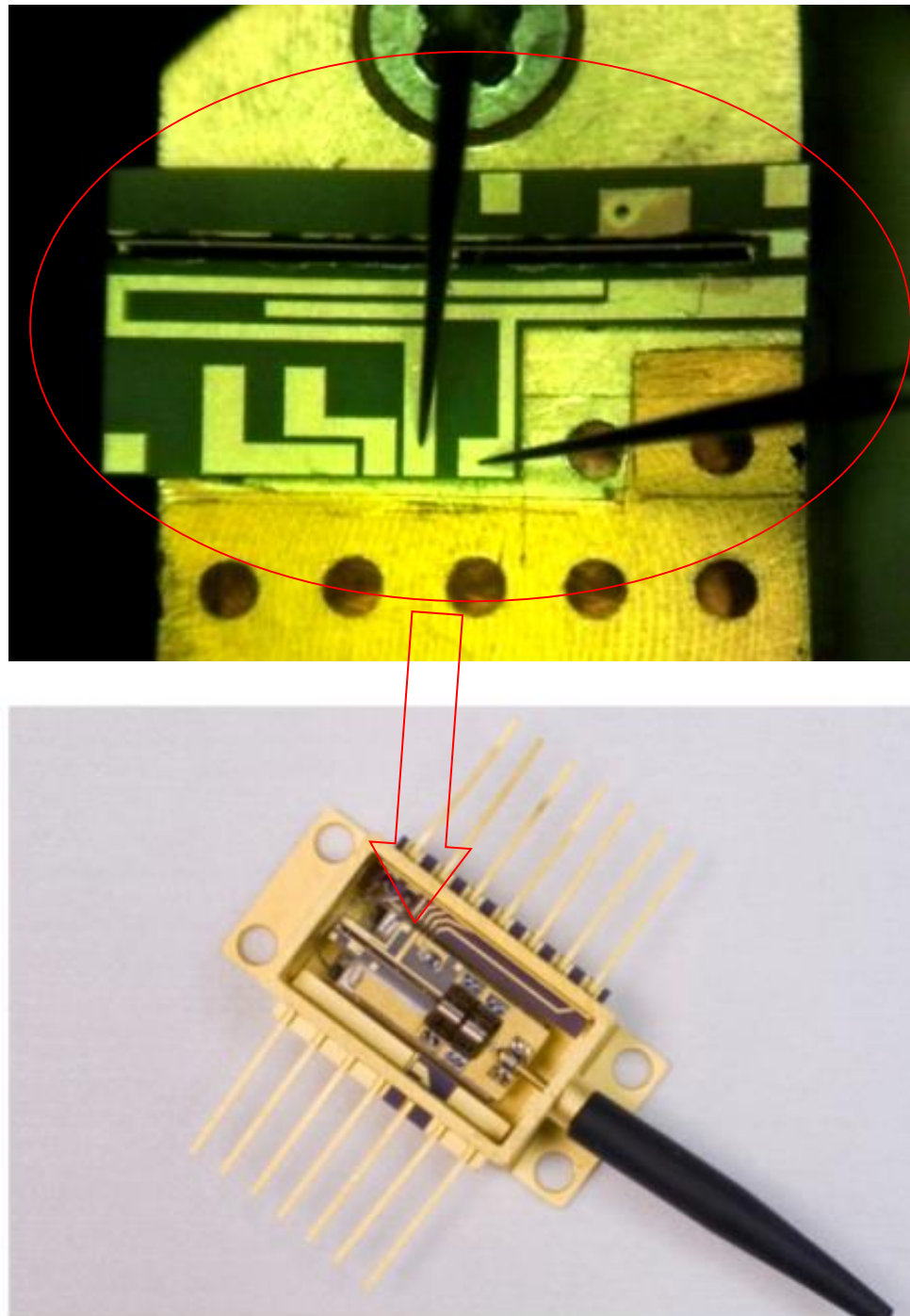
Figure 2-5. (Top) Two-section quantum dot passively mode-locked laser mounted on AlN carrier. (bottom) Laser mounted into a 14 pin butterfly package containing collimating lens, isolator and thermal electrical cooler for convenient operation within a small form factor.
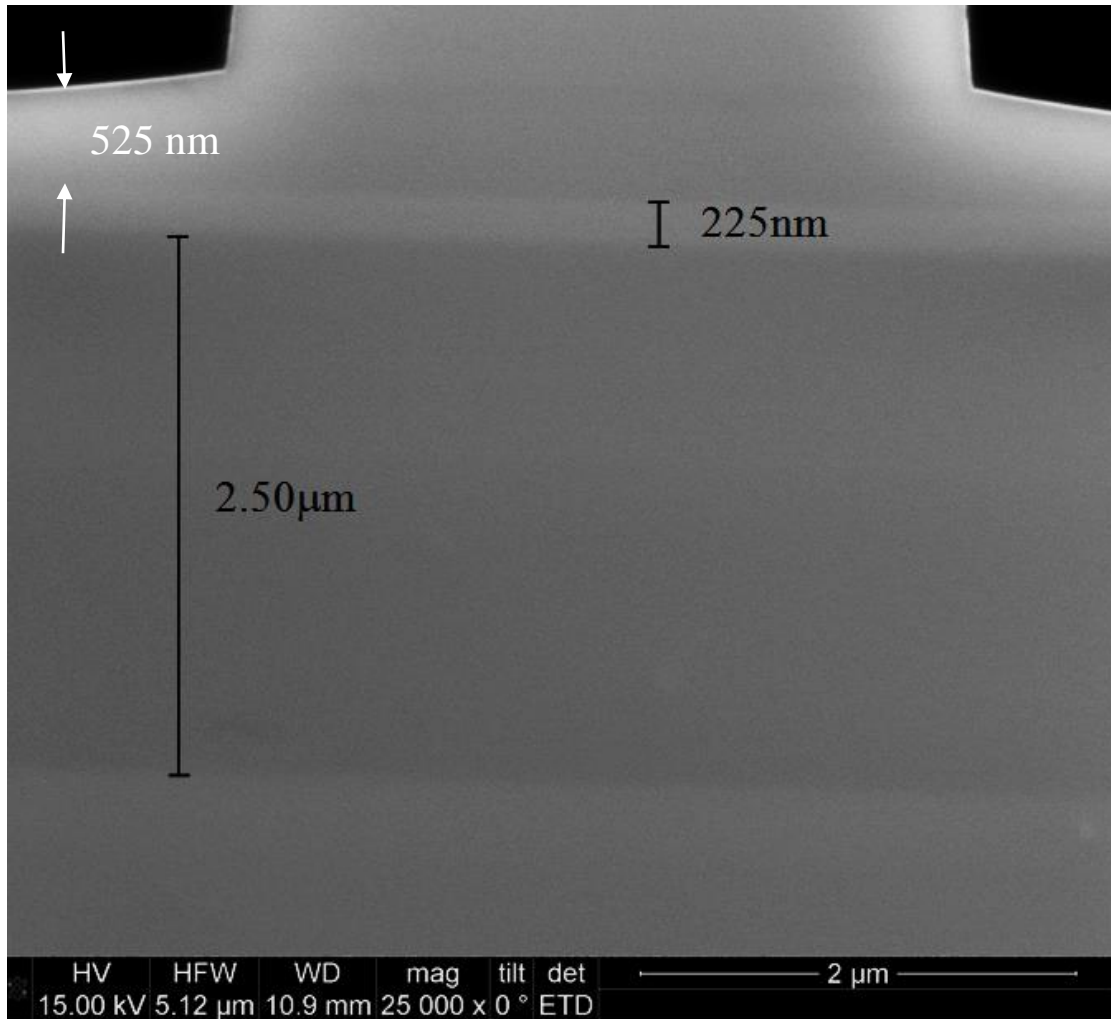
Figure 2-6 High contrast SEM cross-section of the ZLG788A series device. The thickness of the core waveguide region is found to be $t = 225$ nm, and the lower cladding thickness is found to be 2.5 µm. The thickness of the un-etched cladding layer on the side of the ridge is $d = 525$ nm.
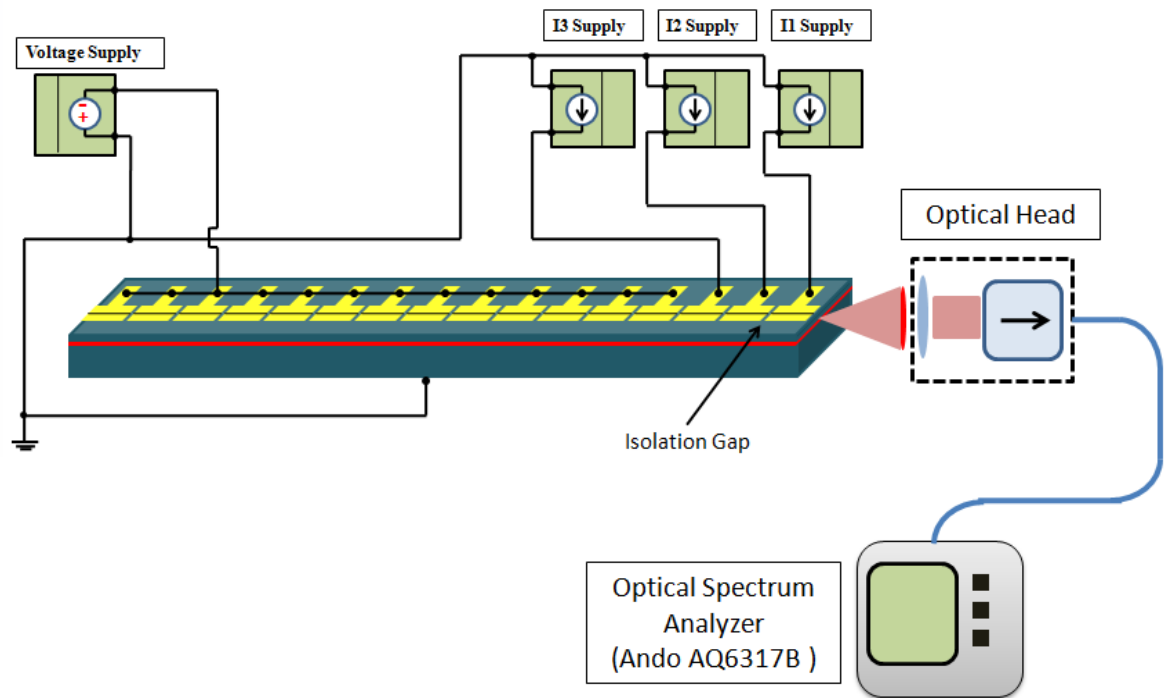
Figure 2-7. Structure of the 16 section device, and the setup for the segmented contact measurement. Spontaneous emission when the device is biased at different pump lengths is coupled into the optical head and measured by an optical spectrum analyzer.

2.3 Effective Current Density

The results presented in this section explore the effective current density injected into the active region and its impact on the threshold current density of the mode-locked laser. It will be further shown in chapter 5 that this has a notable impact on the operational range of the laser and should be strongly considered when designing the laser ridge width and height. It has been shown that the lateral current spreading out of a ridge waveguide has a significant effect on the threshold current density and the modal gain [10]. This current spreading depends on the ridge geometry and the thickness of the un-etched conductive cladding layer remaining beside the ridge. In the previous studies an expression for the effective current density (J_{eff}) in the active region of the device was given by [11]:

$$J_{eff} = J_{total}\left(\frac{2l_s}{w} + 1\right)^{-1}$$

(2-1)

In this expression J_{total} is the applied injection current at the device, w is the width of the laser ridge and l_s is the current spreading length which is expressed as [11]:

$$l_s = \sqrt{\frac{4k_B Td}{q\rho J_{eff}}}$$

(2-2)

where k_B is the Boltzmann constant, T is the temperature, q is the elementary charge, ρ is the cladding layer resistivity, and d is thickness of the un-etched cladding layer. By solving the system of equations in Eqns. (2-1) and (2-2), a previously unpublished expression for J_{eff} can be found:

$$J_{eff} = \left(\left[\frac{\chi^2}{4} + J_{total} \right]^{1/2} - \frac{\chi}{2} \right)^2$$

(2-3)

where χ is given by:

$$\chi = \sqrt{\frac{16k_B Td}{q\rho w^2}}$$

(2-4)

From the cross-sectional SEM images of the ZLG788A series devices shown in Figs. 2-2, 2-3 and 2-6, the laser ridge width, w, is found to be approximately 3.5 μm. The etch depth is 2.0 μm and the depth of the upper cladding layers is 2.525 μm, thus the thickness of the un-etched cladding layer, d, is 525 nm. Taking the hole mobility in the cladding layer to be 239.8 cm^2/V·s [12], the resistivity at room temperature is calculated to be approximately 0.25 Ω·cm. It is found that for a J_{tot} = 1 kA/cm^2, the effective current density in the active layer is J_{eff} = 437 A/cm^2. In Fig. 2-8 the effective current density is plotted as a function of applied current density for the 3.5 μm (ZLG788A) and 5.0 μm devices (ZLG788B) using Eqns. (2-3) and (2-4). For the purposes of this plot it was assumed that the ridge height and etch depth of ZLG788B were the same as that of ZLG788A. This is not necessarily the case; however, the purpose of this discussion is more qualitative. From Fig. 2-8 it is seen that for the same applied current density, the effective current density is greater in the device having a 5 μm ridge width. This is an indication that the efficiency of current injection is higher in the wider ridge devices. Given that the ridge heights are assumed to

be the same (un-etched cladding layer is the same), it follows that the carrier recombination at the sidewalls is identical. Accordingly the device having a narrower ridge waveguide must have a higher percentage of lateral current spreading into the cladding layers. This should result in reduced threshold current density conditions for the ZLG788B series of devices.

To study the aforementioned effect experimentally, threshold current densities were measured for the two devices having identical cavity geometry (L_a=1.2-mm, L_g=6.8-mm), but different ridge widths of 3.5 μm and 5.0 μm. Measurements were taken at 20 °C (blue lines), 40 °C (green lines) and 60 °C (red lines) across the voltage range of 0 to -7 V. In Fig. 2-9, the resulting threshold measurements are plotted. The solid lines represent the 3.5 μm device (ZLG788A AV06), the dashed lines are for the 5.0 μm device (ZLG788B AH09). It is found that in all instances, the threshold current density is greater in the 3.5 μm device. This is consistent with the findings of Fig. 2-8, where it was shown that the device having a narrower *w* had a lower effective current density. While the precise ridge height has not been determined, it is clear that the efficiency of current injection in the wider ridge devices is indeed better. Accordingly, the majority of the experiments presented in this dissertation have been performed on the 5 μm ridge width devices.
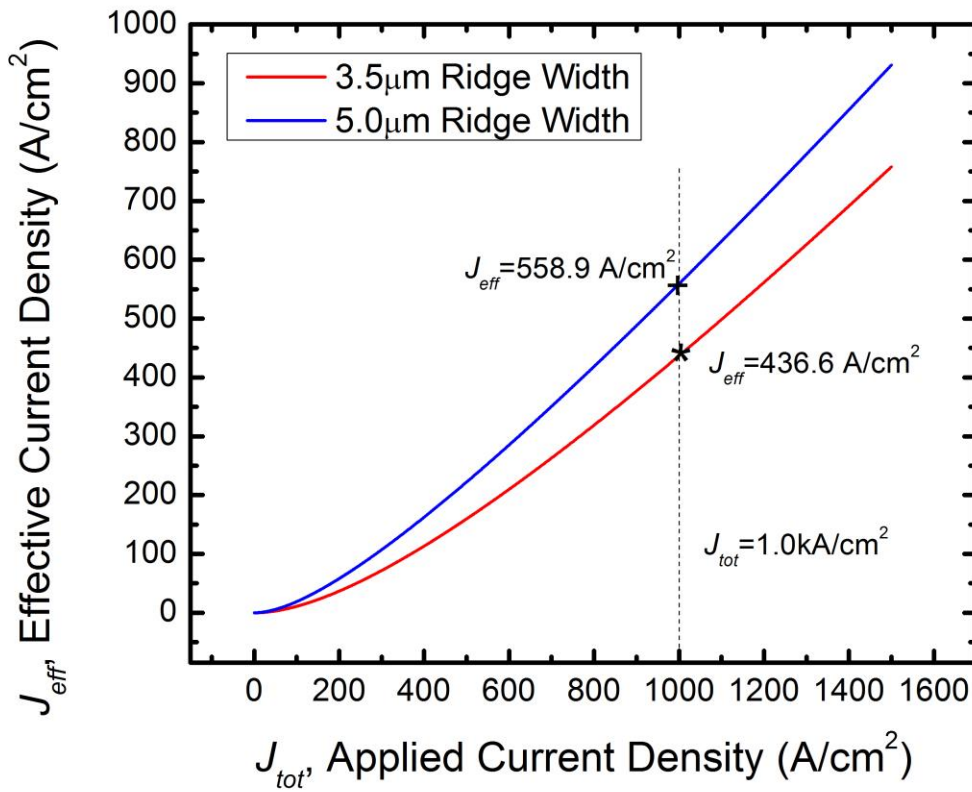
Figure 2-8. Effective current density (J_{eff}) according to Eqns. (2-3) and (2-4) for quantum dot ridge waveguide lasers having a 3.5-μm ridge width (red line), and a 5-μm ridge width (blue line). Resulting J_{eff} are shown in each case for an applied current density of J_{tot}=1 kA/cm².
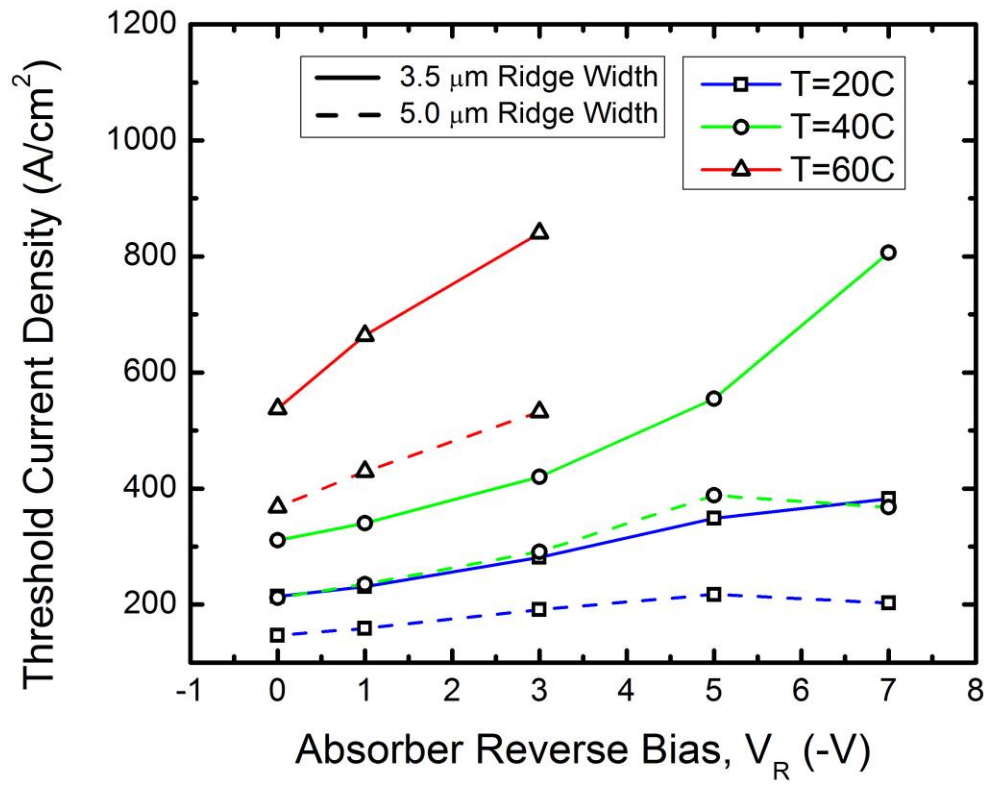
Figure 2-9. Measured threshold current density (J_{th}) over temperature and voltage for a set of two quantum dot lasers. One having a 3.5 μm ridge width (solid lines) and the other a 5.0 μm ridge width (dashed lines). Threshold is shown for the temperatures of 20 ºC (blue lines), 40 ºC (green lines) and 60 ºC (red lines).

REFERENCES FOR CHAPTER 2

[1] G.T. Liu, A. Stintz, H. Li, K.J. Malloy and L.F. Lester, "Extremely low room-temperature threshold current density diode lasers using lnAs dots in InGaAs quantum well" Elect. Lett., vol. 35, pp. 1163-1165, (1999)

[2] Jia-Ming Liu, Photonic Devices (Cambridge University Press, New York, 2005)

[3] D Ouyang, N N Ledentsov, D Bimberg, A R Kovsh, A E Zhukov, S S Mikhrin and V M Ustinov, "High performance narrow stripe quantum-dot lasers with etched waveguide," Semicond. Sci. Technol. vol. 18, no. 12 (2003)

[4] R. L. Fork, B. I. Greene, and C. V. Shank, "Generation Of optical pulses shorter than 0.1 psec by colliding pulse mode-locking," *Appl. Phys. Lett.*, vol.38, pp. 671-672 (1981)

[5] Chang-Yi Lin, Frederic Grillot, Yan Li, Ravi Raghunathan, and Luke F. Lester, "Characterization of timing jitter in a 5 GHz quantum dot passively mode-locked laser," Optics Express, vol. 18, no. 21, pp. 21932-21937 (2010)

[6] R.W.H. Engelmannn, C.L. Shieh, and C.Shu, "Multiquantum well lasers: threshold considerations," Quantum well Lasers, edited by P. Zory, Academic Press, Boston, MA, pp. 131-186 (1993)

[7] Dmitri Z. Garbuzov ; Joseph H. Abeles ; Nancy A. Morris ; Peter D. Gardner ; Alfred R. Triano ; Maria G. Harvey ; Dean B. Gilbert ; John C. Connolly; High-power separate-confinement heterostructure AlGaAs/GaAs laser diodes with broadened waveguide. Proc. SPIE 2682, Laser Diodes and Applications II, 20 (1996);

[8] Y.-C.Xin, Y. Li, A. Martinez, T. J. Rotter, H. Su, L. Zhang, A. L. Gray, S. Luong, K. Sun, Z. Zou, J. Zilko, P. M. Varangis, and L. F. Lester, "Optical gain and absorption of QD measured using an alternative segmented contact method" IEEE J. Quantum Electron. 42, 725 (2006)

[9] P. Blood, G. M. Lewis, P. M. Smowton, H. Summers, J. Thomson, and J. Lutti, "Characterization of semiconductor laser gain media by the segmented contact method" IEEE J. Sel. Top. Quantum Elect., 9, 1275 (2003)

[10] S. Y. Hu, D. B. Young, A. C. Gossard, and L. A. Coldren, "The effect of lateral leakage current on the experimental gain/current-density curve in a quantum-well ridge-waveguide lasers," IEEE J. Quantum Elect. vol. 30, no. 10, pp. 2245-2250 (1994)

[11] Rui Wang, Soon Fatt Yoon, Han Xue Zhao, and Chun Yong Ngo, "Geometrical Effects on Characteristic Temperatrure and Modal Gain of InAs/GaAs Quantum-Dot Lasers," IEEE Phot. Tech. Lett. vol. 23, no. 12 (2011)

[12] Donald A. Neamen, Semiconductor Devices (McGraw-Hill Companies Inc. New York, 2003)

Chapter 3 – Analytical Model of the Mode-Locking Stability

In contrast to *numerical* modeling efforts currently being developed to predict temporal domain optical field profiles from a quantum dot mode-locked laser [1-3], this chapter discusses an *analytical* model that enables prediction of the regions of mode-locking stability from a quantum dot mode-locked laser for a given cavity geometry. The cavity geometry in a two-section mode-locked laser is the absorber length to gain length ratio. In section 3.1, the determination of modal gain and absorption characteristics are presented. The analytical model discussed in this chapter has the unique advantage that all parameters which appear in the analytical expressions can be derived from modal gain and absorption profiles measured directly on the device of interest. In section 3.2, the set of analytical expressions that form the upper and lower bounds of the model are introduced. This directly represents the range of device geometries that are expected to achieve mode-locking threshold for a particular temperature. The resulting modeled stability maps are presented in section 3.3 for a wide range of temperatures and saturable absorber reverse voltages. Finally, in section 3.4 the predictive capabilities of the analytical model are presented. Namely, the predicted operational range is examined when model parameters are adjusted to represent different processing characteristics.

3.1 Determination of Modal Gain and Absorption

The analytical model presented in the next section is a useful tool for predicting the regions of mode-locking stability for a given device geometry. In this section, the approach for extracting model parameters from the experimental data is outlined. This model requires inputs derived from static gain and loss characteristics measured directly on the

device. In order to perform a full analysis of the QD material used in this study, gain spectra were measured at TE cooler temperatures from 20 to 120 ºC over a range of current densities from 229 to 1257 A/cm^2. Total loss spectra were measured for absorber voltages from 0 to -7 V and the same temperature range. Gain and absorption measurements were conducted on device series 788A multi-section single pass emitter described in chapter 2 using a segmented contact method. In this technique, the gain profile is determined by measuring the emitted amplified spontaneous emission with different pump lengths. The absorption profile is determined in a similar fashion but requires the addition of a variable reverse bias. Details of these measurements and the relevant equations can be found in [4, 5].

a. Modal Gain Profile

Firstly, the modal gain results are presented. For clarity, the modal gain spectra for selected temperatures between 20 and 120 °C are shown in Fig. 3-1 at a constant current density of 857 A/cm^2 (15 mA applied to a 500-µm x 3.5-µm section). The measured modal gain data in its completeness is presented in *Appendix A*. At 20°C, three primary optical transitions are evident in Fig. 3-1 corresponding to the ground state (GS) transition at λ=1222.2 nm, the first excited state (ES) transition at λ=1158.8 nm, and the second ES transition at λ=1112.2 nm. It is noted that the second ES is not clearly evident for temperatures greater than 20 ºC. The measured spectra shown in Fig. 3-1 were measured at the same current density and only the temperature was varied. From these measurements, the observed spectral variation of the GS gain peak between 20 ºC and 60 ºC is 0.64 nm/ºC whereas between 60 ºC to 100 ºC it is 0.39 nm/ ºC. The observed red shifting of the GS

gain peak is expected to be a combination of both band gap shrinkage (BGS) and the temperature-dependent shift of the bandgap [6]. For the devices reported here, it is likely that 60 ^{o}C represents an activation energy associated with a non-radiative recombination process [7]. As a consequence, fewer carriers would be available for radiative recombination and the contribution to the red shift due to BGS would be reduced [8]. Inspection of the magnitude of the modal gain over temperature reveals that the GS gain degrades from 10.2 cm^{-1} to 4.4 cm^{-1}, while the ES gain degrades more significantly from 14.1 cm^{-1} to 4.1 cm^{-1}. This has been attributed to a reduced radiative efficiency for higher energy transitions at elevated temperature [9].
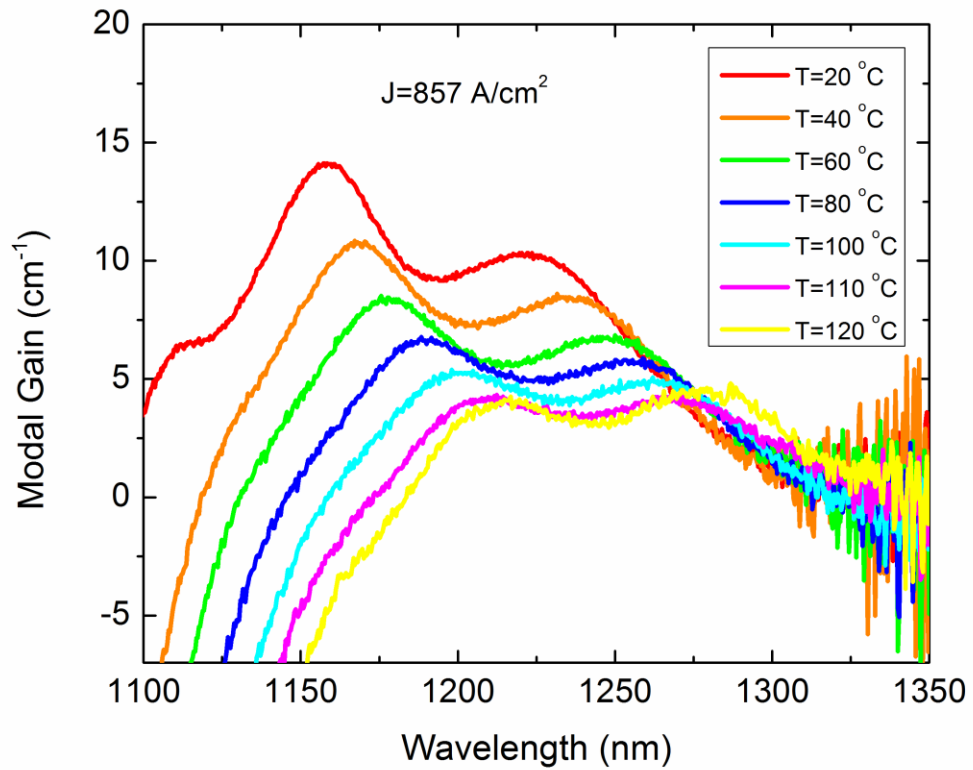
Figure 3-1. Measured modal gain spectra for a constant current density of 857 A/cm^2 at 20, 40, 60, 80, 100, 110 and 120 ºC. The wavelength of emission from the ground state is observed to red shift at an average rate of 0.64 nm/ºC between 20-60 ºC, and 0.39 nm/ºC between 60–110 ºC

For completeness, the peak modal gain values and their matching emission wavelengths in the ground state are summarized from 20 to 80 ℃ in Table 1. For the temperatures of 100 to 120 ℃, the ES gain peak wavelengths and modal gain values are summarized in Table 2. This selection was based on examination of optical spectra which revealed that for the case of a grounded saturable absorber, the lasing wavelength transitioned from GS to ES between 93 and 98 ℃ for the device having L_a=0.8-mm, and between 80 and 85 ℃ for L_a=1.0-mm. The devices having longer absorber lengths failed to produce mode-locked pulses from the ES when the absorber was grounded. The complete set of optical spectrum data will be presented in chapter 4.

From the modal gain data presented in Fig. 3-1 and Tables 1 and 2, the first of the required model inputs can be derived; namely, the modal gain and differential modal gain with respect to current density. For a given temperature and current density, J, it is assumed that the MLL emits at the wavelength corresponding to the peak gain. Consequently, the quantum dot peak modal gain behavior in Fig. 3-1 can be modeled using the following empirical expression [10]:

$$g_o(J) = g_{max}\left[1 - \exp\left(\frac{J_{tr} - J}{b}\right)\right] + \alpha_i \tag{3-1}$$

that has the corresponding differential gain of:

$$\frac{dg_o}{dJ} = \frac{g_{\text{max}}}{b} \exp\left(\frac{J_{tr} - J}{b}\right)$$

(3-2)

in which $g_o(J)$ is the modal gain with respect to current density, g_{max} is the measured

maximum net gain, J_{tr} is the transparency current density, α_i is the internal loss, and b is a

fitting parameter which carries units of A/cm^2. The differential gain evaluated at g_o=0cm$^-$

^{1} ($J = J_{tr}$) represents a conservative approximation for the differential absorption and has

the convenient result based on the fitting parameters [11]:

$$\frac{da_o}{dJ} \approx \left.\frac{dg_o}{dJ}\right|_{g_o=0} = \frac{g_{\text{max}}}{b}$$

(3-3)

In Fig 3-2a, the measured modal gain at the GS gain peak as a function of current

density over the temperature range 20 to 80 °C is shown. This represents the range of

temperatures wherein lasing occurred from the GS when the saturable absorber was

grounded. For the remaining temperatures, the measured modal gain at the ES gain peak is

shown in Fig 3-2b. The symbols in Figs. 3-2a and 3-2b are the experimental values from

Tables 1 and 2 respectively, and the solid lines are the fits according to Eqn. (3-1). From

this, the modal gain, differential modal gain, and differential absorption are determined.

Table 2: Ground State Modal Gain at Peak Gain Wavelength

J A/cm²	T=20 ºC		T=40 ºC		T=60 ºC		T=80 ºC	
	G_{peak} nm	g_o cm⁻¹	G_{peak} nm	g_o cm⁻¹	G_{peak} nm	g_o cm⁻¹	G_{peak} nm	g_o cm⁻¹
1257	1225.6	11.0	1236.9	8.7	1245.5	7.5		
1143	1224.2	10.9	1235.6	8.5	1246.2	7.2	1251.4	7.1
857	1222.2	10.2	1234.7	8.4	1247.9	6.8	1255.3	5.8
685	1221.9	9.9	1232.2	7.8	1244.0	6.1	1252.2	5.3
571	1221.6	9.3	1231.9	7.3	1245.6	6.2	1251.2	4.9
457	1221.5	8.9	1231.8	6.9	1247.2	4.7	1249.8	4.5
400	1221.2	7.7	1232.1	6.2	1245.4	4.6	1253.8	3.3
314	1220.9	6.8	1232.4	4.4	1244.7	3.8	1255.6	2.5
229	1220.2	6.0	1233.5	3.9				

Table 3: Excited State Modal Gain at Peak Gain Wavelength

J A/cm²	T=100 ºC		T=110 ºC		T=120 ºC	
	G_{peak} nm	g_o cm⁻¹	G_{peak} nm	g_o cm⁻¹	G_{peak} nm	g_o cm⁻¹
1257			1204.7	7.4		
1143	1199.4	7.7	1206.3	6.8	1214.5	7.2
857	1200.1	5.3	1208.8	4.2	1215.8	5.2
685	1208.4	4.1	1214.3	3.3	1216.6	4.1
571	1211.9	3.2	1219.4	2	1219.6	3.1
457	1215.8	2.8	1219.2	0.6	1225.4	2.9
400	1215.2	2.2	1217.5	-1.2	1228.5	-0.3
314	1219.1	-0.5				
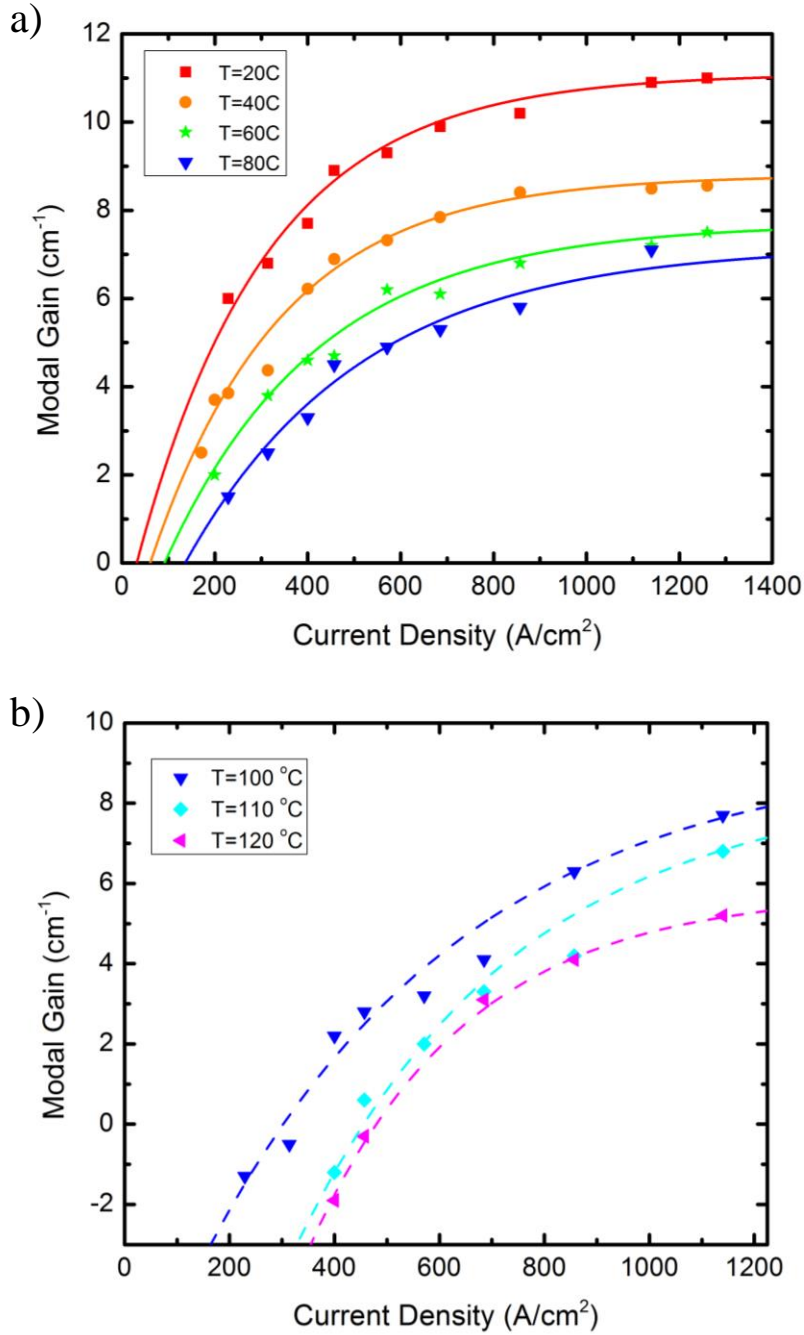
Figure 3-2. a) Measured modal gain peak (symbols) of the GS as a function of current density over the temperature range from 20 to 80 °C. b) Measured modal gain peak of the ES as a function of current density from 100 to 120 °C. Solid lines are the resulting fits from Eqn. (3-1).

b. Modal Absorption Characteristics

As presented in the next section, the unsaturated absorption and internal loss are the only remaining model parameters after the above analysis of the modal gain spectra. The internal loss can be derived from the net gain spectra; however, it is most evident by inspection of the absorption characteristics shown in Fig. 3-3 for the case of 0 V applied to the saturable absorber. For completeness, the absorption characteristics for the remaining voltages studied are shown in *Appendix B*. In our case the internal loss was found to be an average of 2.4 cm^{-1} over the full range of temperatures examined. From Fig. 3-3 the average differential wavelength shift, $\Delta\lambda/\Delta T$, in the absorption peaks is 0.44 nm/^{o}C between 20 and 60 ^{o}C, and it reduces to 0.42 nm/^{o}C between 60 and 110 ^{o}C. Recall that the overall average wavelength shift in the modal gain peak was greater than the above-mentioned values for the absorption peak; however, it is noted that this shift reduces more significantly in the gain spectra than in the loss spectra such that for higher temperatures $\Delta\lambda/\Delta T|_{\text{gain peak}} < \Delta\lambda/\Delta T|_{\text{abs peak}}$. Similar trends have been previously reported [10,12]. This turns out to be a critical detail in understanding the temperature of maximum stability, which will be discussed in more detail in chapter 6. For convenience, in Table 3 a complete list of the absorption peak wavelengths and corresponding maximum absorption values is given in the ground state at each temperature for applied voltages from 0 to -7 V.

c. Unsaturated Absorption

The next step is to determine the values of unsaturated absorption, a_0, for any particular temperature and reverse bias voltage on the absorber. This is accomplished by projecting the range of gain peak wavelengths (complied in Tables 1 and 2 for the full

range of current densities) onto the total loss spectra presented in Fig 3-3. The bands in Fig. 3-3 represent the range of measured gain peak wavelengths. The unsaturated absorption is found by taking the average absorption value over the region and then subtracting the internal loss. This process is repeated for each temperature and reverse voltage. Unsaturated absorptions values for each temperature and voltage combinations are recorded in Table 4. It is found that the unsaturated absorption reaches a minimum at T=60 °C. This is a consequence of the variance in the differential wavelength shift of the gain and absorption spectra, which results in the gain peak walking off of the absorption peak. For the case of T=80 °C, the unsaturated absorption is slightly higher than that of T=60 °C because the shift in the gain peak is significantly reduced for higher temperatures. The values of a_o increase dramatically at 100 °C and higher, when the MLL is lasing from the ES. Intuitively this would seem to reduce the likelihood of achieving laser threshold; however, the increase in a_o is compensated by an increase in modal gain, g_o, at the first ES.
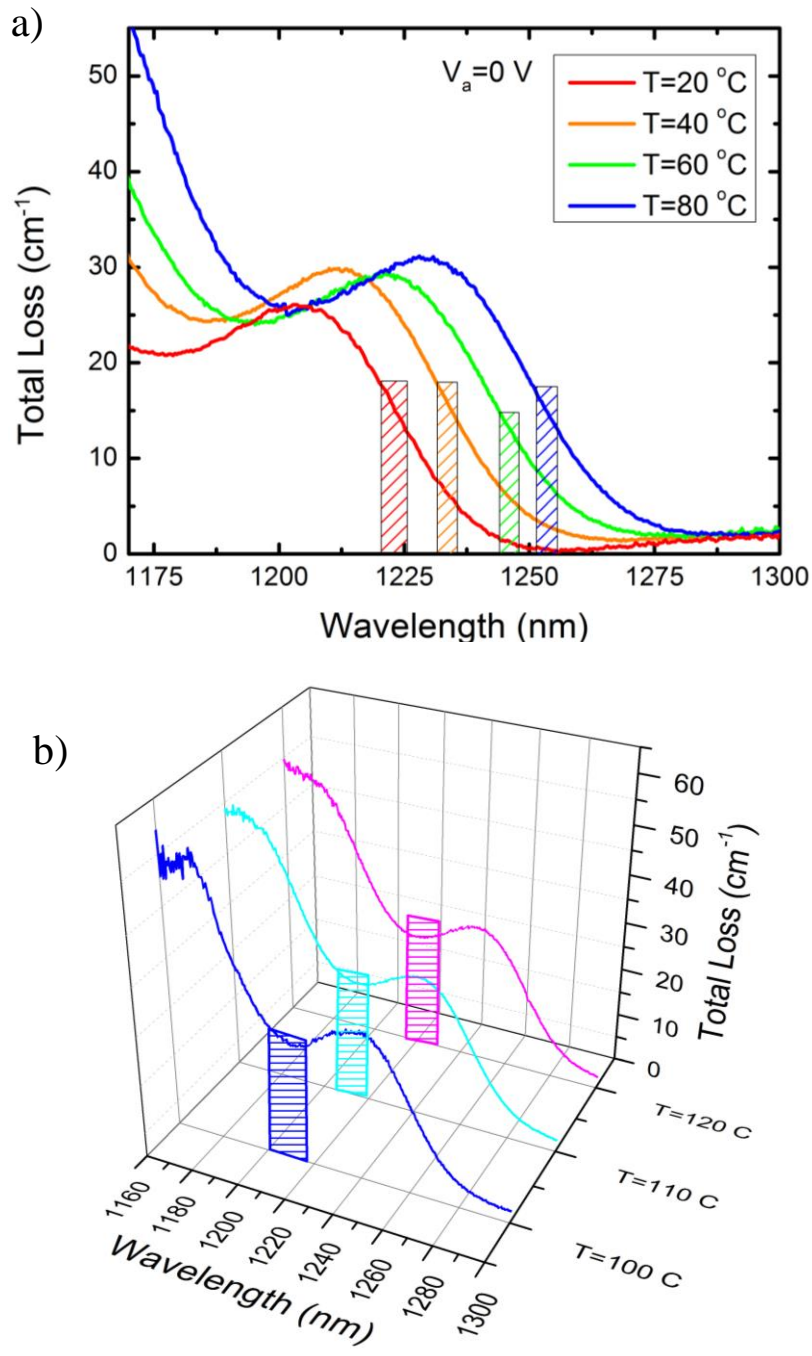
Figure 3-3. Measured total loss spectra for absorber reverse bias of 0 V from T=20 to 80 °C in (a) and from 100 to 120 °C in (b). The shaded bands represent the range of absorber losses possible given the gain peak positions as a function of current density found in Tables 1 and 2.

Table 4: Absorption Peak Wavelengths and Max Absorption

Temp (°C)	V=0 V		V=1 V		V=2 V		T=3 V	
	a_{peak} nm	a_{max} cm^{-1}	a_{peak} nm	a_{max} cm^{-1}	a_{peak} nm	a_{max} cm^{-1}	a_{peak} nm	a_{max} cm^{-1}
20	1203.5	26.0	1205.7	25.7	1208.7	25.1	1210.2	24.2
40	1211.8	29.8	1213.5	28.5	1215.5	27.3	1218.2	26.4
60	1221.2	29.2	1222.7	27.3	1225.2	26.2	1228.4	24.7
80	1229.2	31.0	1231.4	28.8	1233.5	27.5	1235.4	26.4
100	1239.4	30.2	1242.1	29.1	1243.1	28.3	1244.3	27.1
110	1242.1	29.6	1244.3	28.0	1245.5	27.3	1248.8	26.8
120	1246.9	28.5	1248.6	27.3	1250.1	25.9	1253.1	25.5
	V=4 V		V=5 V		V=6 V		T=7 V	
	a_{peak} nm	a_{max} cm^{-1}	a_{peak} nm	a_{max} cm^{-1}	a_{peak} nm	a_{max} cm^{-1}	a_{peak} nm	a_{max} cm^{-1}
20	1211.9	23.4	1212.9	22.5	1214.6	22.5	1216.0	21.8
40	1220.2	25.4	1222.4	24.6	1224.3	23.6	1226.1	22.5
60	1229.6	23.6	1231.8	22.9	1233.7	22.0	1234.9	20.9
80	1237.4	25.6	1239.6	24.6	1241.9	23.7	1243.5	23.0
100	1246.1	26.5	1248.4	25.9	1250.3	24.7	1251.5	23.9
110	1249.7	25.7	1251.8	24.4	1254.2	23.5	1254.3	22.2
120	1255.5	24.5	1257.2	23.5	1259.7	22.9	1262.2	22.3

Table 5: Unsaturated Absorption Values a_o (cm^{-1}) Assuming Average Internal Loss of

$\alpha_i=2.4$ cm^{-1}

Voltage (V)	20ºC	40ºC	60ºC	80ºC	100ºC ES	110ºC ES	120ºC ES
0	12.9	12.5	10.7	12.5	23.2	23.6	22.0
1	14.7	14.1	12.0	13.7	23.8	23.6	21.2
2	16.0	15.3	13.3	15.1	23.7	24.5	20.2
3	16.8	16.8	14.2	16.4	23.7	24.8	20.2
4	17.6	17.6	15.0	17.4	24.7	25.3	20.1
5	17.9	18.3	16.2	18.3	26.0	25.2	20.3
6	18.6	18.6	16.6	18.5	25.9	26.0	20.9
7	18.4	18.5	16.4	18.6	26.7	26.1	21.3

3.2 Development of Analytical Expression from Gain and Loss Characteristics

The analytical expression developed in this section have been constructed to predict the regions of pulse stability for a given device layout and to ultimately investigate the path toward achieving broad temperature operation of QD MLLs. The current representation of the expressions leverages previous work by Lin *et. al*. [11] and Crowley *et. al*. [10]. In the previous section, the method for deriving all of the input parameters that appear in this model from static gain and loss measurements was outlined. The model is based on the idea that the onset of passive mode-locking in a semiconductor lasers is bound by two functions. The first is derived from a net-gain modulation phasor approach, describing the onset of passive mode-locking as a sinusoidal variation in output intensity [13,14]. The expressions derived in that study assumed that the gain and loss were uniformly distributed in the cavity. Subsequent work by Lin *et. al.* [11], expanded this approach to account for discrete, electrically-isolated gain and saturable absorber sections. For convenience, the resulting modified equation is stated here as well:

$$\frac{L_a}{L_g} > \left(\frac{\frac{dg_O}{dJ}}{\frac{dg_O}{dJ}\Big|_{g_O=0}} \right)^2 \frac{g_O(J)}{a_O} \qquad (3\text{-}4)$$

Using the empirical formula from Eqn. (3-1), the mode-lock condition expressed above can be further reduced to the following alternative form:

$$\frac{L_a}{L_g} > \exp\left[2 \cdot \left(\frac{J_{tr} - J}{b}\right)\right]\left(\frac{g_{\max}}{a_0}\left[1 - \exp\left(\frac{J_{tr} - J}{b}\right)\right] + \frac{\alpha_i}{a_0}\right) \qquad (3\text{-}5)$$

The second equation which bounds the regions of passive mode-locking is the threshold condition for lasing and can be expressed in terms of the length of the absorber section over the length of the gain section as follows [10]:

$$\frac{L_a}{L_g} = \frac{g_o - \alpha_m - \alpha_i}{a_o + \alpha_m + \alpha_i} \qquad (3\text{-}6)$$

here α_m is mirror loss described by the classic equation [15]:

$$\alpha_m = \frac{1}{2L}\ln\left(\frac{1}{R_1 R_2}\right) \qquad (3\text{-}7)$$

where R_1 and R_2 are the reflection coefficients at the laser facets, and L is the cavity length. The mirror loss was calculated based on HR(95%)/AR(5%) coated facets and an 8.0-mm cavity and found to be 1.9 cm^{-1}. Using the modal gain and loss data presented in Tables 1-4, all of the parameters that appear in Eqns. (3-5) and (3-6) can be accurately determined. In the following section the resulting modeled stability maps are presented.

3.3 Modeled Mode-Locked Stability Maps

Here we present the anticipated operational range of the ZLG788 series two-section quantum dot passively mode-locked lasers based on gain and loss profiles measured on the ZLG788A multi-section single pass emitter. This section includes a treatment of the ground state and excited state mode-locking regimes. These maps are referenced again in chapter 5 in which an in-depth study of the physical parameters that most strongly impact pulse stability are discussed. Following the methodology of section 3.2, the stability map in Fig. 3-4 was generated for the case of 0 V applied to the saturable absorber, over the full range of examined temperatures. The characteristic function describing the threshold conditions for lasing shown in Eqn. (3-6) sets the upper-bound in Fig. 3-4 while Eqn. (3-5) determines the lower bound. Devices having absorber to gain length ratios that fall within the bounds of the curves in Fig. 3-4 are predicted to produce mode-locked pulses for a given temperature. This represents the operable range of our stability maps. The dotted horizontal lines then depict the absorber to gain section length ratios of the quantum dot mode-locked lasers used in this study; previously presented in chapter 2.

It is generally noted that the path toward achieving better temperature performance in an MLL involves moving to a shorter absorber length. As a result, the device having L_a/L_g=0.11 is anticipated to have the best temperature performance. The analytical model predicts that in all cases, with the exception of 20 ℃ and L_a=0.8-mm, the devices studied are in a region that is limited by the threshold condition rather than the mode-locking stability condition in Eqn. (3-5). The physical implications of this are discussed in chapter 5. Stability maps have also been constructed for the remaining voltages (-1 through -7 V);

these maps are presented in *Appendix C*. The dashed boundaries in Fig. 3-4 represent regions where mode-locking from the first ES was observed. In these regions, Eqn. (3-1) was fitted to the ES net gain peak, and the values of g_{max} and a_0 reflect the maximum gain and unsaturated absorption in the ES, respectively. A direct comparison of the model predictions at the GS and the ES for higher temperatures is shown in Fig 3-5. For 100 ºC and higher, the model indicates that the devices used in this study fail to meet the threshold condition in the GS. Conversely, for high current densities, lasing from the excited state is expected up to 110 ºC for the device having L_a=0.8-mm, and up to 100 ºC for the device having L_a=1.0-mm. One can see that the horizontal dotted lines in Fig. 3-5, representing the absorber to gain length ratios of these devices, intersect the ES maps only.
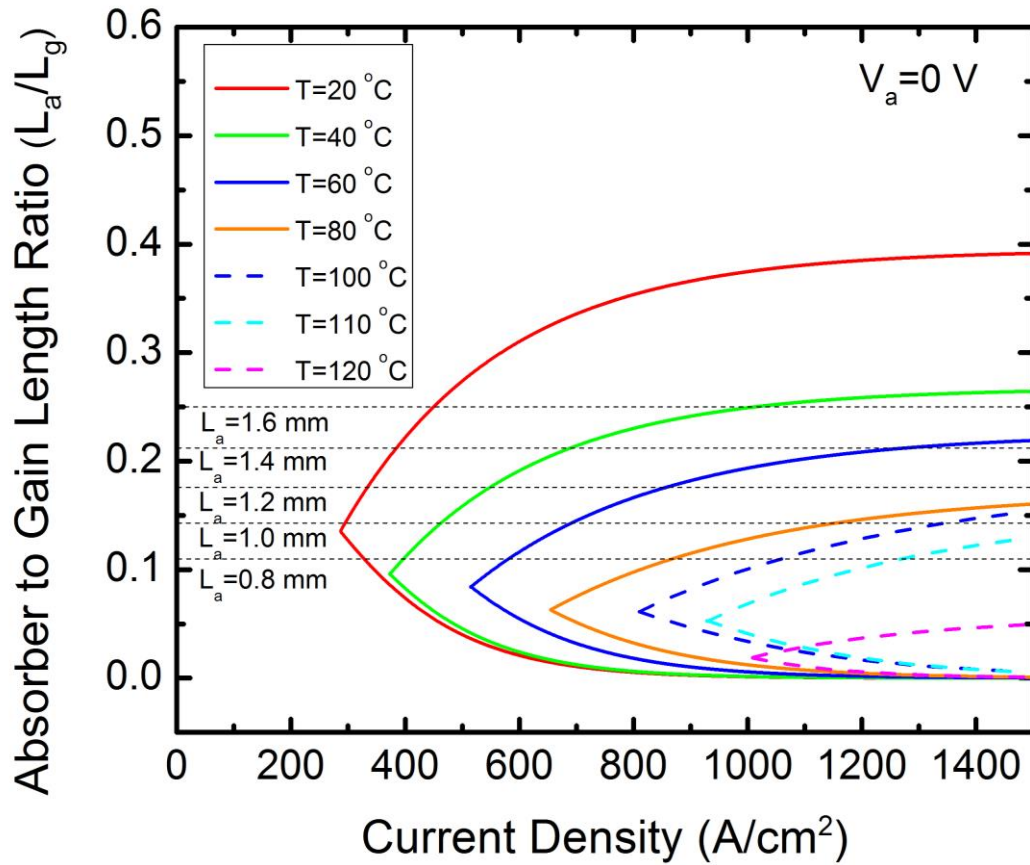
Figure 3-4. Mode-locking stability map for 0 V applied reverse bias as determined from Eqns. (3-5) and (3-6) using the measured GS gain and absorption data, solid plots and measured ES gain and absorption data, dashed plots. The horizantal dashed lines represent the absorber to gain length ratios of the devices used in this dissertation.
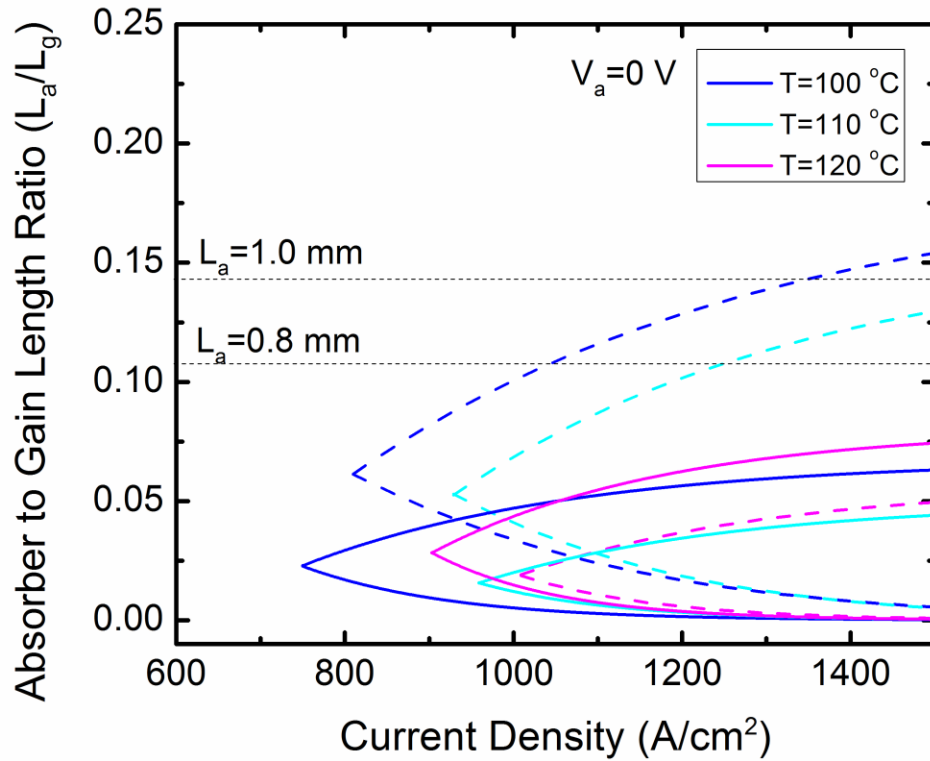
Figure 3-5. Comparison of model predictions from the ground state (Solid lines) and the excited state (dashed lines) for 100 to 120 $^{\circ}$C with grounded saturable absorber. The horizantal dashed lines represent the absorber to gain length ratios of the devices used in this dissertation.

In the final section of chapter 3 we examine methods for optimization of the operational range of a mode-locked laser for different device characteristics. The predictive capability of the model is an area of considerable interest. In this section the utility of the model as a tool to influence the growth and processing of future mode-locked laser designs is investigated.

3.4 <u>Predictive Capabilities for Next Generation Designs</u>

We now turn our focus to examining the potential implications of our model and consider which parameters could be adjusted to move us into a regime of shorter pulse Full Width Half Maximum (FWHM) or more stable operation. In Figs. 3-4 and 3-5, the resulting curves from Eqns. (3-5) and (3-6) are cut off for current density values below the intersection point of the lower and upper bound conditions. In Fig. 3-6 the full range of Eqns. (3-5) and (3-6) is shown for the case of T=60 $^{\circ}$C. Modification of the model parameters and the resulting effects on the range of mode-locked operation is now discussed. Firstly, we note that the high current range can be significantly improved with an increase in maximum gain (g_{max} – blue dashed line); this could be accomplished, for instance, with p-type doping of the dots [16]. Secondly, from Fig. 3-6 it is evident that the onset of mode-locking can be shifted to lower current density with a reduction in transparency current density (J_{tr} – red dashed line); in contrast to the approach for increasing g_{max}, reduction in J_{tr} is accomplished with n-type doping [16]. Finally, we find that the lower bound curve, described by Eqn. (3-5), comes to a peak at lower currents. This peak is found to increase in magnitude with decreasing unsaturated absorption (a_o). Note that from Table 4 that the minimum value of a_o was observed at T=60 $^{\circ}$C. The positive

implications of this will be discussed in greater detail in chapter 5. As it relates to this discussion, we find that the lower bound peak maximizes at 60 ^{o}C when a_o is lowest. Optimization of these parameters presents a great opportunity for maximizing the operational range in accordance with the modeled stability maps and potentially reveals the path toward achieving more stable mode-locking for a given temperature.

All other things being equal, a device with a longer absorber will produce a higher quality pulse train as a result of more interaction length, which allows for increased pulse trimming. Accordingly, it is desirable to use a device with a larger absorber to gain length ratio provided that the threshold condition is still met. Additionally, the best quality pulses occur at lower current densities; typically close to threshold to avoid non-linear effects such as Self-Phase-Modulation (SPM) [17]. Therefore, it follows that the optimum operating condition occurs at the intersection of the upper and lower bound curves; Eqns. (3-5) and (3-6), which we referred to as the point of maximum stability. By modifying our parameters in accordance with the results from Fig. 3-6, it is possible to shift the point of maximum stability closer to the peak of the lower bound curve. By operating in a regime wherein this peak is maximized, we increase the potential performance of the device by virtue of the fact that the point of maximum stability occurs for a larger absorber to gain length ratio.

The analytical theory presented in this chapter adds critical insight not only into the proper design of two section mode-locked lasers, but into the design of future devices as well. In chapter 4, results are presented from experiments designed to examine the current

and voltage biasing regimes that produce stable mode-locking over a wide range of temperatures. In particular, verification of the model predictions for the temperature of maximum operation and the regions of ES vs. GS mode-locking is sought.
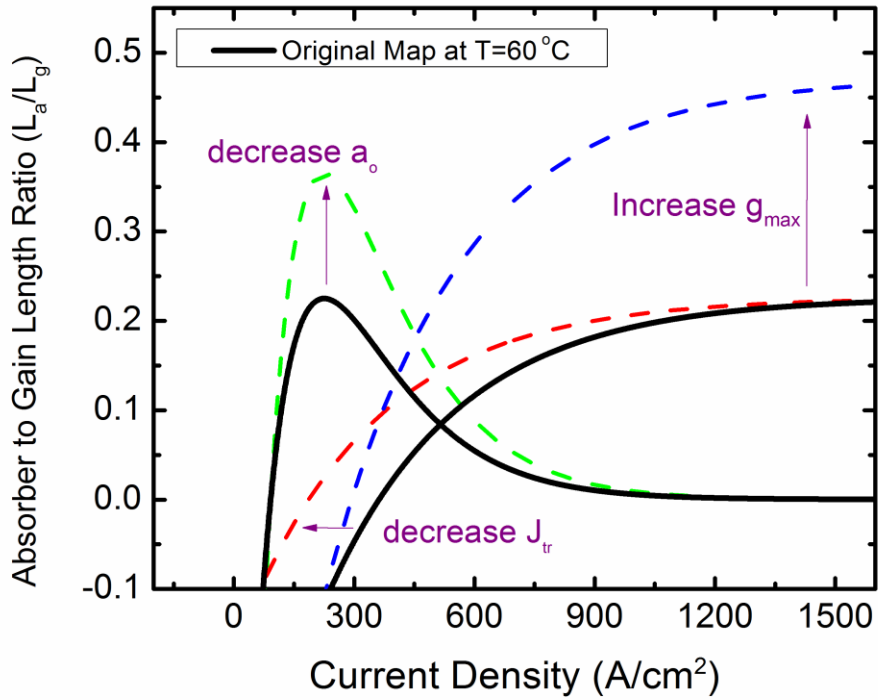
Figure 3-6. Mode-lock stability map for V=0 V applied to the absorber at T= 20 ^{o}C. Dashed line represent the theoretical results after altering the max gain (blue), the transparency current density (red), and the unsaturated absorption (green).

REFERENCES FOR CHAPTER 3

[1] A. G. Vladimirov and D. Turaev, "New model for mode–locking in semiconductor lasers," Radiophys. Quantum Electron., vol. 47, pp. 769–776 (2004)

[2] A. G. Vladimirov and D. Turaev, "Model for passive mode–locking in semiconductor lasers," Phys. Rev. A, vol. 72, pp. 033808-1–033808-13, (2005)

[3] Raghunathan, R.; Crowley, M.; Grillot, F.; Li, Y.; Mee, J. K.; Kovanis, V.; Lester, L. F., "Pulse Characterization of Passively Mode-locked Quantum Dot Lasers Using a Delay Differential Equation Model Seeded with Measured Parameters." IEEE J. Selected Topics in Quantum Electron. No. 99, pp. 1 (2013)

[4] Y.-C.Xin, Y. Li, A. Martinez, T. J. Rotter, H. Su, L. Zhang, A. L. Gray, S. Luong, K. Sun, Z. Zou, J. Zilko, P. M. Varangis, and L. F. Lester, "Optical gain and absorption of QD measured using an alternative segmented contact method" IEEE J. Quantum Electron. 42, 725 (2006)

[5] P. Blood, G. M. Lewis, P. M. Smowton, H. Summers, J. Thomson, and J. Lutti, "Characterization of semiconductor laser gain media by the *s*egmented contact method" IEEE J. Sel. Top. Quantum Elect., 9, 1275 (2003)

[6] I. O'Driscoll, M. Hutchings, P. M. Smowton and P. Blood, "Many-body effects in InAs/GaAs quantum dot laser structures" Appl. Phys. Lett., 97, 141102-1 − 141102-3 (2010).

[7] L. A. Coldren, S. W. Corzine *Diode Lasers and Photonic Integrated Circuits ,*New York: Wiley, (1995)

[8] P. A. Wolff, "Theory of the Band Structure of Very Degenerate Semiconductors," Phys. Rev. 126, 405-412 (1962)

[9] M. T. Crowley, I. P. Marko, N. F. Masse, A. D. Andreev, S. Tomic, S. Sweeney, E. P. O'Reilly, and A. R. Adams, "The Importance of recombination via Excited States in InAs/GaAs 1.3 μm Quantum-Dot Lasers" IEEE J. Sel. Top. Quantum Elect., 15, 799–807 (2009)

[10] [23] MG Thompson, AR Rae, M. Xia, RV Penty, and IH White, "InGaAs Quantum-Dot Mode-Locked Laser Diodes," IEEE J. Sel. Top. Quan. Elect., 15, 661–672 (2009)

[11] C.-Y. Lin, Y.-C. Xin, Y. Li, F. L. Chiragh, and L. F. Lester, "Cavity design and characteristics of monolithic long-wavelength InAs/InP quantum dash passively mode-locked lasers," Opt. Exp., vol. 17, no. 22,pp. 19739–19748 (2009)

[12] M. T. Crowley, D. Murrell, N. Patel, M. Breivik, C.-Y. Lin, Y. Li, B.-O. Fimland, and L. F. Lester, "Analytical modeling of the temperature performance of monolithic passively mode-locked QD lasers" IEEE J. Quantum Electron. 18, 1059-1068 (2011)

[13] K. Lau, and J. Paslaski, "Condition for short pulse generationin ultrahigh frequency mode-locking of semiconductor lasers," IEEE Photon Technol. Lett., vol. 3, no. 11, pp. 974–976 (1991)

[14] J. Palaski, and K. Y. Lau, "Parameter ranges for ultrahigh frequency mode-locking of semiconductor lasers. Appl. Phys. Lett. vol. 59, no. 1, pp. 7-9 (1991)

[15] Jia-Ming Liu, Photonic Devices (Cambridge University Press, New York, 2005)

[16] Vahala, Kerry J.; Zah, C.E., "Effect of doping on the optical gain and the spontaneous noise enhancement factor in quantum well amplifiers and lasers studied by simple analytical expressions," Applied Physics Letters , vol.52, no.23, pp.1945-1947 (1988)

[17] G. P. Agrawal, and N. A. Olsson, "Self-phase modulation and spectral broadening of optical pulses in semiconductor laser amplifiers," IEEE J. Quantum Elect., vol. 25. no. 11 (1989)

Chapter 4 – Experimental Study of the Operational Range

With careful consideration of the analytical theory presented in chapter 3, this chapter deals with development of a set of experiments designed to verify the model predictions and examine device characteristics over a broad range of operating temperatures. In section 4.1, state-of-the-art the experimental setup and methodology is presented. Experiments have been designed to examine temporal, optical and frequency domains. In section 4.2, the construction of the experimental operational maps is presented, and the key features of the maps are identified. This section directly contrasts the experimental observations with the analytical model predictions. Subsequently, in sections 4.3 – 4.5 the optical spectrum, electrical spectrum and time domain characteristics are presented across a wide range of biasing conditions and temperature variation. Key features such as optical spectrum transitions from ground-state to excited-state, the evolution of the time-bandwidth product with temperature and non-linear effects such as pulse splitting are presented and discussed in detail.

4.1 Experimental Setup

The experiments presented in this chapter were conducted on the ZLG788B series of two-section quantum dot passively mode-locked lasers. As described in chapter 2 the lasers have been individually mounted onto AlN carriers for improved thermal conductivity and increased mechanical stability. They are placed on a vacuum stage with a large thermal mass. The temperature of the laser is controlled by a thermo-electric (TE) cooler. An ILX 3811 current source applies current to the anode contact above the ridge waveguide. A reverse bias from 0 to -7 V is applied across the saturable absorber, this is used to alter

absorber recover times which can be reduced from 100's fs with 0V to 10's fs with -7V [1] . Light is coupled into a polarization maintaining single mode fiber using a set of collimating lenses, and an isolator is incorporated to minimize feedback into the laser cavity. A 50 GHz HP 8565E electrical spectrum analyzer enables the characterization of the pulse train in the frequency domain. A high-speed photodiode is used for the optical-to-electrical conversion. The optical domain is characterized with an Ando AQ6317B optical spectrum analyzer. The MLL output is also captured in the temporal domain with a 140 GHz Tektronix DSA 8200 sampling oscilloscope. In contrast to autocorrelation, which suffers from loss of detail regarding pulse shape [2], the high speed sampling scope resolves details of pulse asymmetry; however, it is limited to a minimum pulse width of ~7 ps. This is due to the fact that the measured pulse width from the oscilloscope is actually the convolution of the optical pulse, and the sampling gate, which has a width of 7.1 ps. To address this issue, a state-of-the-art Frequency Resolved Optical Gating (FROG) system has been developed for characterization of pulse shape and chirp from a quantum dot mode-locked laser [2,3]. Pulse characteristics captured using this technique will be introduced in chapter 5. For the purpose of constructing the operational maps in section 4.2, device characteristics were effectively captured with the high speed oscilloscope. It is noted that the optical pulse and the sampling gate are assumed to be Gaussian in nature. As such, the actual pulse width is estimated using the deconvolution formula [4]:

$$\tau_{act}^2 = \tau_m^2 - 50.4$$
(4-1)

where τ_m is the measured pulse width according to the oscilloscope, and τ_{act} is the actual pulse width after the deconvolution. It is also noted that due to the high level of asymmetry in some optical pulses, the approximation in Eqn. (4-1) can induce some error; however, the operational maps presented in section 4.2 are for stable pulse trains that are well approximated by a Gaussian profile. A visual schematic of the experimental setup described in this section is presented in Fig. 4-1. The blue dashed lines in the schematic represent alternative configurations of the polarization maintaining (PM) fiber. The orange dashed line represents an alternative configuration of the SMA cable. Although measurements from the auto-correlator and the FROG are not presented until chapter 5, they have been included in Fig. 4-1 for completeness.
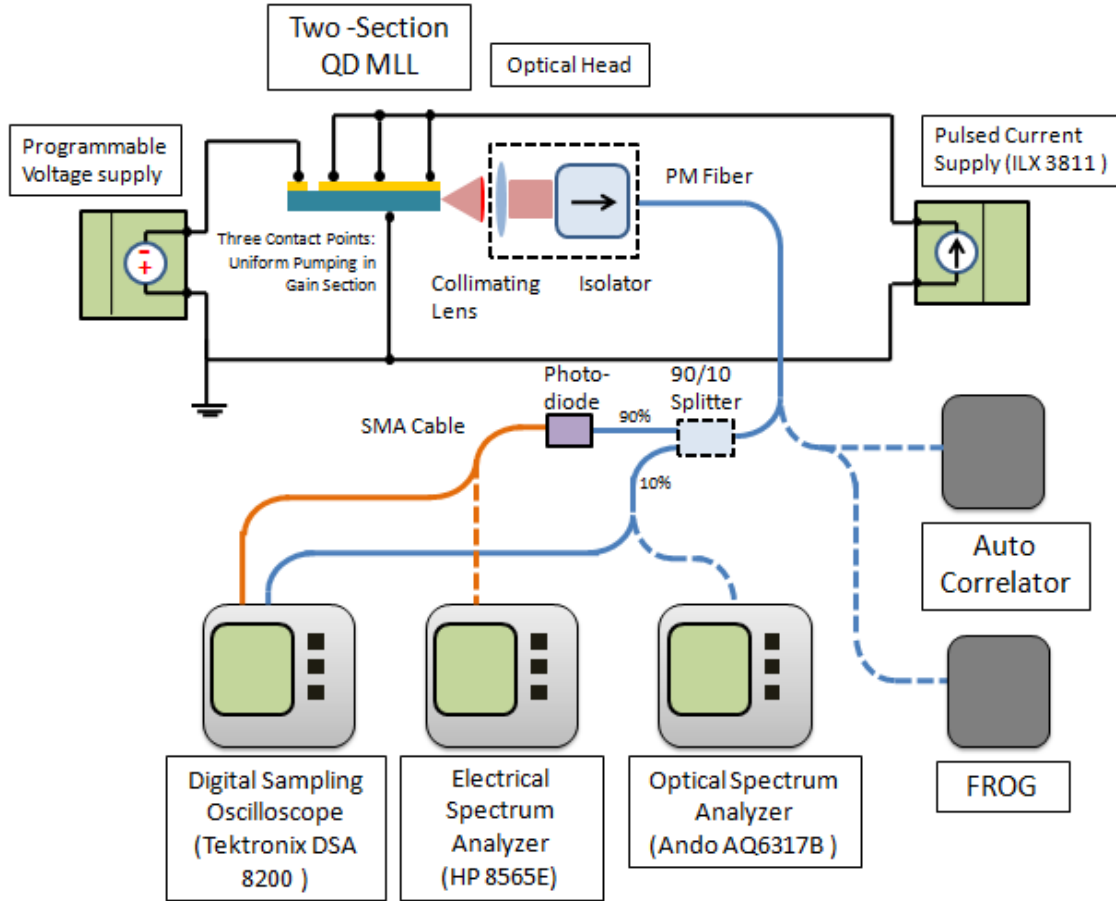
Figure 4-1. Schematic drawing of the experimental setup used to characterize two-section quantum dot (QD) passively mode-locked lasers (MLL). The Dashed lines represent alternative configurations of the cabling.

4.2 Experimental Mapping of Device Operational Range

To examine the accuracy of our predictive model, a detailed characterization of the pulse train output in the temporal domain is performed. At each temperature, and for incremental voltages from 0 to -7 V, the laser injection current was swept from below laser threshold, up to 500 mA– equal to a current density of 1.428 kA/cm^2. This current was selected as a maximum to avoid potential damage to the device. The regions of fundamental mode-locking (5 GHz) were recorded where the measured pulse width (τ_m) was less than 20 ps, equal to an actual pulse width (τ_a) of ~18.7 ps according to Eqn. (4-1). In addition to examination of the pulsed output in the temporal domain, the frequency and optical domains were characterized at the key biasing conditions that bounded the contours of the operational maps. This allowed determination of the electronic state from which the device was lasing, the 3-dB bandwidth of the optical spectrum, and provided added insight into the quality of mode-locking. This data will be presented in detail in sections 4.3 and 4.4.

In Fig. 4-2 the resulting operational map for the device having a saturable absorber length of 0.8-mm (788B AH3) is shown. The regions within the contours represent the current and voltage combinations that produce τ_a<18.7 ps. The laser continued to pulse outside these contours but with longer pulse durations. In many cases, unusual pulse dynamics such as pulse splitting [3], and harmonic mode locking [5] were observed outside the contours of Fig. 4-2. A more detailed investigation into these regimes will be reported in chapter 5.
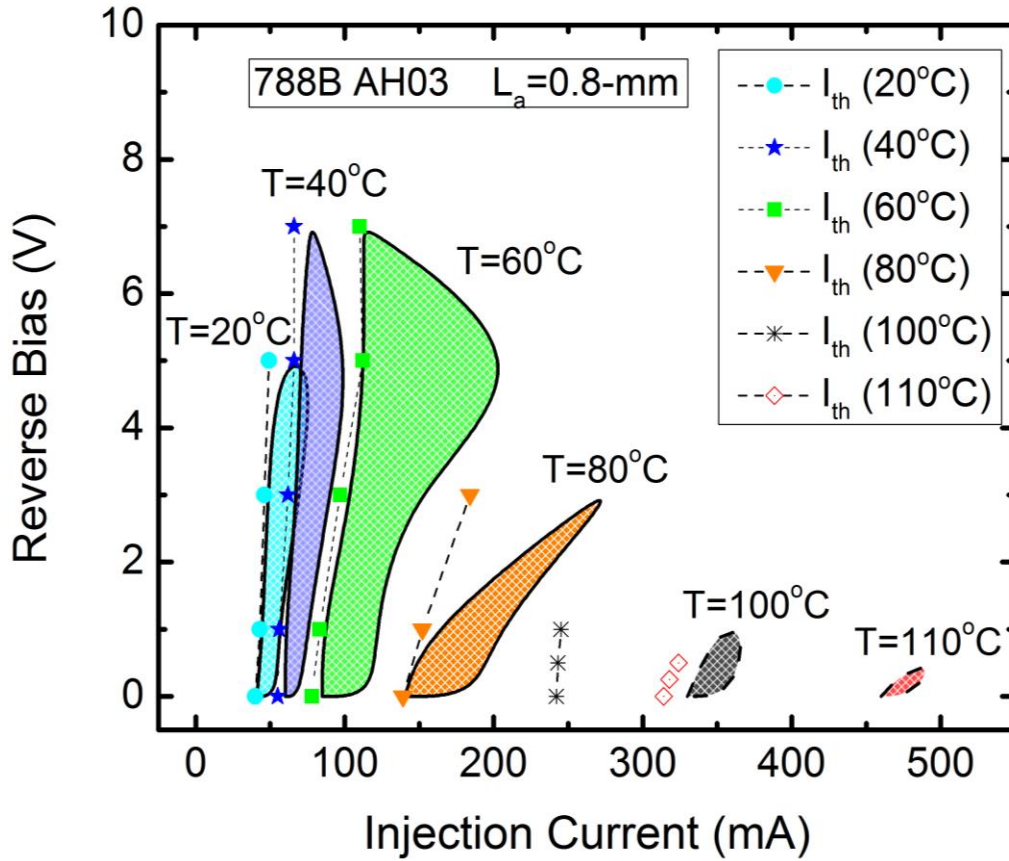
Figure 4-2. Contour maps depicting the regions of fundamental mode-locking (5 GHz) where the measured FWHM of the optical pulse was less than 18.7 ps for a two-section mode-locked laser having saturable absorber length, L_a=0.8-mm. The plotted symbols show the threshold current at each temperature and reverse voltage. At 0V applied to the saturable absorber, the threshold currents were 40, 55, 78, 139, 242 and 314 mA at 20, 40, 60, 80, 100 and 110°C, respectively.

Comparing experimental results in Fig. 4-2 to the analytical predictions shown in Fig. 3-4 (presented in completeness in *Appendix C*), excellent agreement is found, clearly demonstrating the capability to accurately predict temperature of maximum operation for a wide range of absorber voltages. As an example, from examination of Fig. 3-4, the device having L_a=0.8-mm was expected to operate up to 110 °C when the saturable absorber was grounded. This prediction was positively validated by the experiments conducted on the 788B AH03 device; shown in Fig. 4-2. This is currently the highest known temperature operation from a monolithic quantum dot mode-locked laser [6]. Previous work has shown operation of quantum well mode-locked lasers up to 90 °C [7], and quantum dot mode-locked lasers up to 80 °C [8].

The symbols in Fig. 4-2 represent the measured threshold current values for each combination of temperature and absorber bias. One can observe that from 20 to 60 °C these hug the contours of the measured onset of mode-locking, whereas at higher temperatures they begin to deviate from the contours and a significant injection current above threshold is required to generate pulses. The current above threshold where pulses were observed at 110 °C was $1.5 \times I_{th}$ which equates to ~185 mA above threshold. This trend is related to the transition from ground-state (GS) to excited-state (ES) operation. It is found that the onset of pulsing from the GS occurs near threshold, while the onset of pulsing from the ES occurs at injection current values that are well above threshold. Examination of the optical spectrum, introduced in the next section, verifies that between 80 °C and 100 °C, the laser emission wavelength switched to the ES. This result undoubtedly confirms our analytical

model predictions shown in Fig. 3-4 regarding the transition point from GS to ES mode-locking.

In Figs. 4-3 through 4-6, the experimental operational maps are presented for the remaining devices; L_a=1.0-mm, L_a=1.2-mm, L_a=1.4-mm and L_a=1.6-mm, respectively. Relating these maps back to the predictions for the 0V case presented in Fig. 3-4, it is clearly seen that the maximum operational temperature is correctly predicted for all absorber lengths. Furthermore, in comparing the maximum operating temperature across all voltages examined, to the complete set of operational maps presented in *Appendix C*, excellent agreement is observed. This serves as strong evidence that the analytical theory presented in chapter 3 has a high level of physical merit. A final noted consequence of the device containing a L_a=0.8-mm absorber length is that the optimum operating temperature occurs around 60 ^{o}C. Improvement in device characteristics at higher temperatures has been previously noted [9,10], but was not fully understood. In this dissertation, the physical mechanisms that result in improved operation at higher temperatures have been discovered to be strongly associated with temperature dependent tuning of the gain and absorption. This will be discussed in greater detail in chapter 5. In the remaining sections of chapter 4, the optical, electrical and temporal characteristics of mode-locked laser are given, and the key features therein are discussed.
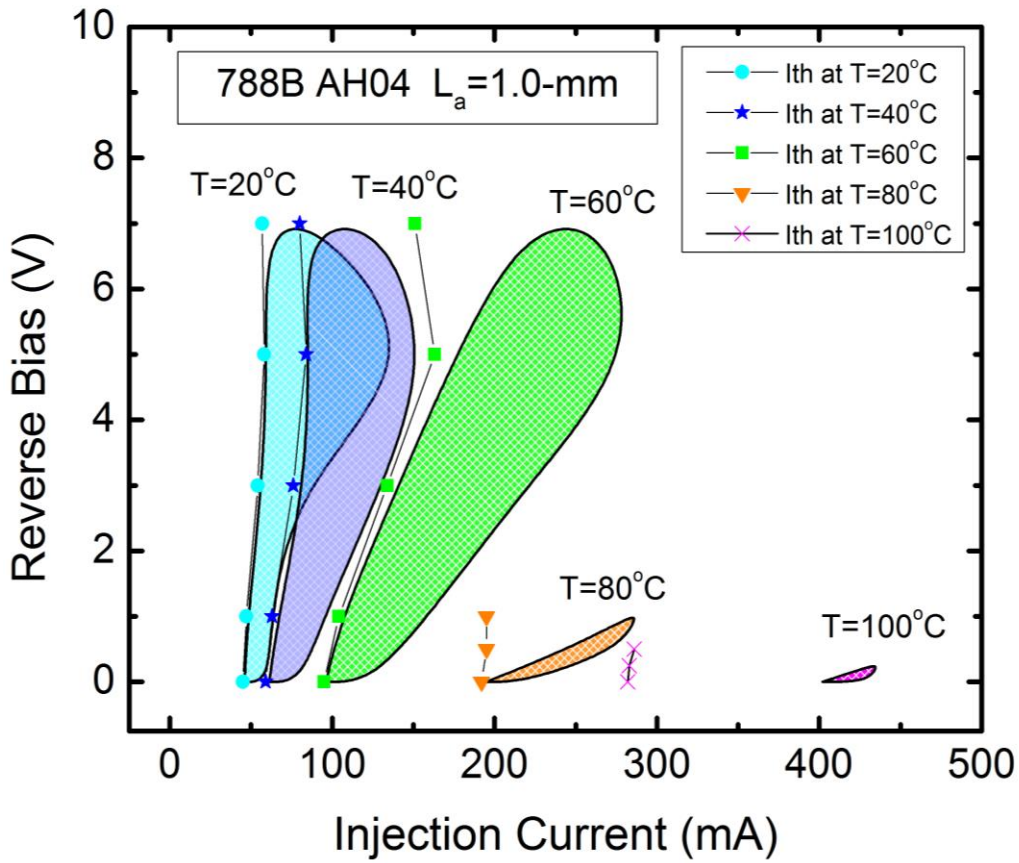
Figure 4-3. Contour maps depicting the regions of fundamental mode-locking (5 GHz) where the measured FWHM of the optical pulse was less than 18.7 ps for a two-section mode-locked laser having satruable absorber length, L_a=1.0-mm. The plotted symbols show the threshold current at each temperature and reverse voltage.
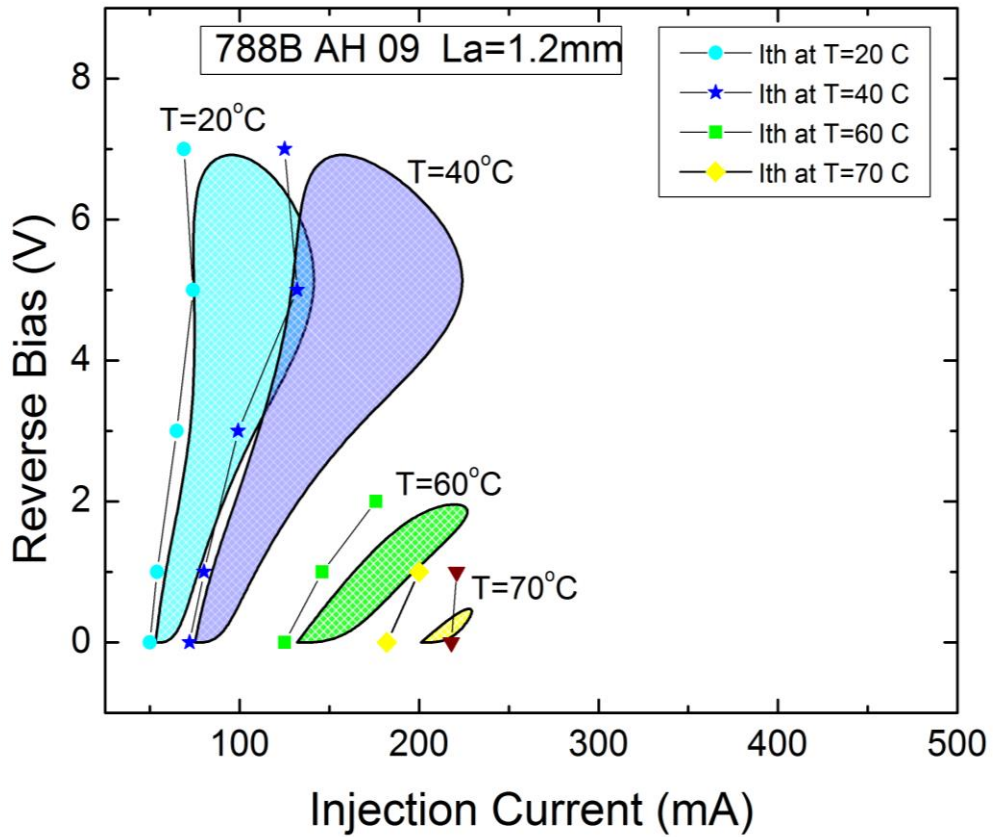
Figure 4-4. Contour maps depicting the regions of fundamental mode-locking (5 GHz) where the measured FWHM of the optical pulse was less than 18.7 ps for a two-section mode-locked laser having satruable absorber length, L_a=1.2-mm. The plotted symbols show the threshold current at each temperature and reverse voltage.
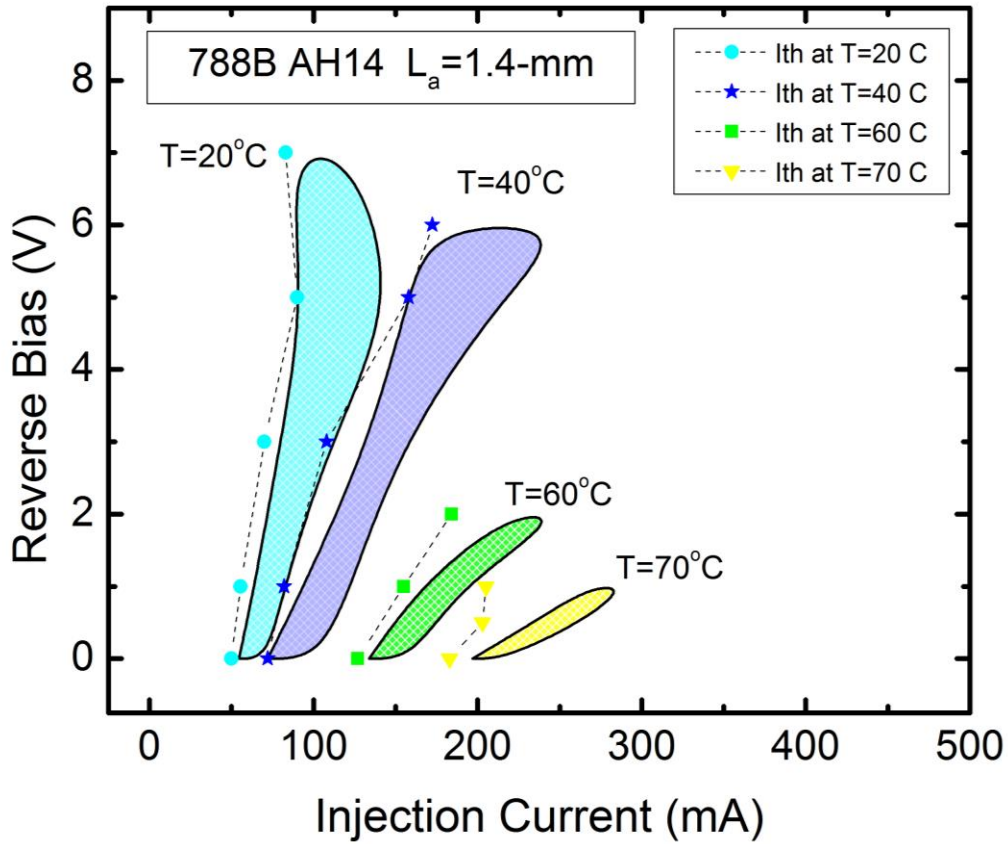
Figure 4-5. Contour maps depicting the regions of fundamental mode-locking (5 GHz) where the measured FWHM of the optical pulse was less than 18.7 ps for a two-section mode-locked laser having satruable absorber length, L_a=1.4-mm. The plotted symbols show the threshold current at each temperature and reverse voltage.
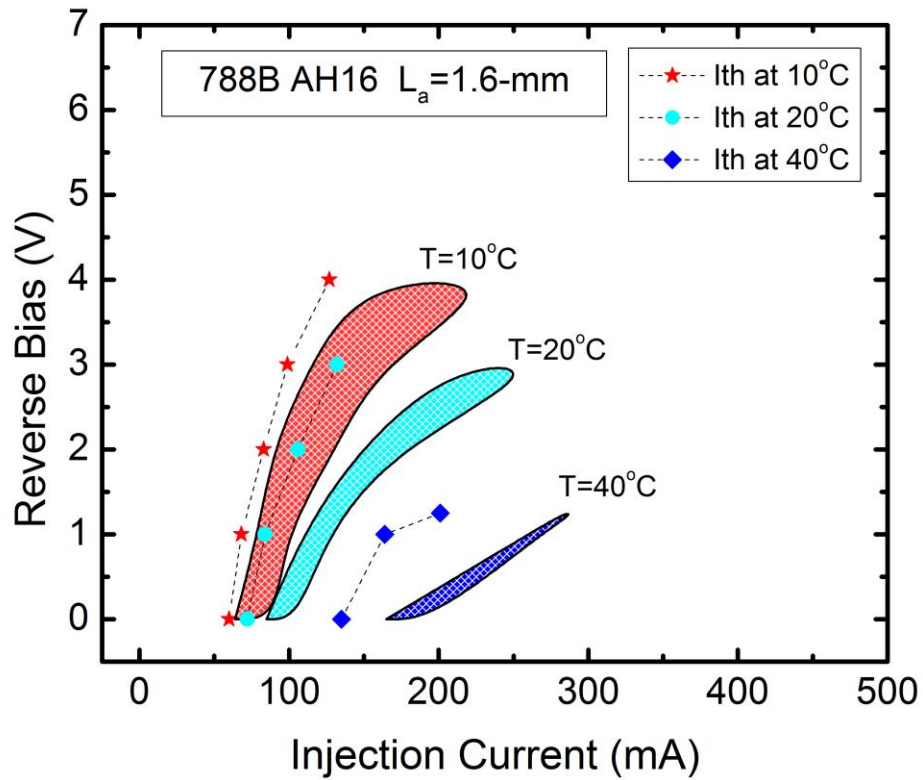
Figure 4-6. Contour maps depicting the regions of fundamental mode-locking (5 GHz) where the measured FWHM of the optical pulse was less than 18.7 ps for a two-section mode-locked laser having satruable absorber length, L_a=1.6-mm. The plotted symbols show the threshold current at each temperature and reverse voltage.

4.3 <u>Optical Spectrum Characteristics</u>

In this section the optical spectrum characteristics of the two section quantum dot mode locked lasers are explored which includes a study of the temperature dependence of the optical spectra as well as the transition from GS to ES operation. The majority of the spectra discussed in this section are from the short absorber device (788B AH03, L_a=0.8-mm) given that this device has demonstrated the best temperature performance. The corresponding temperature dependent optical spectra for the remaining devices are shown in *Appendix D*.

In Fig. 4-7, the temperature-dependent optical spectra are presented for the case where the saturable absorber is grounded (0V). Each of these spectra corresponds to the shortest measured pulse at 0 V. The forward injection currents for these spectra are 55, 70, 80, 145, 350 and 450 mA at 20, 40, 60, 80, 90, 100 and 110 ºC, respectively. The device maintains ground state operation from 20-92 ºC (solid lines in Fig. 4-7), exhibits dual mode [11] operation from 93-98 ºC and then switches to excited state (ES) operation above 98 ºC (dashed lines in Fig. 4-7). The dual mode lasing can be bypassed by increasing the reverse bias to ~1 V on the saturable absorber. This forces the device into single wavelength operation from the ES. In section 4.5 we will examine the quality of the optical pulses emitted from different lasing states including dual mode operation. The mode-locked spectra cover a wavelength span from 1217 to 1265 nm over the complete range of temperatures. The observed ranges of wavelengths are compatible with Si-Ge alloy detectors; the short wavelength extreme (~1220 nm) represents the shortest practical wavelength for Si-based waveguides since it avoids excessive absorption [12].

Upon further observation of Fig. 4-7, it is found that the 3-dB bandwidth of the optical spectrum is narrowing as the device is taken to higher temperature. The corresponding 3-dB bandwidths are 377.7, 452.1, 246.8, 198.6, 1031, 774.7 GHz at 20, 40, 60, 80, 100 and 110 $^{\circ}$C respectively. It is not immediately evident if this is beneficial or not, given that the Fourier limited pulse width goes as the inverse of the optical bandwidth, however, reduced optical bandwidth does appear to coincide with expanded range of operating conditions that produce narrow pulses according to Fig. 4-2, and could be an indication of reduced broadening from SPM [13]. The underlying cause for optimization at elevated temperatures is associated with temperature-dependent tuning of the gain and absorption values at the lasing wavelength, which is a topic of chapter 5. The voltage dependence of the optical spectra at a constant temperature and injection current density is shown in Fig. 4-8. It is found that the application of the reverse bias tends to shift the peak emission from the laser to a shorter wavelength. In contrast to the absorption peak which, as determined from the modal absorption profile, is red-shifting with increasing reverse voltage. The voltage dependence of the GS to ES transition is also evident from Fig. 4-2 and 4-3 at 80 $^{\circ}$C, and in Fig. 4-5 at 70 $^{\circ}$C wherein the pulses are observed from the GS at 0 V but transition to ES under application of reverse bias.
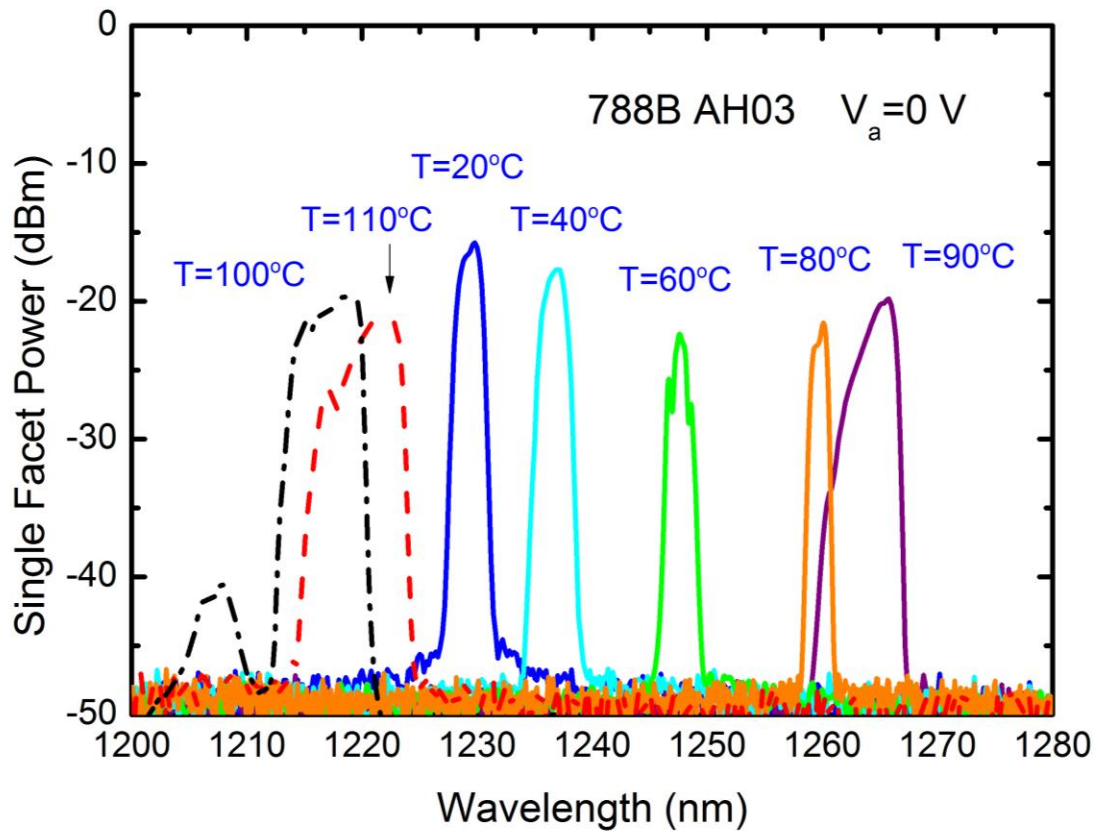
Figure 4-7. Measured optical spectra over temperature corresponding to the shortest measured pulses for the absorber grounded in all cases. Solid lines show ground state operation, dashed lines represent excited state operation (100 ^{o}C: Dashed-dotted, 110 ^{o}C: dashed). The spectra were measured at 55, 70, 80, 145, 350 and 450 mA at 20, 40, 60, 80, 90, 100 and 110 ^{o}C, respectively. The corresponding 3-dB bandwidths were: 1.9 nm, 2.13 nm, 1.28 nm, 1.05 nm, 5.07 nm and 3.84 nm.
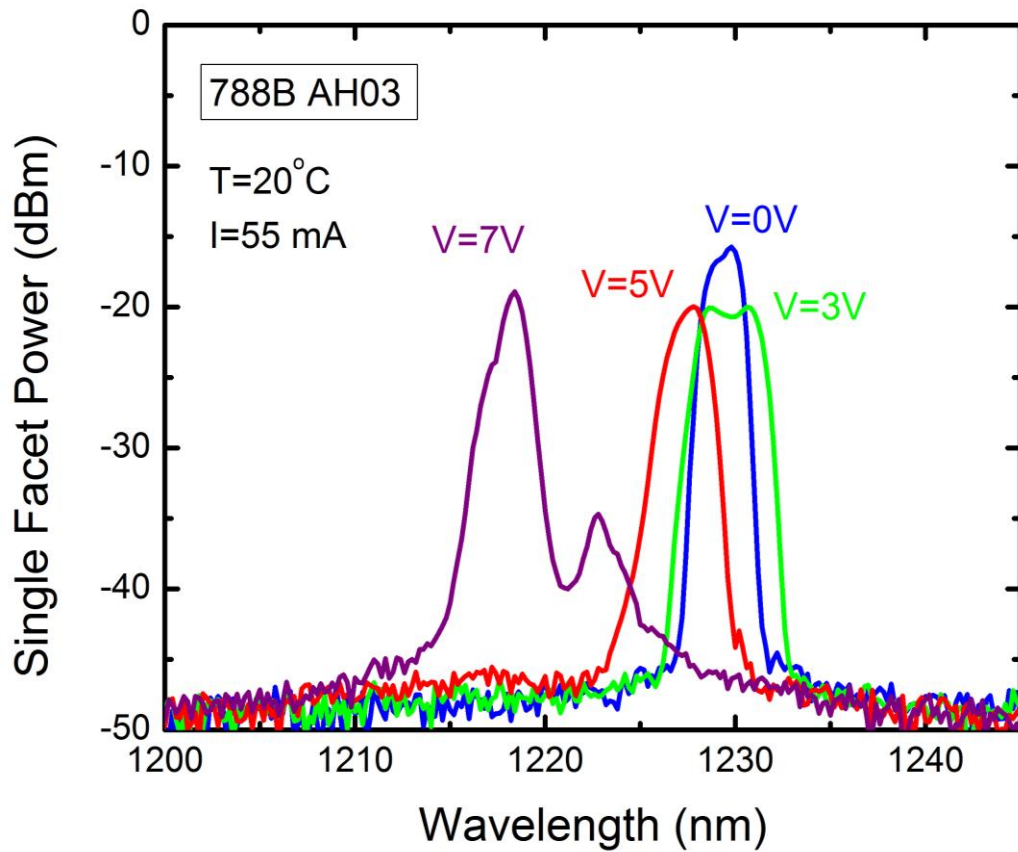
Figure 4-8. Measured optical spectra at T=20 °C for an injection current of 55 mA. The Absorber reverse voltage is varied from 0 to -7 V resulting in a shift in the laser peak emission to shorter wavelengths. The -7 V case (Purple solid line) exhibits dual mode operation.

A grounded saturable absorber is a common element to each of the devices tested over the range of temperatures which optical pulses are generated. It is observed that in each case there is a characteristic temperature where the device transitions from GS to ES operation. In Fig. 4-9 the corresponding grounded absorber transition temperatures are plotted for the full range of devices studied. Likewise, the resultant optical spectra are shown in Figs.4-10 through 4-12 for a variety of biasing condition around the GS/ES transition temperature on the devices having L_a=0.8-mm, 1.0-mm and 1.2-mm, respectively. From Fig 4-9, these transition temperatures are found to linearly decrease with increasing absorber length. The blue line in Fig. 4-9 is the resulting least squares fit which has a slope of dT/dL = -39.5 ℃/mm. Consequently, high temperature operation favors devices having low absorber to gain length ratios. This is consistent with the findings of the analytical model discussed in chapter 3. It has been experimentally shown that the L_a=0.8-mm device maintains fundamental MLL operation from the GS up to 93 ℃. To the best of our knowledge, this is the highest temperature that pulses from the GS of a quantum dot mode-locked laser have been demonstrated [14].

As a final observation, it can be seen in Fig 4-10 that there exists a region between the primarily GS or ES operation where hybrid lasing of the GS and ES peaks can occur. This effect has been previously observed by Rafailov *et. al.* [15]. This is typically only observed when operating at temperatures near the GS/ES transition point shown in Fig. 4-9. Under these conditions, competition between the ES pulses and GS pulses results in pulse broadening or even complete distortion of pulse shape. In section 4.5 the resulting temporal behavior will be presented for GS, ES and hybrid modes of operation.
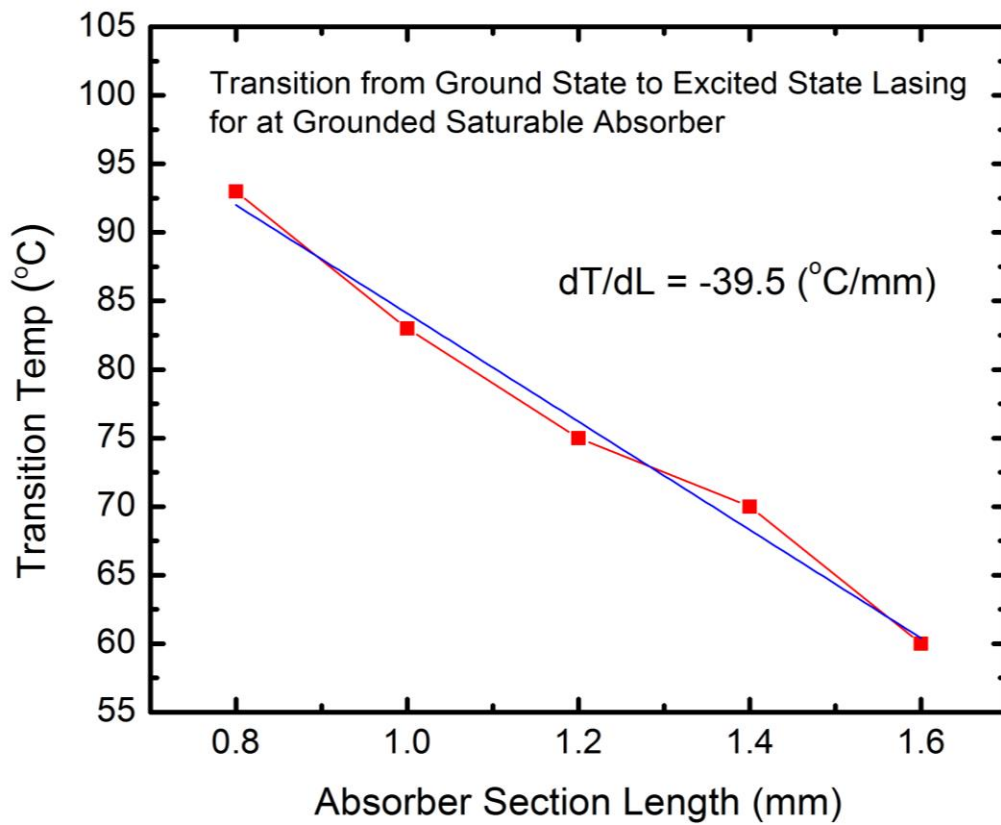
Figure 4-9. Measured transition temperature from ground-state to excited-state lasing for devices having total cavity length of 8.0-mm, but a varying saturable absorber length from 0.8-mm to 1.6-mm. The saturable absorber has been grounded in each case.
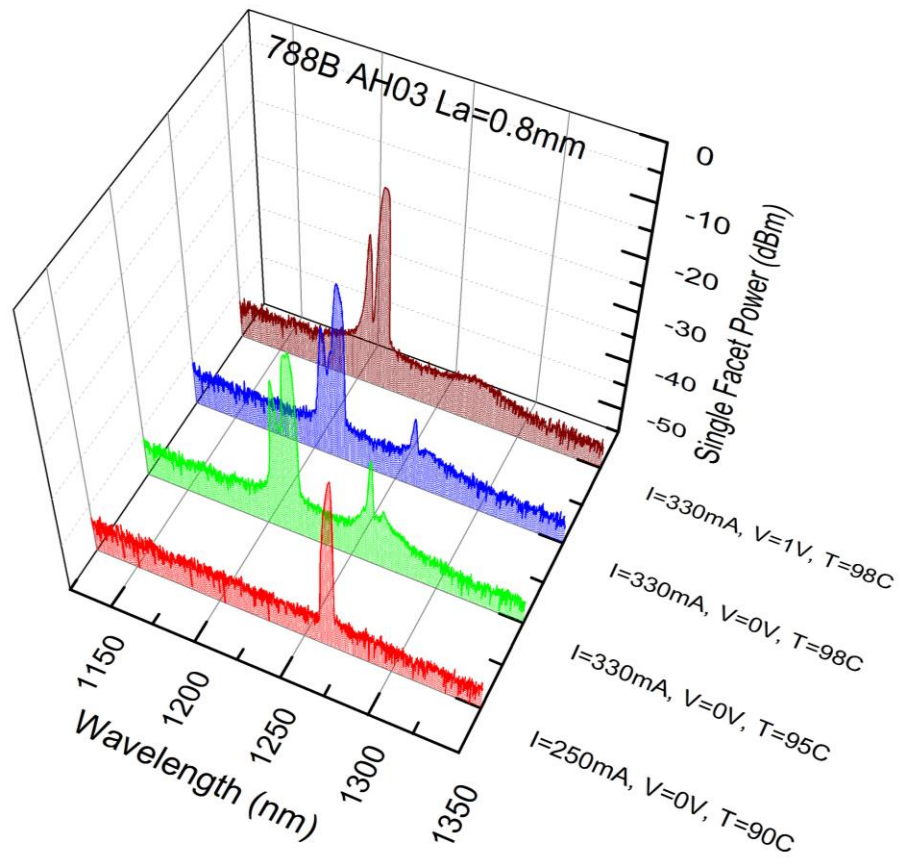
Figure 4-10. Measured optical spectra on the two-section MLL having L_a=0.8-mm absorber length. The temperature is increased from 90 to 98 $^{\circ}$C inducing a switch from ground-state to excited-state lasing.
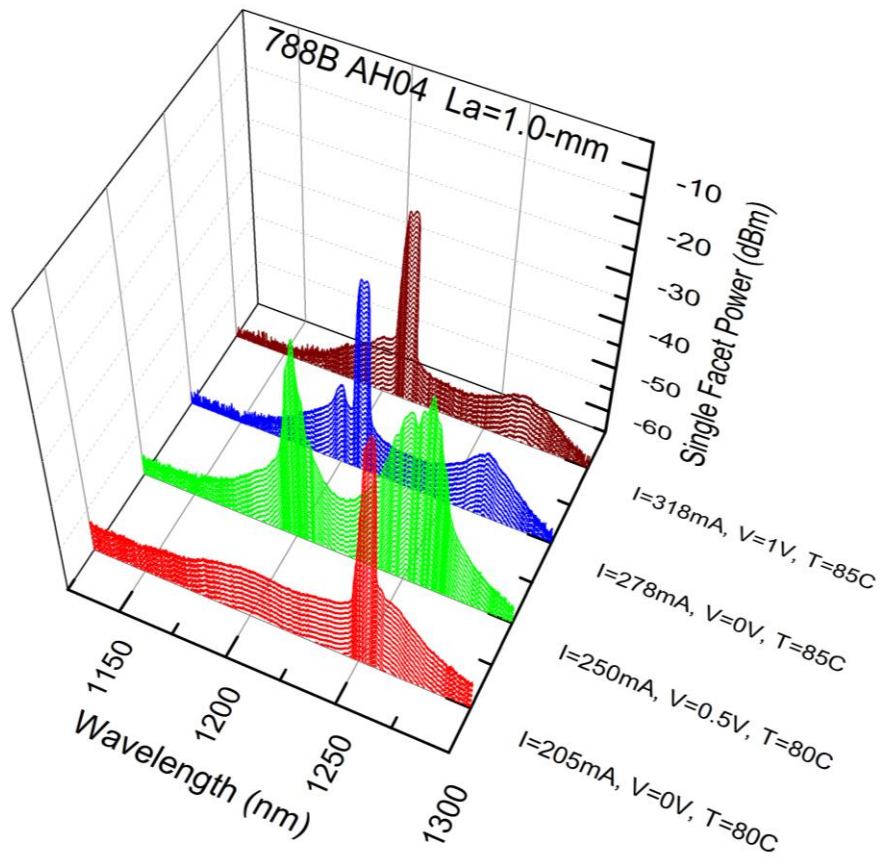
Figure 4-11. Measured optical spectra on the two-section MLL having L_a=1.0-mm absorber length. Temperature increased from 80 ^{o}C up to 85 ^{o}C which induced excited state mode-locking. Application of a small reverse bias at T=80 ^{o}C is shown to induce a hybrid lasing state.
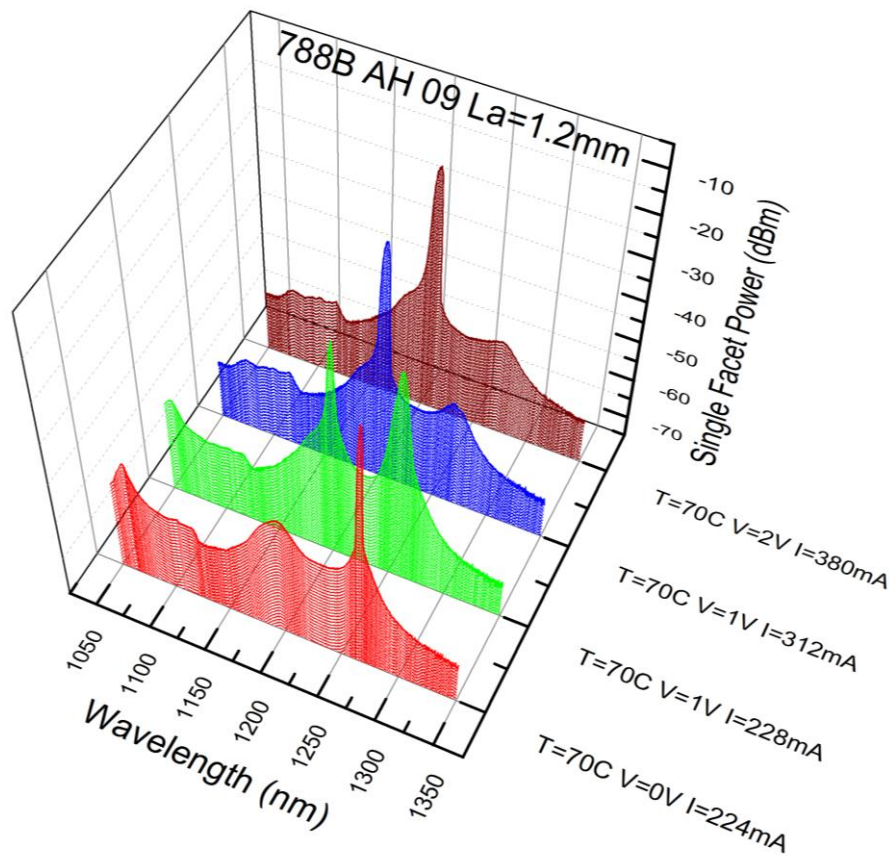
Figure 4-12. Measured optical spectra on the two-section MLL having L_a=1.2-mm absorber length. Temperature was kept constant at 70 °C. The transition for ground-state to excited state lasing is induced through application of a reverse bias on the absorber and inreasing the injection current.

4.4 <u>Electrical Spectrum Characteristics</u>

RF spectrum characteristics have been captured at the key biasing conditions that bounded the contour maps shown in Figs. 4-2 through 4-6. This was accomplished at all temperatures and for all devices discussed in this dissertation. In Fig. 4-13, the resulting spectra are shown for the short absorber (0.8-mm) device (788B AH03) across the full range of temperatures examined. A common operating point of 0 V applied to the absorber has been used in this representation. The forward injection currents at each temperature corresponded to those used to generate the optical spectra plots in Fig. 4-7. For the purpose of being concise, the electrical spectrum characteristics for the remaining devices have been omitted from this dissertation as the fundamental conclusions are the same.

The electrical spectrum characteristics can be used as a way of screening devices for possible stable mode-locking behavior. Although not as conclusive as a FROG measurement, the device is presumed to be sufficiently mode-locked when the fundamental and second harmonics exhibit at least 15-20 dB above the noise in the RF spectrum analyzer [16]. On average, the RF spectra for the pulses presented in Figs. 4-2 through 4-6 exhibited 5-6 harmonics with the SNR of the fundamental RF signal being greater than 37-dB. The typical RF linewidth for these devices in a free running condition can range from hundreds of kHz to a few kHz depending on the absorber bias and injection current conditions. The RF linewidth of these lasers can be dramatically improved through use of resonant feedback setups. It was previously shown that under stable resonant feedback the RF linewidth can be reduced to as low as 170 Hz [17]
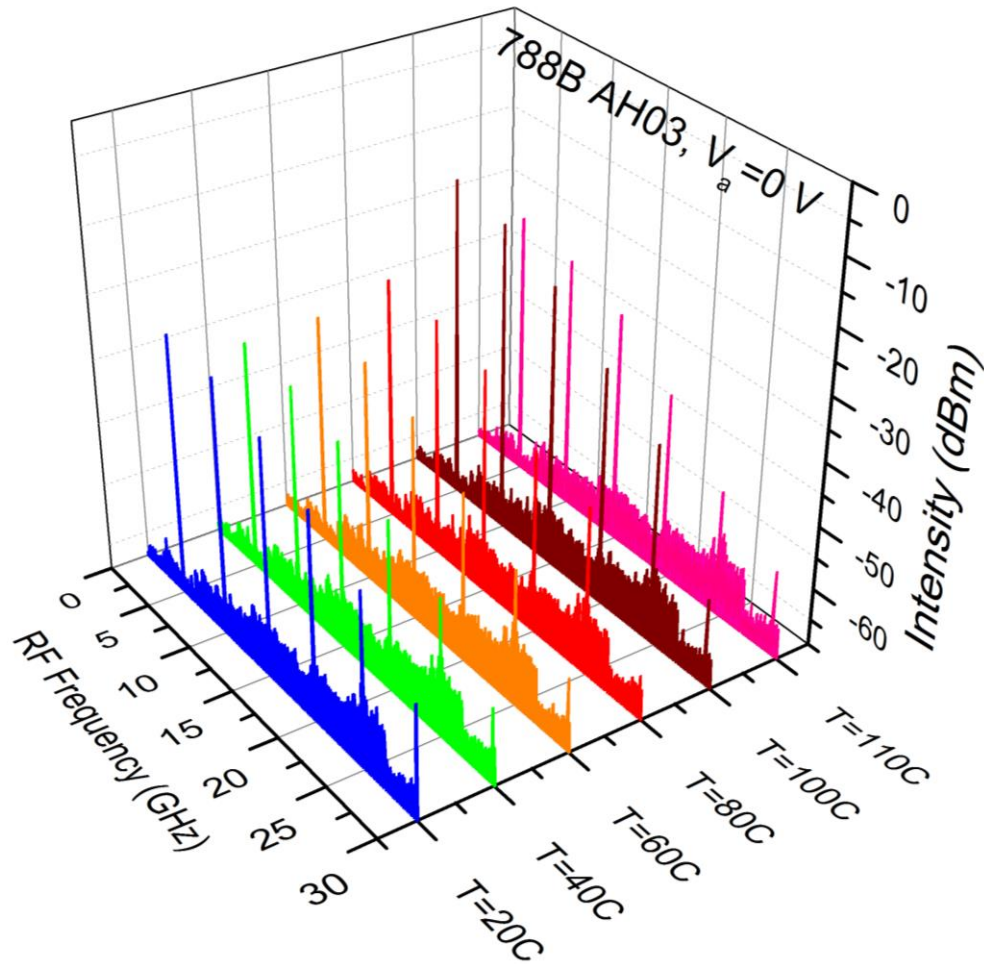
Figure 4-13. Measured electrical spectrum characteristics for a grounded saturable absorber and temperatures ranging from T=20 to 110 ºC. On average the RF spectrum exhibited 5-6 harmonics with the SNR of the fundamental RF signal being greater than 37-dB. The forward injection currents were 55, 70, 80, 145, 350 and 450 mA at 20, 40, 60, 80, 90, 100 and 110 ºC, respectively.

4.5 <u>Pulse Characteristics in the Temporal Domain</u>

In sections 4.3 and 4.2 it was shown that the device having a 0.11 absorber to gain-section length ratio (L_a=0.8-mm) was optimized for 60 °C operation. This was evident from an increase in the range of operation according to Fig. 4-2, and coincided with reduced 3-dB bandwidth in the optical spectra. In this final section of chapter 4 the temperature dependent time domain pulse characteristics, as measured with the 140 GHz Tektronix DSA 8200 sampling oscilloscope, are discussed.

a) Temperature Dependence of Optical Pulse Generation

Fig. 4-14 and 4-15 shows the measured temporal behavior of the optical pulse train over temperature corresponding to the optical pulse spectra of Fig. 4-7. With the saturable absorber grounded, the device is shown to produce mode-locked pulses across the full range of examined temperatures. The pulse period is 200 ps corresponding to fundamental mode-locking in the 8-mm laser cavity. The pulse's Full Width Half Maximum (FWHM) ranged from 8 to 19 ps across the temperature excursion. It is found that the temperature-dependent pulse durations have a minimum between 60 and 80 °C. With the freedom to increase the reverse bias at the absorber, the absolute shortest pulses measured were at 60 °C with -3 V on the absorber. This case produced a pulse train with 6.2 ps FWHM. The pulses between 60 and 80 °C are also shown to have the least intra-pulse energy, which is good evidence of improved mode-locked stability at the higher operating temperatures. From Fig. 4-14 and 4-15 the pulse asymmetry is clearly observed. The fast leading edge followed by a slow trailing edge is a result of strong absorption in the saturable absorber which sharply trims the leading edge of the pulse. The broadened pulse in the gain section

forms the slowly decaying tail of the trailing edge [2,18]. It is noted that for a short absorber device, the pulse width in the spatial dimension can be longer than the absorber itself. For example, assuming an effective group refractive index of 3.5 in the laser cavity, a 15 ps pulse will occupy 1.3-mm of longitudinal dimension within the cavity. That is longer than 3 out of the 5 absorber lengths studied in this dissertation. Accordingly, a scenario can exist where the pulse is never exclusively in the absorber section. This has interesting and significant impacts on the pulse characteristics. One would expect that the pulse width and chirp would be reduced in the longer absorber device due to more efficient pulse trimming when the pulse is completely encompassed by the absorber section. In the shorter absorber devices a portion of the pulse is being broadened by the gain section for every instance in time.

The typical evolution of the pulse train shape is shown in Fig. 4-16a. The points labeled A to D correspond to biasing conditions at key points used in the construction of the operational maps introduced in Fig. 4-2. For convenience in Fig. 4-16b, the maps are shown again with annotations to mark the biasing points represented in Fig. 4-16a. Typically, the shortest pulses are produced at currents close to laser threshold, while increasing the injection current beyond laser threshold results in spectral broadening and pulse broadening due to self-phase modulation [13]. Point D represents a characteristic pulse train that may be found outside the contours of the operational maps. In this case pulse break-up is depicted [3], which often occurs at currents slightly higher than the boundaries of the map.
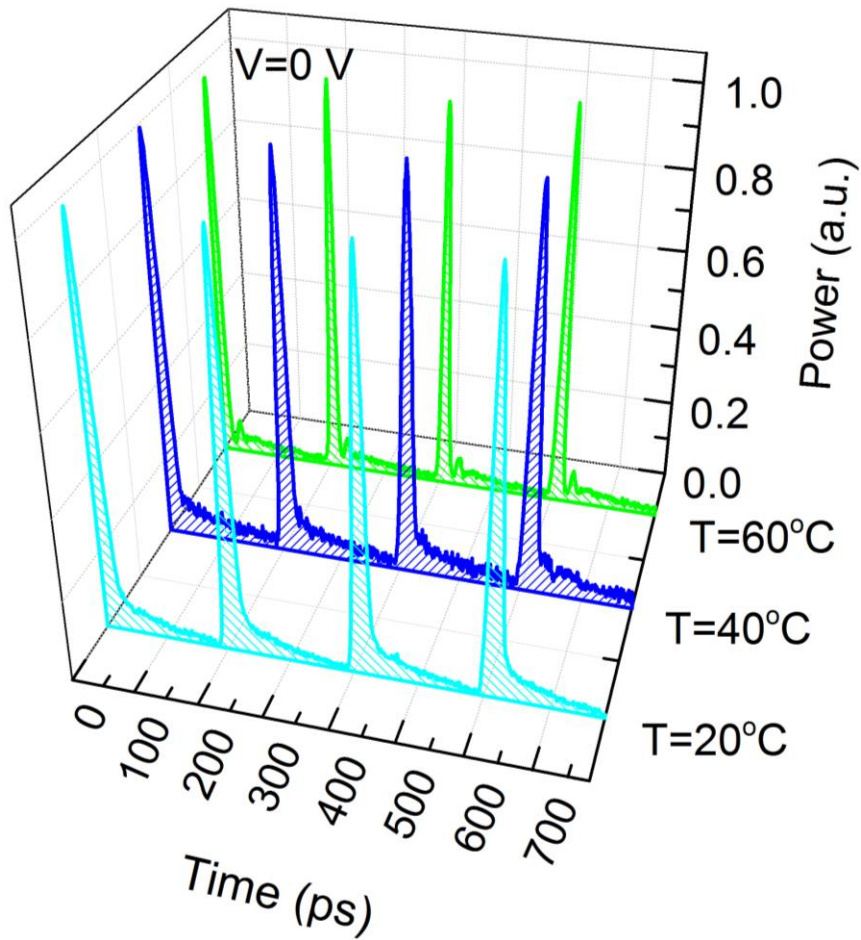
Figure 4-14. Normalized temporal measurements of the 5 GHz pulse train as captured on a 140 GHz digital scope.. The pulse widths (FWHM) corresponding to the pulse spectra shown in FIG. 4-7 were 17 ps, 16 ps and 9 ps, at temperatures of 20, 40 and 60 °C, respectively.
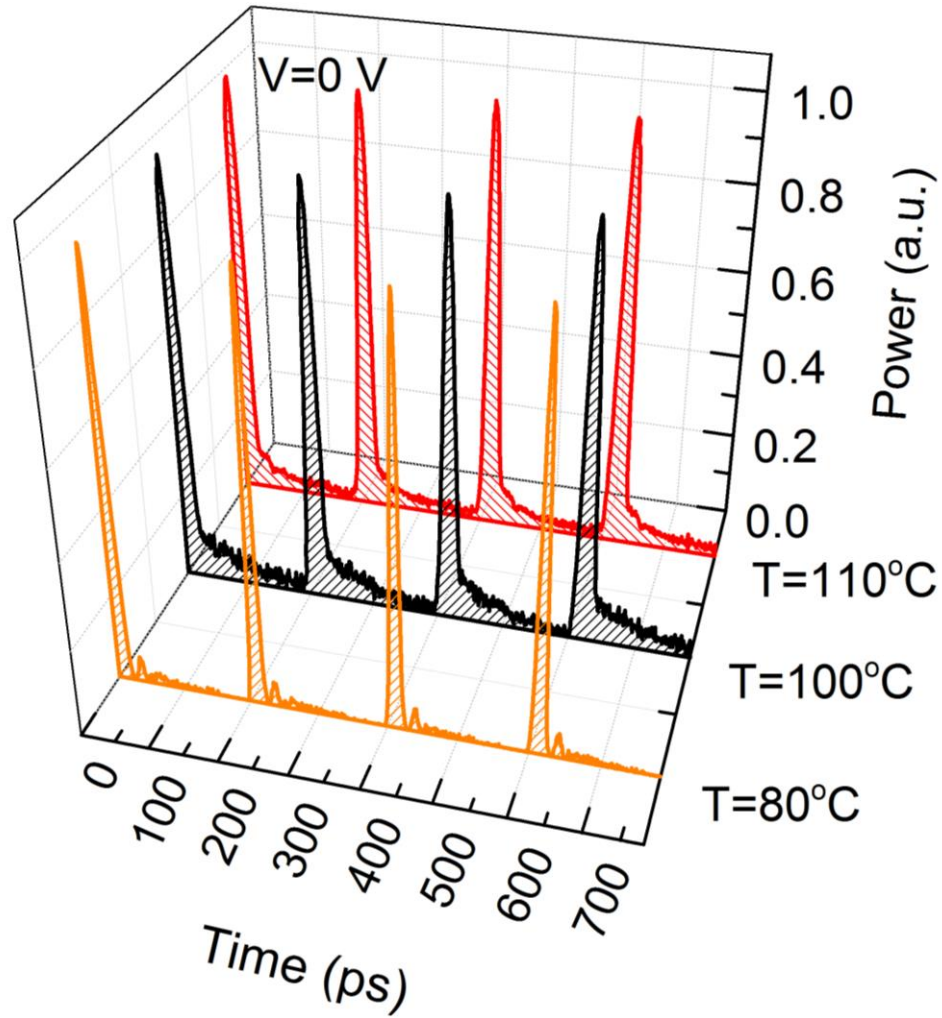
Figure 4-15. Normalized temporal measurements of the 5 GHz pulse train as captured on a 140 GHz digital scope. The pulse widths (FWHM) corresponding to the pulse spectra shown in FIG. 4-7 were 8, 17 and 19 ps at 80, 100 and 110 ºC, respectively.
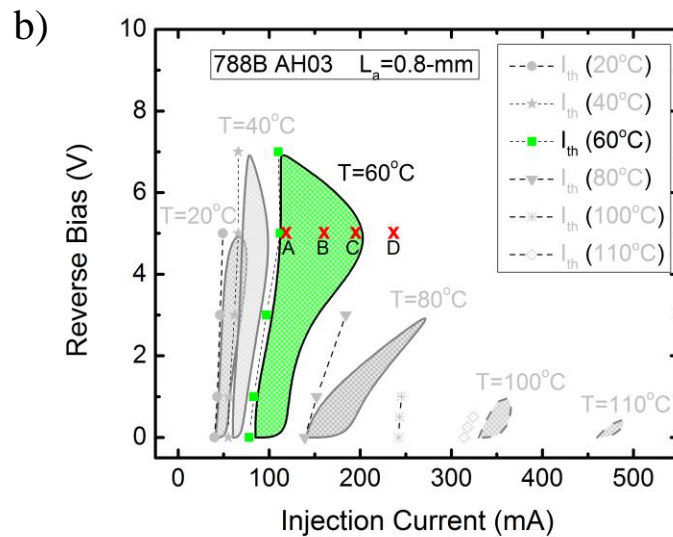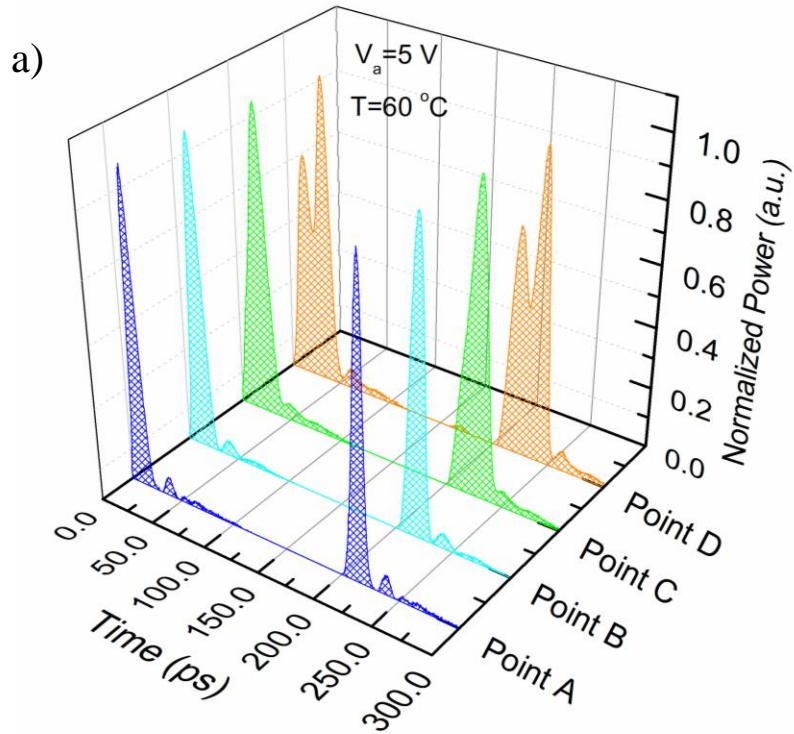
Figure 4-16. (a) Pulse train output at T=60 $^{\circ}$C and V_a= -5V for a device with L_a=0.8-mm. Points A to D correspond to biasing conditions at key points in the T=60 $^{\circ}$C operational map shown in Fig. 4-2. Shown again in (b) for convenience

b) Pulse Generation under GS/ES Hybrid Operation

As described in section 4-3, and shown in Figs 4-10 through 4-12, when operating at temperatures near the GS to ES transition point, competition between the lasing states often results in distortion of pulse shape and consequently the deterioration of mode-locking [16]. It is found that there exists an intermediate condition where both ground and excited states are lasing simultaneously. Under these circumstances, unstable operation is generally observed, characterized by switching between pure ES lasing and hybrid lasing, or similarly, switching between pure GS and hybrid state lasing. In some regimes away from either of these boundaries, pulse trains with multiple peaks exhibit regular repetition. Simultaneous two-state lasing in quantum dots has been previously noted [19]. One such case is shown in Fig. 4-17 for the device having a 1.2-mm absorber. At T=70 $^{\circ}$C, I=316 mA and V = 0 V applied to the absorber, hybrid lasing occurs and more complex pulse structure is observed. Fig. 4-17b shows the optical pulse as measured from the high-speed oscilloscope. It is believed that this pulse shape is the result of a superposition of two more narrow optical pulses, one of the ES and the other of the GS. This hypothesis could be validated in the future with a FROG measurement, which would determine the spectral content of the optical pulse. Another possibility could be to use a tunable filter to block contributions of the output for one of the lasing states and measure the resulting pulse train for stability.

To contrast the simultaneous lasing of excited and ground states shown in Figs. 4-17, the temporal pulse data for the conditions of pure GS and pure ES lasing are shown in Figs. 4-18 and 4-19. The biasing conditions selected were; (4-18a-b) T=60 $^{\circ}$C with V=0 V

and I=132 mA, (4-18c-d) T=60 °C with V=-2.5 V and I=347 mA, (4-19a-b) T=70 °C with V=0 V and I=224 mA and (4-19c-d) T=70 °C with V=-1 V and I=312 mA. The corresponding optical spectrum data are also shown. From Figs. 4-18 and 4-19, it is seen that the tail decays more gradually for the case of ES lasing ultimately leading to increased levels of intra-pulse energy. This is presumably a result of slower gain/absorber dynamics at the elevated values of current [18]. Although the narrowest pulses were found to occur for the case of pure GS lasing, the quality of the optical pulses as generated from the ES is still qualitatively good. ES pulses are achievable over a wide range of biasing conditions producing pulses with FWHM of less than 18.7 ps and excellent pulse power. Analysis of these conditions with an electrical spectrum analyzer also shows excellent RF extinction ratio.

Owing to the high quality of optical pulses produced from the ES in addition to those of the GS, the possibility of uncooled optical time division multiplexing in a QD MLL has been recently expressed [20]. This can dramatically reduce the energy-per-bit of the transceiver architecture, as traditionally the thermoelectric coolers account for a significant percentage of the total power budget. With a maximum pulse FWHM of 18.7 ps and a period of 200 ps, 10 OTDM channels could be realized resulting in a total aggregate bandwidth of 50 Gbps [21].

c) *Time-Bandwidth Product*

In this final subsection of chapter 4 the temperature-dependent time-bandwidth product (TBP), as measured from the high-speed sampling oscilloscope, is briefly

discussed. In chapter 5, the TBP data presented here is re-visited when a comparison is drawn between reduced values of unsaturated absorption at higher temperatures and low values of measured TBP. Using the 3-dB bandwidth from Fig. 4-7 and the pulse widths (FWHM) from Fig. 4-14, the evolution of the TBP has been calculated. In Fig. 4-20 the temperature dependent TBP is given for 0 V (red stars), 1 V (blue squares), 5 V (green triangles) and 7 V (navy diamonds) reverse bias applied to the saturable absorber. It is clearly seen that in all cases the TBP is improving with increasing temperature, such that there is minimum value between 60 and 80 ^{o}C of ~1.3. Above 98 ^{o}C, when the quantum dot mode-locked laser is operating from the ES, the resulting pulses presumably become more heavily chirped, and the TBP rises to 18 at 100 ^{o}C. This is not surprising since the gain-section current required to obtain mode-locked pulses is much higher than the threshold currents above 80 ^{o}C. The observed minimum in TBP at temperatures above room temperatures is consistent with the prior findings of this chapter wherein a great deal of evidence has been presented showing that device performance improves with high temperature operation in the short absorber device. In the next chapter we examine the physical mechanisms behind these observations.
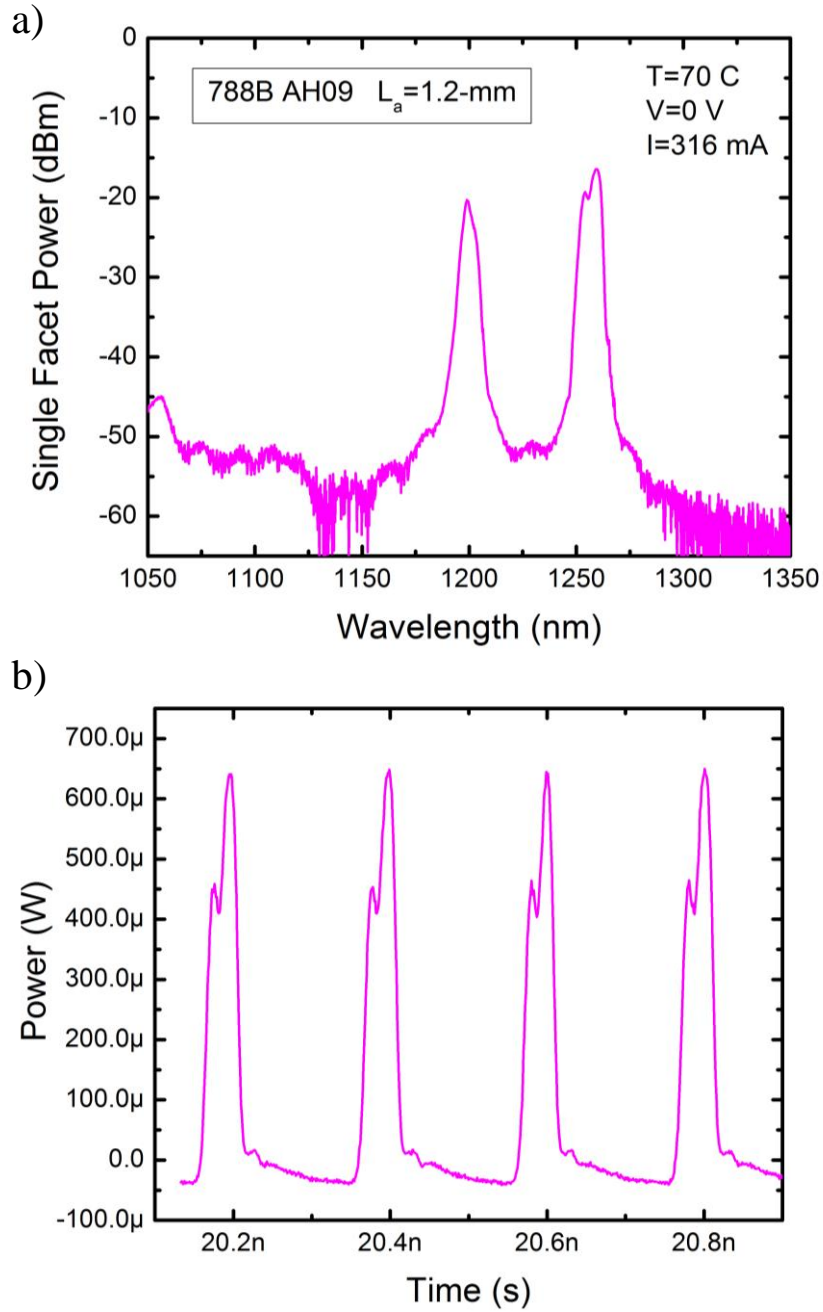
Figure 4-17. Measured optical spectra (a) of the two-section MLL having L_a=1.2-mm (788B AH09). Shown for the biasing conditions of T=70 °C with V=0 V and I=316 mA. The equivalent pulse train in the time domain under these condtions is shown in (b). Competition between the ES and GS pulsing has lead to pulse overlap.
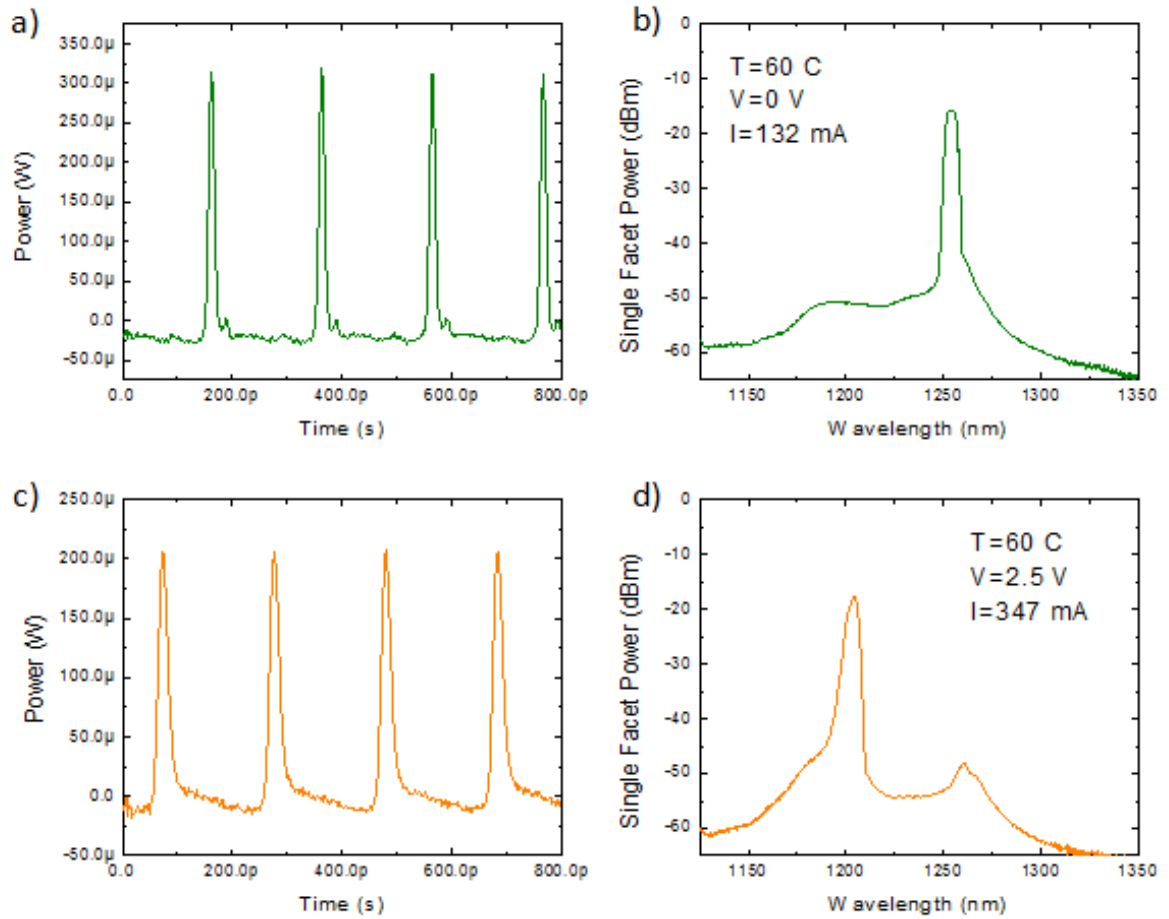
Figure 4-18. Measured optical spectra of the two-section MLL having L_a=1.2-mm. Shown

for the biasing conditions of; (a-b) T=60 °C with V=0 V and I=132 mA, (c-d) T=60 °C with

V=2.5 V and I=347 mA,
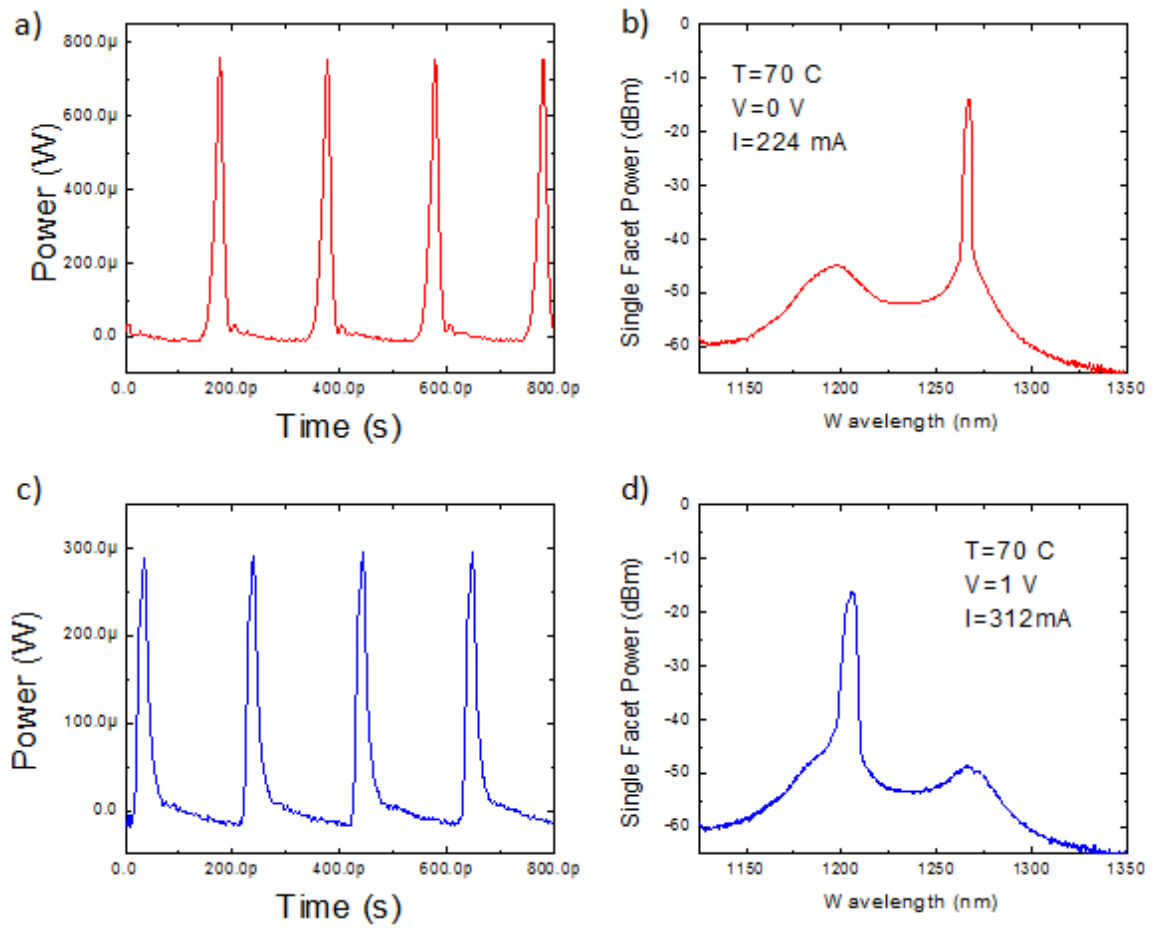
Figure 4-19. Measured optical spectra of the two-section MLL having L_a=1.2-mm (788A AV06). Shown for the biasing conditions of (a-b) T=70 $^{\circ}$C with V=0 V and I=224 mA, and (c-d) T=70 $^{\circ}$C with V=1 V and I=312 mA.
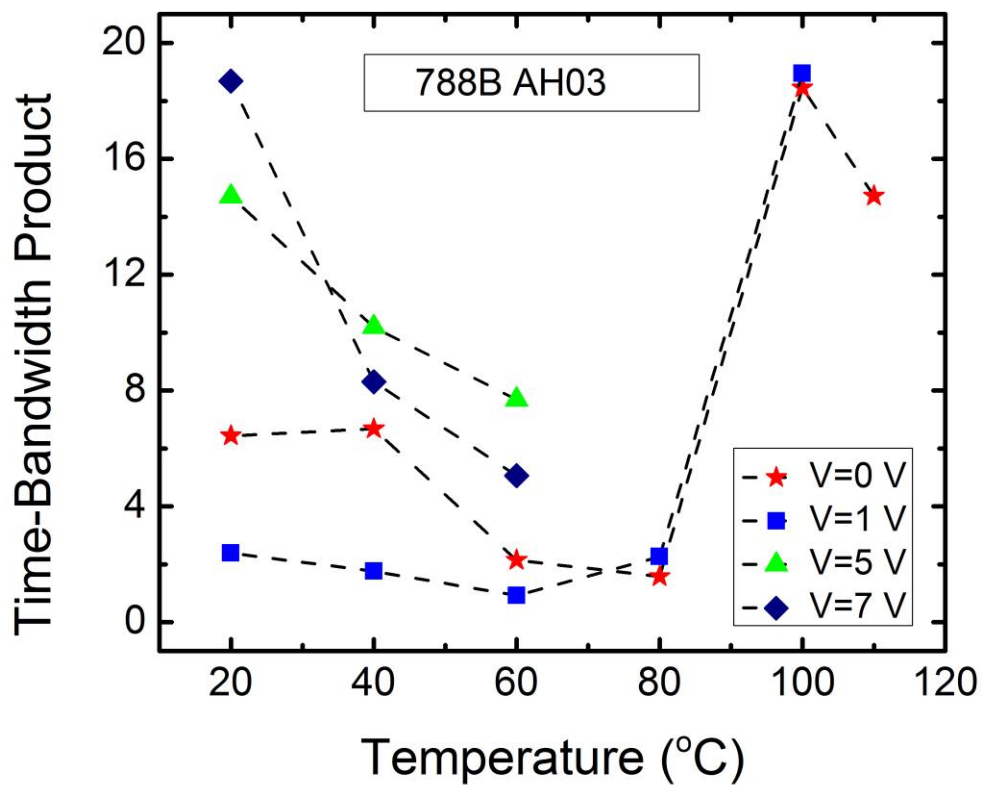
Figure 4-20. Time-bandwidth product (TBP) over temperature for the operating bias points of 0, -1, -5, and -7 V applied to the saturable absorber. TBP values are determined using the temporal and spectral data presented in Figs. 4-7 and 4-14. A minimum TBP is shown to occur between the temperatures of 60 and 80 ^{o}C.

REFERENCES FOR CHAPTER 4

[1] U. Keller, "Recent developments in compact ultrafast lasers," Nature, vol. 424, pp. 831-838 (2003).

[2] Yan Li, Luke F. Lester, Derek Chang, Carsten Langrock, M. M. Fejer, and Daniel J. Kane. "Characteristics and instabilities of mode-locked quantum dot lasers," Optics Express, vol. 21, no. 7, (2013)

[3] Xin, Y.-C., Kane, D.J., and Lester, L.F., "Frequency-resolved optical gating characterization of passively modelocked quantum-dot lasers," Electron. Lett. vol. 44, no. 21, pp. 1255-1257 (2008).

[4] R. Bracewell, The Fourier Transform and Its Applications (McGraw-Hill, New York, 1965)

[5] R. Raghunathan, M. Crowley, F. Grillot, Y. Li, J. K. Mee, V. Kovanis, L.F. Lester, "Pulse Characterization of Passively Mode-locked Quantum Dot Lasers Using a Delay Differential Equation Model Seeded with Measured Parameters." IEEE J. Selected Topics in Quan. Electron. No. 99, pp. 1 (2013)

[6] J. K. Mee, M. T. Crowley, N. Patel, D. Murrell, R. Raghunathan, A. Aboketaf, A. Elshaari, S. F. Preble, P. Ampadu, and L. F. Lester, "A passively mode-locked quantum-dot laser operating over a broad temperature range" Appl. Phys. Lett. vol.101, no.7, pp.071112-4 (2012)

[7] M. T. Crowley, N. Patel, D. Murrell, Y-C Xin, A. Stintz and L. F. Lester, J. High Speed Elec. & Sys. **20**, 713, (2011).

[8] M. A. Cataluna, E. U. Rafailov, A. D. McRobbie, W. Sibbett, D. A. Livshits and A. R. Kovsh, IEEE Photon. Tech. Lett. **18**, 1500, (2006).

[9] M. A. Cataluna, D. B. Malins, A. Gomez-Iglesias, W. Sibbett, A. Miller, and E. U. Rafailov, "Temperature dependence of electro-absorption dynamics in an InAs quantum-dot saturable absorber at 1.3 μm and its impact on mode-locked quantum-dot lasers" Appl. Phys. Lett. 97, 121110 (2010).

[10] Weidong Yang, Roger R. Lowe-Webb, Hao Lee, and Peter C. Sercel, "Effect of carrier emission and retrapping on luminescence time decays in InAs/GaAs quantum dots," Phys. Rev. B 56, 13314–13320 (1997)

[11] F. Grillot, N. A. Naderi, J. B. Wright, R. Raghunathan, M. T. Crowley, and L. F. Lester, "A dual-mode quantum dot laser operating in the excited state", Appl. Phys. Lett, 99, 231110, 2011.

[12] K. Solehmainen, T. Aalto, J. Dekker, M. Kapulainen, M. Harjanne, K. Kukli, P. Heimala, K. Kolari, and M. Leskela, IEEE J. Lightwave Tech. **23**, 3875, (2005).

[13] GP Agrawal, and NA Olsson,"Self-phase modulation and spectral broadening of optical pulses in semiconductor laser amplifiers," IEEE J. Quan.Elect.vol. 25.no. 11 (1989)

[14] JK Mee, MT Crowley, R Raghunathan, D Murrell, LF Lester, " Characteristics of passively mode-locked quantum dot lasers from 20 to 120°C ", Proc. SPIE 8619, Physics and Simulation of Optoelectronic Devices XXI, 86190B (2013)

[15] Cataluna, M.A., Sibbett, W., Livshits, D.A., Weimert, J., Kovsh, A.R., Rafailov, E.U., "Stable mode locking via ground or excited state transitions in a two-section quantum-dot laser," App. Phys. Lett. vol. 89, pp. 081124-1 – 081124-3 (2006).

[16] M. T. Crowley, D. Murrell, N. Patel, M. Breivik, C.-Y. Lin, Y. Li, B.-O. Fimland, and L. F. Lester, "Analytical modeling of the temperature performance of monolithic passively mode-locked QD lasers" IEEE J. Quantum Electron. 18, 1059 (2011)

[17] C. Y. Lin, F. Grillot, N.A. Naderi, Y. Li, J.H. Kim, C.G. Christodoulou, L.F. Lester, "RF linewidth of a monolithic quantum dot mode-locked laser under resonant feedback." IET Optoelectronics, vol. 5, no. 3, pp 105-109 (2011)

[18] R. Raghunathan, J. K. Mee, M. Crowley, F. Grillot, V. Kovanis, L.F. Lester, "Modeling and Characterization of Pulse Shape and Pulse Train Dynamics in Two-Section Passively Mode-Locked Quantum Dot Lasers," SPIE OPTO 86190C-86190C-11 (2013)

[19] A. Markus, JX. Chen, C. Paranthoen, A. Fiore C. Platx, O, Gauthier-Lafaye, "Simultaneous two-state lasing in quantum dot lasers," Appl. Phys. Lett. vol. 82, no.12, pp. 1212-1220 (2003)

[20] J. K. Mee, M. T. Crowley, D. Murrell, R. Raghunathan, L. F. Lester, "Temperature Performance of Monolithic Passively Mode-Locked Quantum Dot Lasers: Experiments and Analytical Modeling," Selected Topics in Quantum Electronics, IEEE Journal of , vol.19, no.4, pp.1101110 (2013)

[21] A. A. Aboketaf, L. Cao, D. Adams, A. W. Elshaari, S. F. Preble, M. T. Crowley, L. F. Lester and P. Ampadu, "Hybrid OTDM and WDM for multicore optical communication," IGCC, pp.1-5, (2012)

Chapter 5 – The Evolution of Device Performance with Increasing Temperature and Bias Conditions

In chapters 3 an anlytical model was presented which predicted that the path toward high temperature operation in a quantum dot mode-locked laser was to move to a shorter absorber length. It was subsequently demonstrated in chapter 4 that the 0.8-mm and 1.0-mm abosrber devices indeed exhibited the best temperature performance. It was discovered that these devices perfomed better at higher operating temperatures, evident by the expanded operational range in the contour maps (Fig. 4-2) and minimum pulse TBP (Fig. 4-20) between 60 and 80 °C. In section 5.1 the influence of temperature dependent unsaturated absorption on the optical pulse width is put forth as the clear physical mechanism that drives improved performance at elevated temperatures. In section 5.2 the stability of the mode-locked lasers is examined with more scrutiny using frequency resolved optical gating (FROG) measurements. The evolution of the pulse TBP with temperature is revisited and compared to that of chapter 4. In section 5.3, for the first time non-linear two-pulse-per-round-trip generation is shown to be a stable effect as verified by FROG. This has exciting implications for applications requiring a high repetition rate source. Finally, in section 5.4 the waveguide geometry and its relative impact on the effective current density and ultimately the range of pulsed operation is discussed.

5.1 Temperature Dependent Tuning of Modal Gain and Absorption

One of the key observations from chapters 3 and 4 is that the devices which are optimized for broad temperature operation (L_a/L_g=0.11&0.14) prefer lasing temperature

around 60 ℃. This is evidenced not only by expanded regions of mode-locked operation, but also from measurements of the pulse characteristics wherein narrow pulse durations and minimum inter-pulse energy occurred for the temperatures between 60 and 80 ℃. The analytical model from chapter 3 has demonstrated great utility; however, it fails to capture the dynamics related to improved stability over an increased range of injection currents. Eqn. (3-4) is derived in the limit that the pulse train is sinusoidal [1,2], while Eqn. (3-6) describes the threshold condition for lasing. In addition, the model assumes a uniformly distributed gain and loss everywhere in the cavity, i.e., the variation of the gain and loss characteristics along the length of the device is not accounted for [3]. The effect of lumped gain/loss elements is magnified at currents above threshold and manifests in self-phase modulation and gain saturation [4]. Due to these constraints, the model is best suited to conditions near threshold. Previous studies have shown that mode-locking stability can improve at elevated temperatures due to an increased rate of thermionic emission [5,6]. In this study, it is shown that there are potentially other factors leading to improved stability with temperature. In particular, a trend in the unsaturated absorption has been found that explains the expanded range of pulsed operation beyond the onset of mode-locking.

Using the method described in section 3.1, In Fig. 5-1 the unsaturated absorption (a_o) at the gain peak is derived from modal gain and loss measurements and plotted over the full range of temperatures studied. In section 3.1 it was noted that the average differential wavelength shift in the gain spectra (0.64 nm/℃) was larger than that in the absorption spectra (0.44 nm/℃) resulting in a gain peak walk off that reduces the absorption at the lasing wavelength for elevated temperatures. As seen in Fig. 5-1 the

minimum unsaturated absorption values are measured at 60 $^{\circ}$C for all absorber biasing conditions. A similar trend can be found in the variation of the TBP with temperature, first reported in Fig. 4-20 and shown again in the inset of Fig. 5-1, wherein the TBP is observed to minimize between 60-80 °C. It is found that a reduced value of a_o allows for lower modal gain, g_o, in the amplifying section of the device as per Eqn. (3-6). As a result, the pulse is subjected to less distortion per pass in the gain section, and pulse shaping takes place more gradually. Thus, the pulse widths at 60 °C are generally shorter than those at any other temperature; accordingly, the operational conditions yielding pulses below 18.7 ps expand as observed in Fig. 4-2 and 4-3. The remarkable similarity between the behavior of the unsaturated absorption and the TBP provide strong experimental evidence that the tuning of the modal gain peak off of the absorption peak is indeed responsible for improved operation at elevated temperature. This previously unreported correlation between low unsaturated absorption and reduced TBP provides valuable insight into the physical mechanisms that drive mode-locking quality. With this understanding, future devices can be designed to leverage broad gain bandwidths and selective lasing wavelength capabilities to operate in a regime that minimizes the unsaturated absorption and thus maximizes the range of biasing conditions over which the device produces high quality pulses.
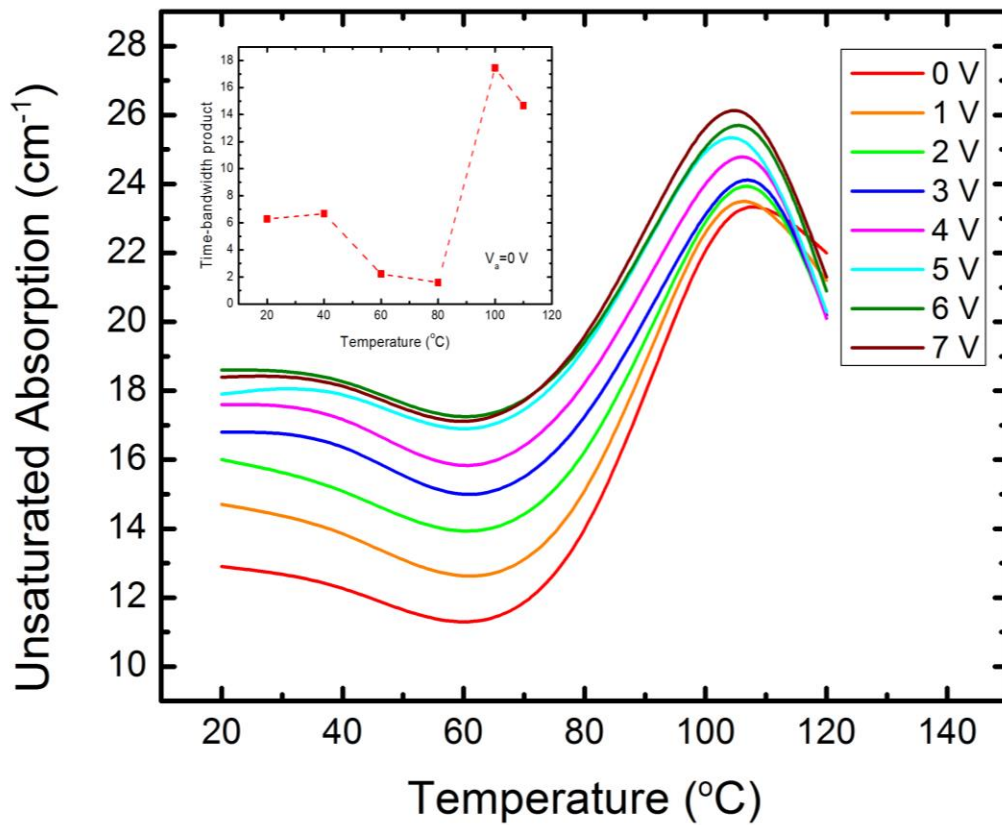
Figure 5-1. Experimentally measured unsaturated absorption at the gain peak over the temperature range from 20 to 120 °C for saturable absorber reverse bias of 0 to -7 V. The absoption is found to reach a minimum around T=60 °C. This is a consequnce of the gain peak/abosrption peak walk off. Inset: Time-bandwidth product over temperature for 0 V reverse bias at the saturable absorber.

5.2 <u>Experimental Study of Operational *Stability*</u>

The characterization techniques described in chapter 4 for resolving the temporal behavior of the mode-locked laser have proven adequate for the construction of the contour maps of Figs. 4-2 through 4-6, which described the operational range of the devices. In general, with the high speed sampling oscilloscope we can gather information regarding the pulse width and asymmetry to a high level of accuracy. This is especially true for pulses with FWHM greater than 10 ps. However, it has been shown that simultaneous characterization of time and frequency is necessary for true determination of mode-locked stability [7]. In this section we examine the temperature characteristics of the laser with a state-of-the-art Frequency Resolved Optical Gating (FROG) pulse measurement system.

a) Description of FROG Measurement

Light from the quantum dot mode-locked laser is coupled into polarization maintaining (PM) fiber using the optical head described in chapter 4. At the optical input of the FROG, the light is collimated and launched into a free space Michelson interferometer. A variable delay, set by the user interface software, produces a collinear beam of pulse pairs which are then coupled into a 45.4 mm a-periodically-polled $LiNO_3$ (A-PPLN) waveguide. The delay is scanned such that power of the second harmonic generation (SHG) is 4X greater when the pulses are overlapping compared to the case of no overlap as the efficiency of SHG is proportional to $|E^2|$ [8,9]. The frequency doubled light is then focused into a multi-mode fiber with a microscope objective, and routed into a spectrometer. This allows for determination of pulse asymmetry and chirp. A more detailed description of this setup can be found in [7]

b) Pulse Characteristics over Temperature

Using the method described above, FROG measurements have been captured for the device having L_a=1.0-mm (788B AH05) at temperatures of 20, 40, and 50 ^{o}C for the absorber reverse bias of 0V, 1V, 3V and 5V. Beyond 50 ^{o}C the optical spectrum has red-shifted outside of the usable range for the A-PPLN waveguides currently available. The device is shown to maintain stable mode-locking across the full range of examined conditions. These measurements serve as the first true verification of operational stability over temperature in this device as it is the first time that simultaneous time and frequency measurements have been captured. In Fig. 5-2a the retrieved temporal intensity and phase is shown at the temperature of 20 ^{o}C for the operating point of 3 V reverse bias applied to the saturable absorber and 62 mA of forward injection current. The corresponding temporal phase and chirp is also shown in Fig. 5-2b. It is found that the 20 ^{o}C case produced a pulse width FWHM of 8.6 ps. The pulse's asymmetric profile is clearly seen, which in the case of Fig. 5-2 is shown to have a slow leading edge followed by a fast trailing edge. The temporal phase is found to be parabolic with a concave-up profile. In contrast, it has been discovered that when the pulse's temporal intensity exhibits a fast leading edge followed by a slow trailing edge, the temporal phase will be parabolic with a concave-down profile. An example of this is found in Fig. 5-3 where the pulse temporal intensity, phase and chirp are shown for the temperature of 40 ^{o}C. Fig. 5-3a and 5-3b are the retrieved FROG traces for an injection current of 82 mA and a reverse absorber bias of 3 V. Fig. 5-3c and 5-3d are the retrieved FROG traces for an injection current of 95 mA and a reverse bias of 7 V. Fig. 5-3c and 5-3d are shown for the purpose of contrasting the different pulse shapes.

116

It should be noted that FROG SHG has time direction ambiguity, thus it is not certain if the flipping of the asymmetry is an artifact of the pulse measurement or a real effect. Never-the-less, reversal of the asymmetry in the temporal profile has been studied in depth with a numerical (DDE) model that enabled determination of the optical field, optical gain, and optical absorption profiles with time from a mode-locked laser [10]. Therein, the variances in the pulse shape were attributed to change absorber recovery time for different linewidth enhancement factors (α-parameters). For the case when the leading edge of the pulse is steeper than the trailing edge, the temporal phase is concave down. It has been shown found that slower absorber saturation and faster recovery is correlated to a larger α-parameter [10]. Accordingly, as the pulse, which has been broadened by the gain section, enters the saturable absorber, it takes longer for the total loss to drop below the total gain. This creates the slow leading edge. However, because the absorber recovery time is fast, the pulse is efficiently trimmed on the trailing edge. This leads to a pulse shape similar to the shape of the pulses seen in Figs. 5-3a and 5-3b. On the other hand, for the case of a lower α-parameter, the absorber saturates rapidly but the absorber recovery time is slower [10]. In this case, the DDE model predicted that when the pulse enters the absorber it is sharply trimmed on the leading edge, however, the trailing edge is more gradual due to the slower absorber recover time. This gives way to a pulse shape similar to that of Fig. 5-3c.

a)

b)
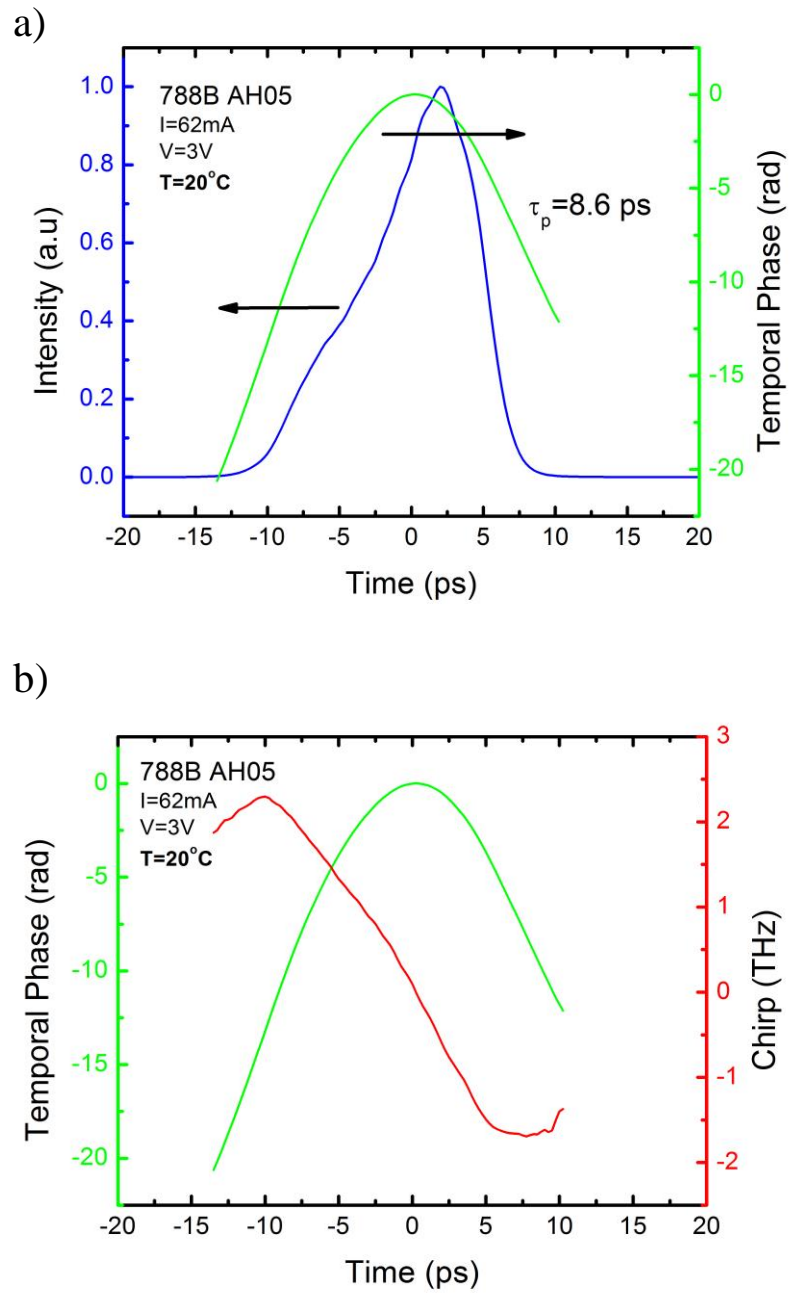
Figure 5-2. Retrieved pulse characteristics from FROG at T= 20 ºC for forward injection current of 62 mA and reverse bias of 3 V. (a) Retrieved pulse intensity and temporal phase. (b) Temporal phase profile and chirp.
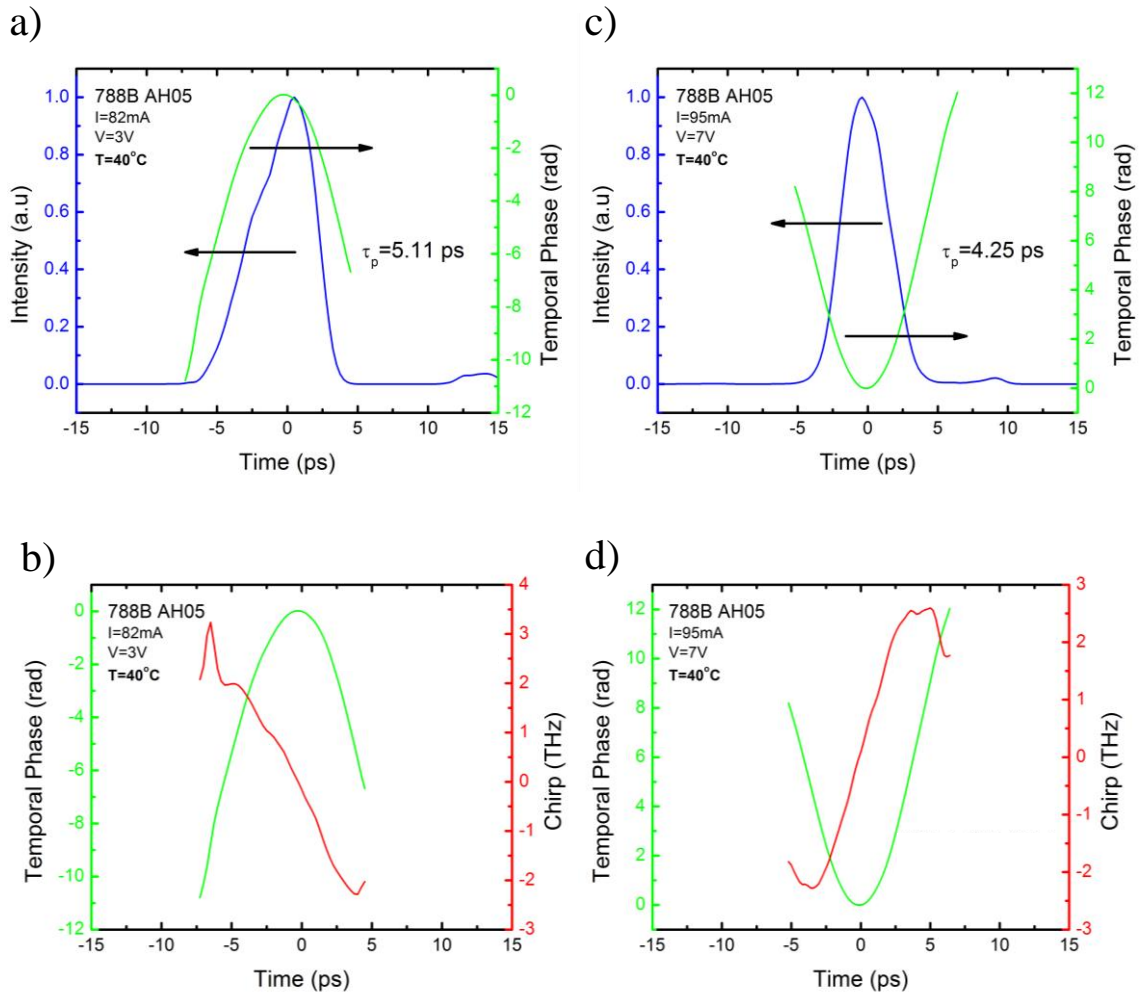
Figure 5-3. Retrieved pulse characteristics from FROG at T= 40 ℃ for forward injection current of 82 mA and reverse bias of 3 V. (a) Retrieved pulse intensity and temporal phase. (b) Temporal phase profile and chirp. (c) Temporal intensity and phase at T= 40 ℃ for forward injection current of 95 mA and reverse bias of 7 V. (d) Temporal phase profile and chirp

a)

b)
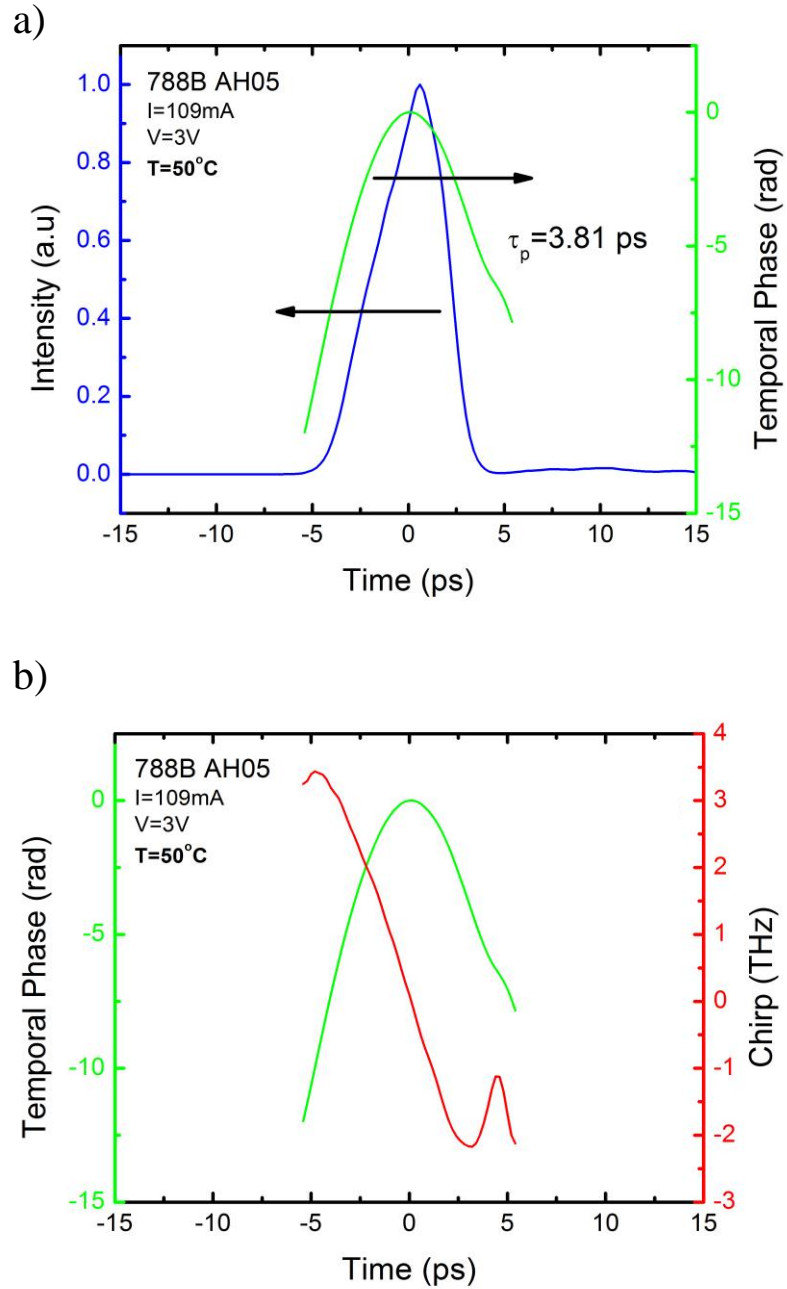
Figure 5-4. Retrieved pulse characteristics from FROG at T= 50 ºC for forward injection current of 109 mA and reverse bias of 3 V. (a) Retrieved pulse intensity and temporal phase. (b) Temporal phase profile and chirp.

In Fig. 5-4 the retrieved FROG characteristics are shown for the L_a=1.0-mm device

at T=50 °C for the biasing conditions of 3 V reverse bias on the saturable absorber and 109

mA injection current across the gain region. This was the highest temperature examined

with the FROG. It is found that in comparison to Figs. 5-2 and 5-3, this case produced a

narrower pulse FWHM being 3.8 ps as shown in Fig. 5-4. Overall, the narrowest pulse was

measured at T=50 °C with 5 V reverse bias and I = 119 mA. Those conditions produced a

pulse FWHM of 3.5 ps with 1.59% FROG error. The FROG error in all of the cases

examined here was less than 2%. Upon examination of the temporal and spectral phase

characteristics of the device as recovered by FROG, two primary observations are noted.

Firstly, the magnitude of the differential temporal phase with time is minimized at the lower

temperature values, seemingly in contrast with the recovered pulse widths, which minimize

at higher temperature. It is concluded that additional factors must be influencing the

temporal pulse width. Accordingly a second observation is made and comes with

examination of the spectral phase versus angular frequency. Pulse shaping in a laser is the

result of the interplay between group delay dispersion (*GDD*) and self-phase modulation

of the gain medium [11,12]. The group delay dispersion is the derivative of the group delay

with respect to angular frequency and can be expressed as:

$$GDD = \frac{dT_d}{d\omega} = \frac{d^2\phi}{d\omega^2}$$

5-1

where ω is the angular frequency, ϕ is the spectral phase and T_d is the group delay which

is equal to the first derivative of the spectral phase with respect to angular frequency [11].

Calculations of the *GDD* yield approximately constant values due to the quadratic nature of the spectral phase. These results have been summarized in the short table below for the applied reverse bias of 3V and the bias currents of I = 62, 82, and 109 mA at the temperatures of 20, 40 and 50 $^{\circ}$C, respectively.

Table 6: Group Delay Dispersion with increasing temperature

Temperature (ºC)	Group Delay Dispersion (ps²) V=3 V	Group Delay Dispersion (*Linear Chirp*) (ps/nm) V=3 V
20	45.8	-16.1
40	19.5	-6.9
50	15.3	-3.5

From Table 6 it is found that the group delay dispersion reduces at the higher temperatures and achieves a minimum of 15.3 ps^2 at 50 $^{\circ}$C. This is in good agreement with the reduced optical pulse widths observed at higher temperatures. A similar correlation has been previously noted by Schmeckebier *et. al.* [13]. In that study, it was shown that the pulse FWHM and TBP followed the same trend as the slope of the linear spectral chirp, which is expressed in units of ps/nm. This is another form of the *GDD*, similar to the approach of [11], wherein the *GDD* is given as the wavelength derivative of the group delay, T_d, which yields *GDD* in time per unit length. Recall that T_d is the derivative of the spectral phase with respect to angular frequency. For direct comparison, in Table 6 the *GDD* (slope of the linear chirp) is given in units of ps/nm and is shown to reduce at increasing temperature. The values of *GDD* in units of ps/nm are plotted against the pulse FWHM in Fig. 5-5, and the same trend is observed over the range of examined temperatures.

Furthermore, examining the conditions of Fig. 5-3b and 5-3d, where at T=40 ºC a stronger reverse bias of 7V was applied to the absorber and shown to flip the asymmetry of the temporal pulse shape, it is seen that the absolute value of the *GDD* reduces from 19.5 ps^2 to 14.8 ps^2. This is reasonable given that the flip in asymmetry was an indication of reduced linewidth enhancement factor. It is however noted that the flip in the asymmetry of the spectral phase also creates a sign change in the second derivative of the spectral phase which is the *GDD*. A negative *GDD*, when expressed in units of s^2, corresponds to anomalous dispersion in contrast to a positive *GDD* which corresponds to normal dispersion [12]. Further experimentation is required to determine if a single device can truly exhibit both of these characteristics, or if this is some sort of artifact of the pulse measurement resulting from the time ambiguity.

The evolution of the pulse time-bandwidth product (TBP) has also been determined using the FROG for precise measurement of the optical pulse width and the optical spectrum analyzer for measurement of the 3-dB bandwidth of the optical spectrum. From this, a comparison is drawn to the TBP previously shown in chapter 4. The pulse width (FWHM), 3-dB bandwidth and calculated TBP are presented in Table 7 at the temperatures of 20, 40 and 50 ºC. The corresponding TBP values are plotted in Fig. 5.6 for reverse bias of 0 V (blue dashed line), 1 V (green dashed line), 3 V (orange dashed line) and 5 V (red dashed line). It is found that the TBP reduces at higher temperatures to as low as 1.43 at 50 ºC, being as high as 5.57 at 20 ºC. It was previously demonstrated in Fig. 4-20 that the TBP reached a minimum around T=60 ºC. Although there is not enough temperature range in this experiment to demonstrate a minimum around T=60 ºC, the general trend of

improving TBP at elevated temperatures is confirmed. It is also noted that the reduced levels of TBP shown in Table 7 and Fig. 5-6 coincide with reduced levels of *GDD* discussed above.
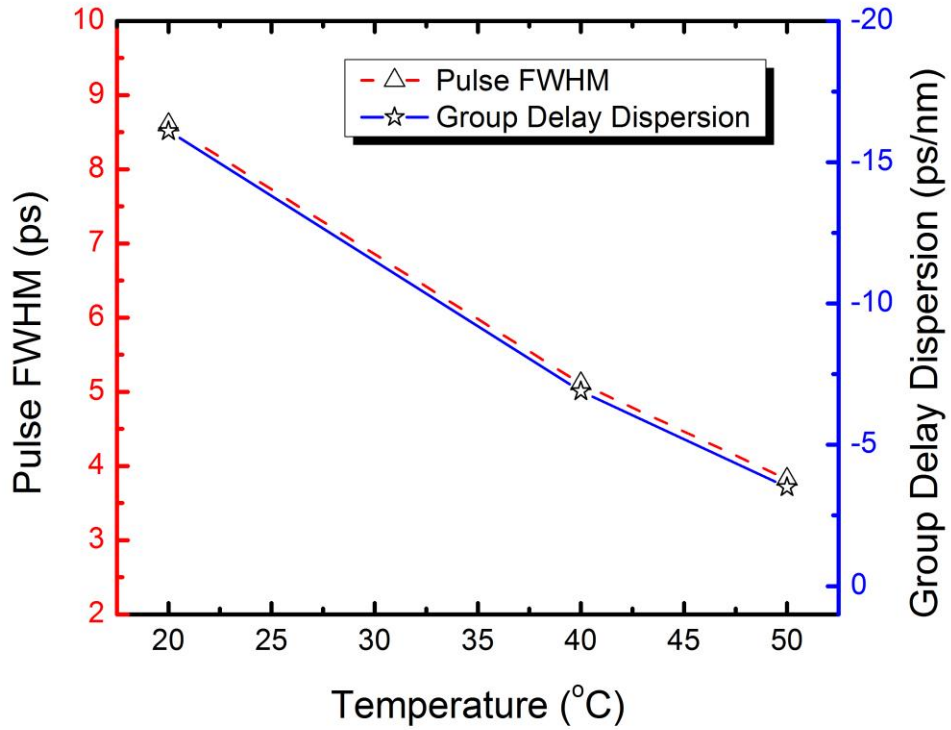
Figure 5-5. Optical pulse Full Width Half Maximum (FWHM) recovered from FROG pulse measurements (red dashed line), and Group Delay Dispersion (*GDD*) plotted in units of ps/nm at 20, 40 and 50 °C.

Table 7: Optical Pulse Width (FWHM). 3-dB bandwidth of the optical spectrum and the

calculated time-bandwidth product

Temp	Reverse Bias (V)	Pulse Width FWHM (ps)	Optical Spectrum 3-dB bandwidth		Time-Bandwidth Product
			(nm)	(GHz)	
20 ºC	0	17	1.6	317.2	5.39
	1	15	1.9	371.6	5.57
	3	8.6	2.5	494.9	4.26
	5	5.0	3.3	653.0	3.27
40 ºC	0	7.0	1.4	275.2	1.93
	1	5.7	1.7	334.0	1.90
	3	5.1	2.4	472.5	2.41
	5	3.9	2.7	531.6	2.07
50 ºC	0	6.8	1.1	210.4	1.43
	1	6.1	1.5	293.0	1.78
	3	3.8	3.1	607.6	2.31
	5	3.5	3.1	606.3	2.13
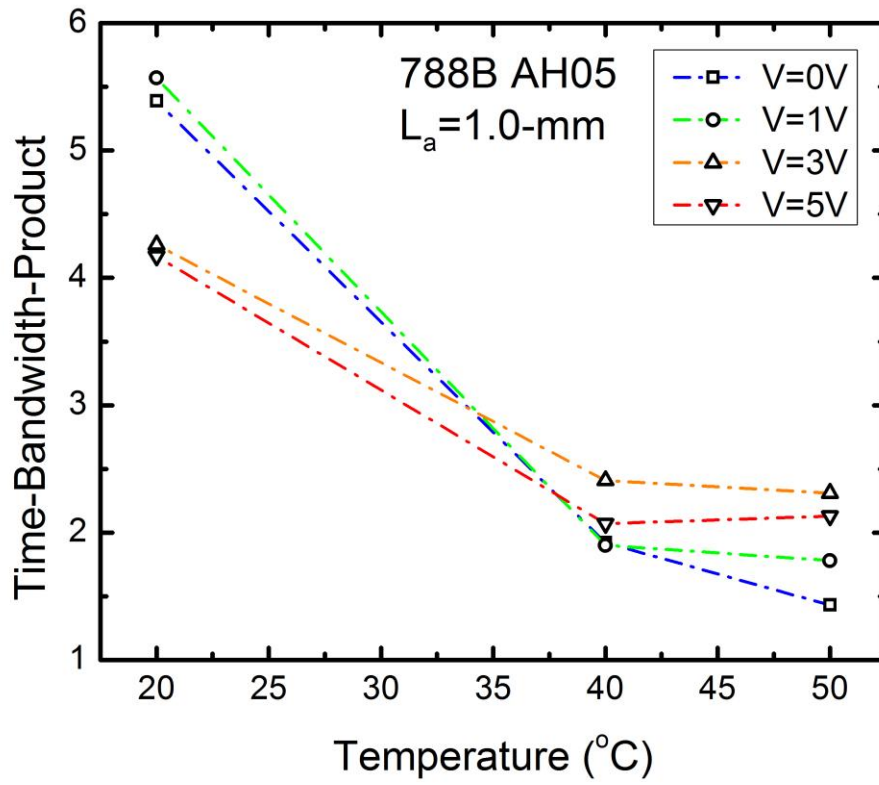
Figure 5-6. Evolution of time-bandwidth-product over temperature calculated from FROG measurements of the optical pulse train at T= 20, 40 and 50 °C. Shown for reverse bias voltages of 0 V (blue dashed line), 1 V (green dashed line), 3 V (orange dashed line) and 5 V (red dashed line)

5.3 <u>Stable Double Pulsing</u>

As discussed in chapter 1, the aggregate bandwidth from a quantum dot mode-locked laser can be dramatically increased by combining the laser with Si photonics to realize time and wavelength division multiplexing schemes [14,15]. In addition to the amount of parallelization within the architecture, bandwidth can be directly increased by adjusting the repetition rate of the optical pulse train. In this dissertation, the proficiency to achieve a wide range of stable (FROG confirmed) operation at the fundamental repetition rate of 5 GHz has been demonstrated. In this section, for the first time double pulsing as previously predicted by DDE modeling [16] is shown to be a stable effect as confirmed by FROG pulse measurements. In a previous study, using a double interval technique, the ability to stimulate specific higher order repetition rates compared to the fundamental was demonstrated in a multi-section device [17]. Here, a range of FROG confirmed stable harmonic mode-locking is demonstrated in a two-section laser. This discovery has strong engineering implications given that 2X increase in total capacity can be achieved by simply biasing the device in an appropriate manner.

It is found that for the device having an absorber length of 1.0-mm (ZLG788B AH05), when operating at the temperature of T=20 $^{\mathrm{o}}$ C, a region of double pulsing (two pulses per roundtrip) occurs at the reverse voltage of 5 V, between the injection currents of 108 and 118 mA. The evolution of the pulse shape is captured for visualization purposes with the high speed sampling oscilloscope and shown in Fig. 5-7. The onset of fundamental mode-locking occurs for the current of 70 mA (red curve). Increasing the current beyond the onset of mode-locking broadens the pulse until around 94 mA (green curve). Between

127

95 and 107 mA the pulse train becomes highly unstable. Very abruptly, at 108 mA narrow pulse generation occurs at double the fundamental repetition rate. Double pulsing is continuous across the range of 108 to 118 mA. Between 119 and 127 mA the pulse again becomes unstable. An example of a typical pulse shape within this region is shown in Fig. 5-7 at I=119 mA (maroon curve). Pulsing at the fundamental repetition rate resumes upon increasing the current further; however, these pulses are very wide as seen in Fig 5-7 at I=130 mA (light blue curve). The electrical spectrum characteristics of the pulse train are shown in Fig. 5-8a for a 45 GHz span. A narrow 6 MHz RF span has also been captured around the 10 GHz peak in Fig. 5-8b. From this, a Lorentzian fit has deduced an RF linewidth of 527 kHz. This is significantly higher than the line width under resonate feedback, which has been measured as low as 170 Hz [18]. It is clearly seen from Fig. 5-8a that the power in the 2nd harmonic is far greater than that of the fundamental 5 GHz frequency. The SNR of the 10 GHz peak is 43.8-dB and it is noted that the harmonics at 20 and 30 GHz exhibit greater SNR than those at 5, 15, and 25 GHz. The 5 GHz peak has a SNR of less than 10-dB. The double pulsing operation described here should not be confused with the harmonic mode-locking induced by the colliding pulse mode-locking effect [19]. In the latter, the absorber is positioned in the center of the cavity to induce the 2nd harmonic [17], whereas in the case that has been just been described, increased gain current is the method utilized. Therefore, one technique is geometrical, the other electrical.
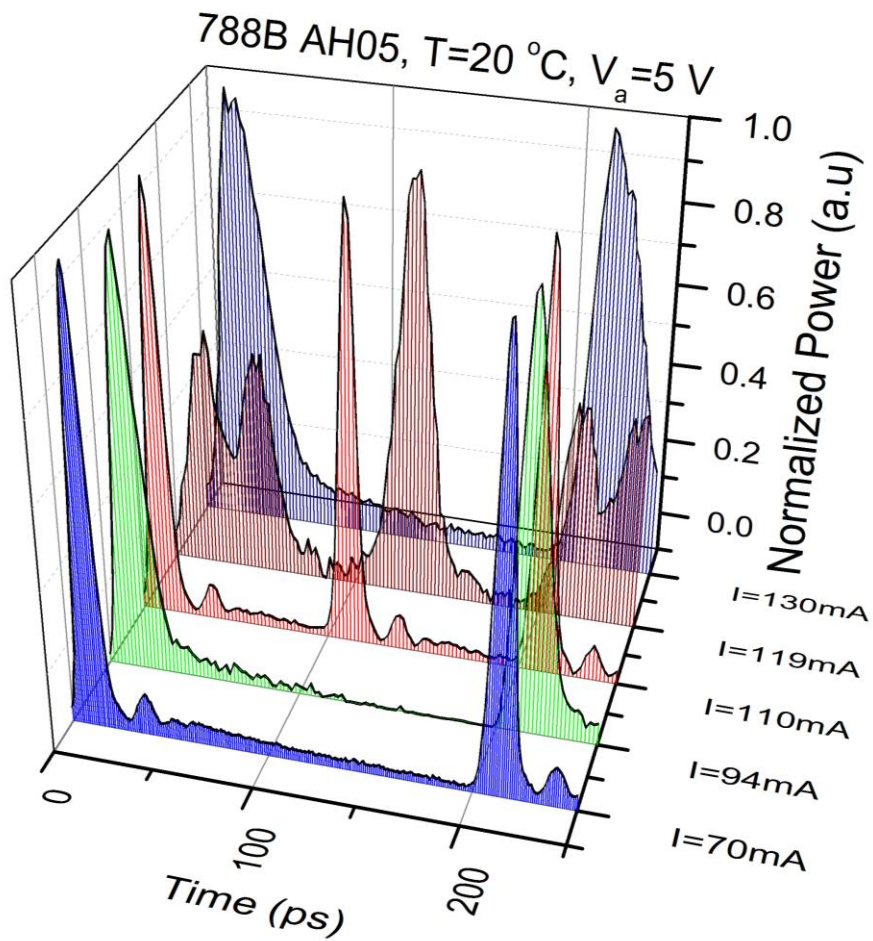
Figure 5-7. Evolution of pulse shape measured with the high speed sampling oscilloscope. The QD MLL has an absorber length of 1.0-mm and is shown biased from 70 to 130 mA with a reverse bias of 5 V at T=20 ºC. The pulse is shown to transition from fundamental mode-locking to harmonic mode-locking between 94 and 119 mA
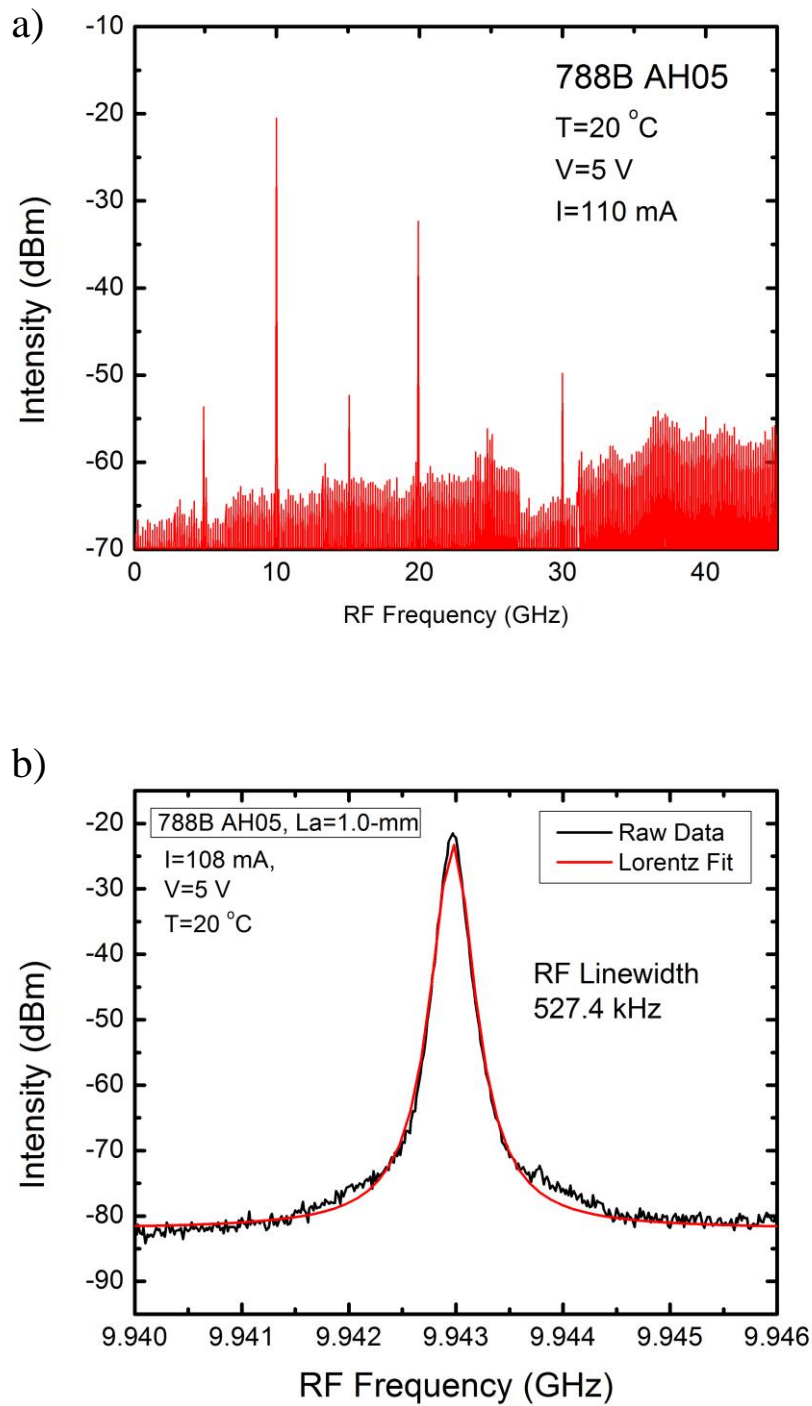
Figure 5-8. Electrical spectrum of QD MLL at T=20 °C with reverse bias of 5 V and injection current of 110 mA. (a) 45 GHz span showing high power in 2nd harmonic peak, and (b) 6 MHz span showing raw data (black line) and Lorentz fit (red line).

The observations in Figs 5-7 and 5-8 indicate that the device is *pulsing* at twice the fundamental repetition rate, but they do not serve as sound evidence that the double pulsing is in fact a *stable* effect. Simultaneous time and frequency characteristics, which are the necessary and sufficient criteria for determining mode-locked stability [7], have not previously been captured for double pulsing induced by gain non-linearities. To this point, FROG measurements are captured at the temperature of 20 °C, with a reverse bias of 5 V, over the injection current range of 70 to 130 mA. The retrieved temporal intensity, temporal phase and chirp are shown in Fig. 5-9. The forward injection currents are represented as follows: (a, b) I=70 mA, (c, d) I=94 mA, (e, f) I=108 mA, (g, h) I=110 mA and (i, j) I=130 mA.

This is the evolution of the optical pulse train with increasing current as measured by FROG: It is found that the pulses generated at the onset of mode-locking converge easily, producing a narrow 4.96 ps pulse with low chirp. This case is shown in Fig. 5-9 (a, b). (The FROG is considered to converge when the error is less than 2%). As the injection current is increased it is not possible to capture a FROG trace with low error, and beyond approximately I = 85 mA, no FROG traces will converge despite the fact that the high speed sampling oscilloscope displays a less than 20 ps pulse (Fig 5-7). An example of this region is shown in Fig. 5-9 (c, d). As mentioned above, at 108 mA the device abruptly transitions to harmonic mode-locked operation. At this point, the FROG measurement once again begins to converge. The pulses in Fig. 5-9 (e through h) are those of the harmonic mode-locked region, and have pulse widths of approximately 6 ps. Beyond the region of harmonic mode-locking, the device enters an unstable regime wherein no FROG trace can

converge. As seen in Fig. 5-7, at the injection current of 130 mA, the device once again returns to fundamental mode-locking; however, this region does not produce converged FROG pulses. This final case is shown in Fig. 5-9 (i, j). In terms of the group delay dispersion (*GDD*) discussed in section 5.3, calculations of the second derivative of the spectral phase with respect to angular frequency yield approximately constant values of 21.5, -17.7 and 23.8 ps^2 at I = 70, 108 and 110 mA, respectively. The negative value of *GDD* arises from the reversal of the asymmetry that occurs at I=108 mA. The reduced absolute value of the *GDD* under these circumstances is consistent with the observations made in reference to Figs. 5-3a and 5-3c where the |*GDD*| was show to reduce upon reversal of the asymmetry. This is potentially related to reduced values of line-width enhancement factor under these biasing conditions [10]

Non-linear double pulsing is not only an experimental observation, but it has been predicted by the numerical DDE model [16]. Therein, the simulated regimes of two pulses per roundtrip, three pulses per roundtrip, 4 pulses per roundtrip and potentially even 5 pulses per roundtrip were demonstrated. The number of operational regimes was shown to be highly voltage dependent such that higher voltages favored the non-linear dynamics [16]. This is consistent with the experimental results presented here. The reverse bias of 5 V was selected in Figs. 5-7 through 5-9 because it produced a regime of harmonic mode-locked operation. The lower voltages did not demonstrate this type of operation. It is also noted that the devices having a short absorber (L_a=0.8 and 1.0-mm) were considerably more likely to exhibit the non-linear dynamics. Devices having longer absorber lengths did not have any regions of harmonic mode-locking. This study marked the first demonstration

of the stability associated with harmonic mode-locked operation. It has now been shown that there is a 10 mA range wherein the 1.0-mm absorber device exhibits stable harmonic mode-locking. This is not only desirable for increased aggregate bandwidths for data transmission architectures, but also has practical utility for selectable pulse repetition rates from a single device.
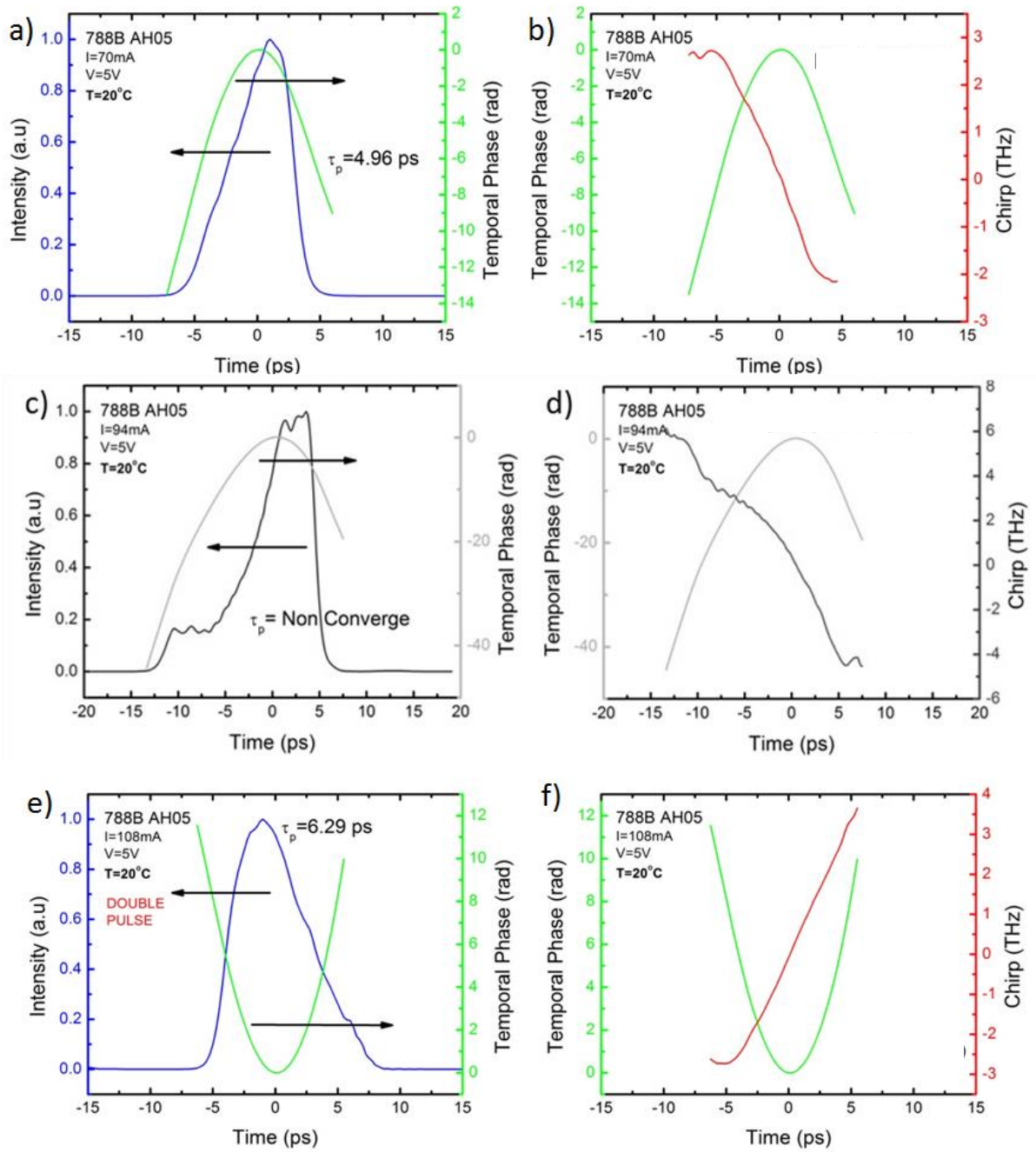
Figure continues on the next page
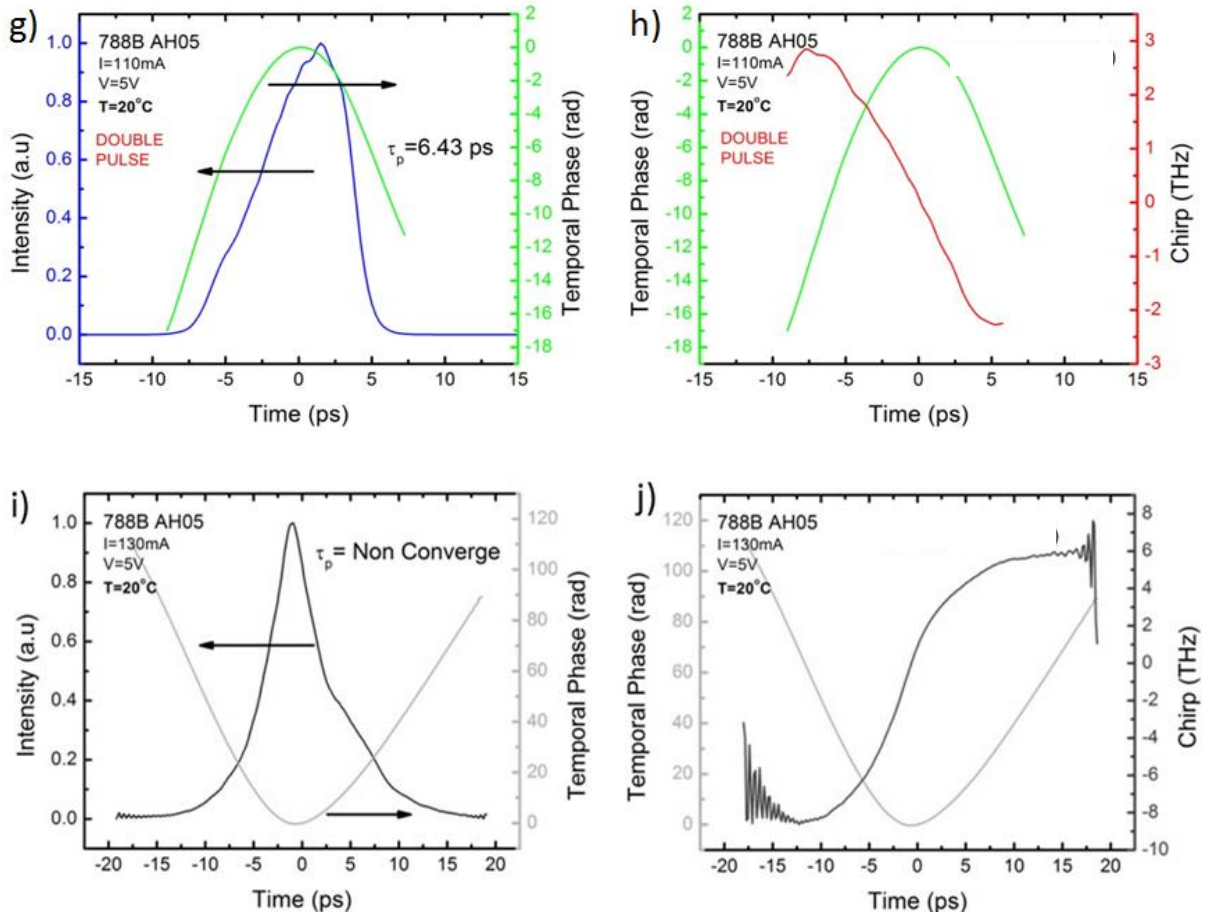
Figure 5-9. Demonstration of stable double pulsing in a quantum dot mode-locked laser. The evolution of the optical pulse train is shown for increasing current at T=20 °C and reverse bias of V=5 V. The forward injection currents are (a, b) I=70 mA, (c, d) I=94 mA, (e, f) I=108 mA, (g, h) I=110 mA and (i, j) I=130 mA. Mode-locking at the fundamental repetition rate occurs for (a through d) then enters a region of double pulsing shown in (e through j). Increasing the current further, the device returns to the fundamental repetition rate shown in (i, j). The plots displayed in grey scale represent regions where FROG did not converge; (c, d) and (i, j).

5.4 <u>Effective Current Density in the Active Layer</u>

In this final section of chapter 5, the impact of effective current density on device performance is discussed. As the next generation of mode-locked laser designs for high temperature operation are being developed, careful consideration should given to the ridge waveguide geometry. In chapter 2 it was shown that for the same applied current density, a device having a narrower ridge width will have a lower effective current density. This was attributed to an increase lateral current spreading into the cladding layer in the narrow ridge. It was subsequently demonstrated that the threshold current density in the wider 5-µm ridge width device was indeed lower than that of the narrower 3.5-µm ridge device (Fig. 2-8). We now examine the relative impact that this has on the operational range of the mode-locked lasers.

One would expect that the device having a higher effective current density should exhibit better mode-locking characteristics, given that increased levels of injection current increases the susceptibility to non-linear effects [4]. Examining this further, an experimental operational map has been constructed for the 3.5-µm device (ZLG788A AV06). The operational range of this device is compared to that of Fig. 4-4, which is the operational map for the equivalent L_a=1.2-mm device with a 5.0-µm ridge width (ZLG788B AH09). In Fig. 5-10, the resulting operational maps are shown side-by-side for convenience. There are three representations of the maps. The first, Figs. 5-10a and 5-10b, is shown for the x-axis in units of mA; this is equivalent to the maps presented in chapter 4. In the second, Figs. 5-10c and 5-10d, the x-axis has been normalized for current density to take into account the different ridge widths. For the third and final variation, Figs. 5-10e

and 5-10f, the x-axis carries the units of mW/μm and is a measure of the output power

which has been normalized for the different ridge widths. It is clearly noted from Fig. 5-

10c and 5-10d that mode-locking occurs at much higher current densities in the 3.5-μm

device. It is also noted that while the 5-μm device exhibits narrow pulse generation at

threshold, the onset of narrow pulses in the 3.5-μm ridge that does not occur directly until

significant currents above threshold. This is a direct consequence of the reduced effective

current density in the narrow ridge device, which increases the threshold current density

[20]. It follows that with higher current density, an increased level of spontaneous emission

is present at the onset of mode-locking. This acts to broaden the pulses at onset such that

they do not meet the criteria for constructing the contours of the operational map. As the

current is increased, the spontaneous emission noise is reduced and the pulses narrow;

however, as seen in Fig. 5-10, a manifest gap occurs between threshold and the onset of

narrow pulse generation for the 3.5-μm device.

The upper current limit of the narrow pulse generation is found to be related to

power. For the same power, the photon density will be greater in the narrow ridge device

as a result of tighter optical confinement, thus the operational maps in Figs. 5-10e and 5-

10f show the output power normalized to the ridge waveguide width and expressed in units

of (mW/μm). It is observed that the limit where pulses become too wide to satisfy the

criteria for the maps is approximately the same for both devices. For example, the cutoff

normalized power for a reverse bias of 5 V at 40 $^{\circ}$C is 17.8 mW/μm in the 3.5 μm ridge

device, and 17.3 mW/μm in the 5 μm device. The cutoff normalized power for a reverse

bias of 5 V at 20 $^{\circ}$C is 10.3 mW/μm in the 3.5 μm device and 10.8 mW/μm in the 5 μm

device. Given that the onset of narrow pulse generation is delayed due to the lower effective current density, and coupled with the observation that the upper current cutoff for narrow pulse generation occurs at approximately the same photon density, it follows that the operable range is significantly reduced in the narrow ridge device. This is consistent with the observations of Fig. 5-10, and is a valuable study for processing designs of the ridge waveguide geometry as it suggests that a wider ridge waveguide can increase the range of operational stability by virtue of improved effective current density in the active layer of the device. As a next step, an experimental study of the performance of devices with different ridge heights, or thicknesses of the unetched cladding layer, would be worthwhile.

In this chapter some of the key physical mechanisms that impact pulse stability have been examined. For the first time, improvement in operational range at higher temperature has been explained by a correlation between reduced values of unsaturated absorption and low values of the time-bandwidth product. This is a positive consequence of the gain peak walking-off of the absorption peak at elevated temperature. A state-of-the-art measurement system, FROG, was also introduced and subsequently used to verify the evolution of the time-bandwidth product over temperature. Furthermore, the non-linear effect of double-pulsing was studied and shown for the first time to be a stable condition experimentally. This was verified by convergence of pulses in the FROG which is currently the most accurate indication of stable mode-locking. Finally, the waveguide geometry and the relative impact on the range of operation across temperature were discussed.
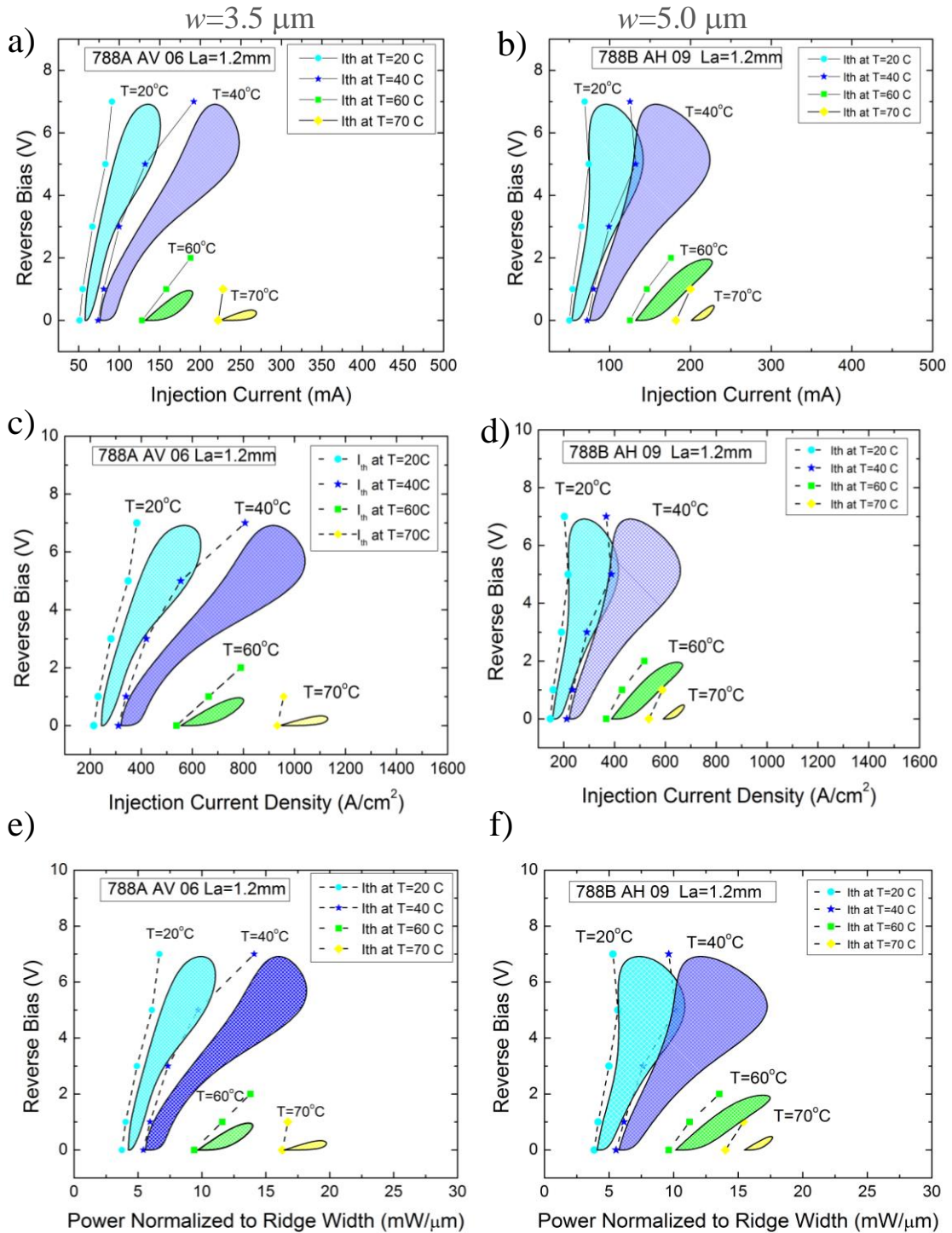
Figure 5-10. Measured operational maps for two devices having same saturable absorber length but with different ridge waveguide widths of (a, c, d) 3.5 μm and (b, d, e) 5.0 μm. X-axis in units of mA (a,b), current density (c, d) and power normalized to the ridge waveguide width (e, f).

REFERENCES FOR CHAPTER 5

[1] K. Lau, and J. Paslaski, "Condition for short pulse generationin ultrahigh frequency mode-locking of semiconductor lasers," IEEE Photon Technol. Lett., vol. 3, no. 11, pp. 974–976 (1991)

[2] J. Palaski, and K. Y. Lau, "Parameter ranges for ultrahigh frequency mode-locking of semiconductor lasers. Appl. Phys. Lett. vol. 59, no. 1, pp. 7-9 (1991)

[3] C.-Y. Lin, Y.-C. Xin, Y. Li, F. L. Chiragh, and L. F. Lester, "Cavity design and characteristics of monolithic long-wavelength InAs/InP quantum dash passively mode-locked lasers," Opt. Exp., vol. 17, no. 22,pp. 19739–19748 (2009)

[4] GP Agrawal, and NA Olsson,"Self-phase modulation and spectral broadening of optical pulses in semiconductor laser amplifiers," IEEE J. Quan.Elect.vol. 25.no. 11 (1989)

[5] M. A. Cataluna, D. B. Malins, A. Gomez-Iglesias, W. Sibbett, A. Miller, and E. U. Rafailov, "Temperature dependence of electro-absorption dynamics in an InAs quantum-dot saturable absorber at 1.3 μm and its impact on mode-locked quantum-dot lasers" Appl. Phys. Lett. 97, 121110 (2010).

[6] Weidong Yang, Roger R. Lowe-Webb, Hao Lee, and Peter C. Sercel, "Effect of carrier emission and retrapping on luminescence time decays in InAs/GaAs quantum dots," Phys. Rev. B 56, 13314–13320 (1997)

[7] Yan Li, Luke F. Lester, Derek Chang, Carsten Langrock, M. M. Fejer, and Daniel J. Kane. "Characteristics and instabilities of mode-locked quantum dot lasers," Optics Express, vol. 21, no. 7, (2013)

[8] G. Imeshev, M. A. Arbore, M. M. Fejer, A. Galvanauskas, M. Fermann, and D. Harter, "Ultrashort-pulse second-harmonic generation with longitudinally nonuniform quasi-phase-matching gratings: pulse compression and shaping "JOSA B, vol. 17,no. 2, pp. 304-318 (2000)

[9] Schober, A. M., G. Imeshev, and M. M. Fejer. "Tunable-chirp pulse compression in quasi-phase-matched second-harmonic generation." Optics letters, vol. 27, no. 13, pp. 1129-1131 (2002)

[10] Heffner, B.L., "Accurate, automated measurement of differential group delay dispersion and principal state variation using Jones matrix eigenanalysis," Photonics Technology Letters, IEEE, vol.5, no.7, pp.814-817 (1993)

[11] P. F. Curley, Ch. Spielmann, T. Brabec, F. Krausz, E. Wintner, and A. J. Schmidt, "Operation of a femtosecond Ti:sapphire solitary laser in the vicinity of zero group-delay dispersion," Optics Letter, vol. 18, no. 1, (1993)

[12] R. Raghunathan, M. Crowley, F. Grillot, Y. Li, J. K. Mee, V. Kovanis, L.F. Lester, "Pulse Characterization of Passively Mode-locked Quantum Dot Lasers Using a Delay Differential Equation Model Seeded with Measured Parameters." IEEE J. Selected Topics in Quan. Electron. No. 99, pp. 1 (2013)

[13] H. Schmeckebier, G Fiol, . Meuer, D. Arsenijevic, and D. Bimberg, "Complete pulse characterization of quantum-dot mode-locked lasers suitable for optical communication up to 160 Gbit/s," Optics Express, vol. 18, no. 4 pp. 3415-3425 (2010)

[14] A. Aboketaf, A. W. Elshaari, and S. F. Preble, "Optical time division multiplexer on silicon chip" Opt. Express 18, 13529-13535 (2010)

[15] A. A. Aboketaf, L. Cao, D. Adams, A. W. Elshaari, S. F. Preble, M. T. Crowley, L. F. Lester and P. Ampadu, "Hybrid OTDM and WDM for multicore optical communication," IGCC, pp.1-5, (2012)

[16] Raghunathan, J. K. Mee, M. Crowley, F. Grillot, V. Kovanis, L.F. Lester, "Modeling and Characterization of Pulse Shape and Pulse Train Dynamics in Two-Section Passively Mode-Locked Quantum Dot Lasers," SPIE OPTO 86190C-86190C-11 (2013)

 [17] Li, Y., Chiragh, F. L., Xin, Y.-C., Lin, C.-Y., Kim, J., Christodoulou, C. G. and Lester, L. F., "Harmonic mode-locking using the double interval technique in quantum dot lasers," Opt. Express, 18(14), pp. 14637-14643, (2010).

[18] C. Y. Lin, F. Grillot, N.A. Naderi, Y. Li, J.H. Kim, C.G. Christodoulou, L.F. Lester, "RF linewidth of a monolithic quantum dot mode-locked laser under resonant feedback." IET Optoelectronics, vol. 5, no. 3, pp 105-109 (2011)

[19] R. L. Fork, B. I. Greene, and C. V. Shank, "Generation Of optical pulses shorter than 0.1 psec by colliding pulse mode-locking," *Appl. Phys. Lett*., vol.38, pp. 671-672 (1981)

[20] Rui Wang, Soon Fatt Yoon, Han Xue Zhao, and Chun Yong Ngo, "Geometrical Effects on Characteristic Temperatrure and Modal Gain of InAs/GaAs Quantum-Dot Lasers," IEEE Phot. Tech. Lett. vol. 23, no. 12 (2011)

Chapter 6 – Conclusions/Future Work

6.1 Summary

In this dissertation, a detailed study of the *time-domain* characteristics of optical pulses generated from quantum dot passively mode-locked lasers was performed. Devices having different cavity geometry and ridge waveguide design were extensively studied over a wide range of operating temperatures and currents using analytical modeling techniques to predict the regimes of operation. Experimental measurements of the operational range and ultra-sensitive frequency resolved optical gating (FROG) pulse measurements were also conducted. Several milestone achievements were accomplished throughout the course of this dissertation. The results are summarized for each chapter below.

In chapter 2, the details of the quantum dot mode-locked lasers used throughout the dissertation were given. This included a description of the active layer composition and cavity geometry of the two-section mode-locked lasers and the multi-section single pass emitter. Additionally, the impact of the ridge waveguide geometry on the effective current density, and consequently the threshold current density, was calculated and experimentally examined. A previously unpublished expression for J_{eff} was derived, and it was found that the narrow ridge device had a lower effective current density as a result of increased lateral current spreading into the cladding region [1]. It was subsequently verified, through measurements of the threshold current density across voltage and temperature, that the 3.5-μm ridge-width device had a higher threshold current density than the 5-μm ridge-width device.

In chapter 3, using a segmented contact method [2,3], the gain and loss characteristics of a 6-stack DWELL [4] semiconductor laser structure were measured. The resulting modal gain and absorption spectra were used to derive the input parameters of an analytical mode-locked model. Analytical predictions of the regions of operational stability for a given cavity geometry across a wide range of temperatures were calculated. These were expressed in the form of stability maps. The stability maps demonstrated that the path toward high temperature operation was to move to a short absorber device. The maps also predicted record temperature performance could be achieved from a device having an absorber to gain length ratio of 0.11. In the final section of chapter 3 some of the predictive capabilities of the model were explored and it was shown the n-type or p-type dopants could potentially be used to increase the range of operational stability.

In chapter 4, following the generation of the theoretical stability maps, five different two-section mode-locked lasers having absorber to gain length ratios of $L_a/L_g = 0.11$, 0.14, 0.18, 0.21 and 0.25 were characterized over temperature. Experimental measurements of the pulsed output in the time domain lead to the construction of operational maps in which the regions within the contours of the maps represented injection current and absorber reverse bias conditions that produced pulses of FWHM less that 19 ps. Record temperature performance was observed where mode-locked pulses with pulse widths $\leq$ 19 ps were emitted from 20-110ºC in the mode-locked laser having a 0.8-mm absorber length. Additionally, excellent agreement between the modeled stability maps of chapter 3 and experimental operational maps was found. For the case of a grounded absorber, the model

was able to correctly predict the maximum temperature where mode-locking was observed in each device. The model also correctly predicted the transition temperatures from ground-state operation to excited-state operation. As a final observation, it was noted that the pulse time-bandwidth product reduced to a minimum around 60 $^{\circ}$C. This was subsequently explained in chapter 5.

In chapter 5 some of the key physical mechanisms that impact pulse stability were discussed. For the first time, improvement in operational range at higher temperature was explained by a correlation between reduced values of unsaturated absorption and low values of the time-bandwidth product. This was shown to be a positive consequence of the gain peak walking-off of the absorption peak at elevated temperature. Furthermore, a state-of-the-art measurement system, FROG, was introduced and subsequently used to verify the evolution of the time-bandwidth product over temperature. FROG pulse measurements, which are currently the most accurate indication of stable mode-locking, were also used to examine the non-linear effect of double-pulsing. For the first time, this was shown to be a stable effect. Finally, the waveguide geometry and the relative impact on the range of operation across temperature were discussed. It was demonstrated that the reduced effective current density in the narrow ridge device results in an increased range above threshold before narrow pulse generation can occur. This was the attributed to increased spontaneous emission at higher injection currents. It was also shown that the cutoff for narrow pulse generation occurs for the same photon density in both devices and thus the operational range was reduced in the narrow ridge device.

The results presented in this dissertation have strong implications for the next generation of mode-locked laser design. Clearly, the record temperature performance of the quantum dot mode-locked lasers makes them highly attractive for optical data transmission architectures in extreme environments, such as those in space. More practically speaking, given the discovery of the strong correlation between reduced values of unsaturated absorption and low time-bandwidth product, a grating could be used in the future to select a lasing wavelength to have the minimum unsaturated absorption. This would be possible due to the inhomogeneously broadened gain bandwidth [5, 6]. Techniques such as these can be used to reduce the optical pulse width of the laser and thus lending it more favorably for use in the WDM/OTDM architecture [7] discussed in chapter 1. Perhaps even more desirable, the possibility of uncooled OTDM has also expressed [8].

6.2 <u>Future Work</u>

In the final section of this dissertation the potential to further reduce dispersion in the laser cavity through biasing techniques of a three-section mode-locked laser is discussed. Improvements in the time-domain characteristics of the optical pulses emitted from a quantum dot passively mode-locked laser could potentially be accomplished with a novel method for intra-cavity chirp compensation in a three section mode-locked laser. This has the potential to reduce the optical pulse width to its Fourier limit. As mentioned in chapter 1, the parameter that quantifies the level of chirp a pulse experiences for a given laser cavity is known as the linewidth enhancement factor (α-parameter). The α- parameter depends on the ratio of the change in the real part of the refractive index with respect to carrier density (*dn/dN*) to the differential gain (*dg/dN*) of the material [9]:

147

$$\alpha = \frac{\Delta n'}{\Delta n''} = \frac{-4\pi}{\lambda} \frac{dn/dN}{dg/dN}$$

<div align="right">(6-1)</div>

In contrast to quantum well lasers, wherein the carrier density is clamped at threshold, in quantum dot lasers the carrier density is not clearly clamped because of the energy relaxation processes in the dots [10]. Accordingly the accumulation of carriers can occur in the excited-state and other non-lasing states even when the ground-state emission is still occurring. This has interesting implications for quantum dot lasers because it means a wide range of α–parameters can be achieved by simply tuning the applied bias current.

a. *Negative Linewidth Enhancement Factor*

Of particular curiosity is the prospect of negative linewidth enhancement factor, which has been experimentally demonstrated using the AM/FM method by [11]. Subsequent calculations by Frédéric Grillot *et. al.*[12] showed good agreement with the previous experimental data, including the prediction of negative α-parameter in the ground-state when significant injection current was applied. Fig. 6-1 shows the calculated ground-state α-parameter (black dots) from [12], with the superimposed experimental measurements (red stars) form [11]. The α-parameter is shown to initially increase with injected current. This is because filling of the carriers in the excited-state is readily occurring while the laser is emitting from the ground state. Then, at some bias current above threshold, stimulated emission from the excited state occurs and the carrier density in the ground state significantly reduces. In other words, the ground-state gain collapses

upon the onset of excited-state lasing and this leads to the negative linewidth enhancement factor that was experimentally observed.
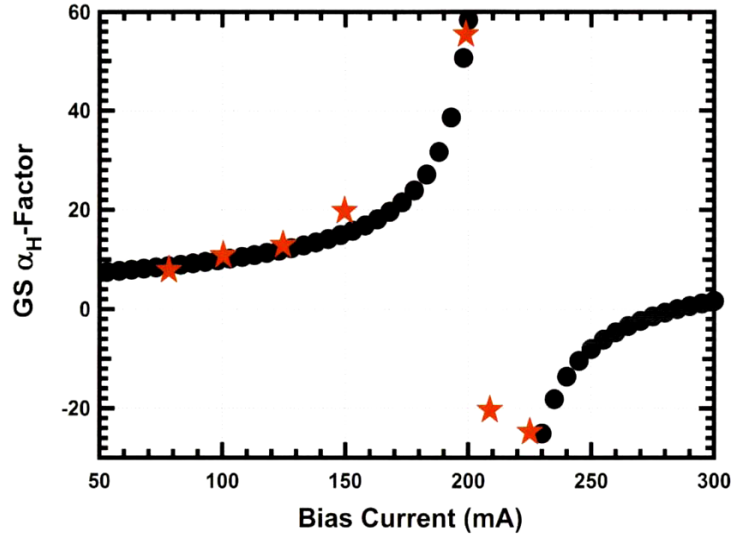
Figure 6-1. Calculated ground-state linewidth enhancement factor (black dots) in a quantum dot laser, and experimentally measured (AM/FM technique) linewidth enhancement factor values (red stars).

b.   Three-section mode-locked laser

Leveraging the idea of a negative linewidth enhancement factor, one can envision a three-section mode-locked lasers wherein part of the laser cavity is biased heavily to induce the negative α-parameter while the remainder of the cavity is biased to transparency so that the optical mode is not attenuated as it moves through that section. This three-section laser is now said to encompass offsetting regions of positive and negative linewidth enhancement factor. Here pulse compression occurs without the need for external hardware

such as a Chirped Fiber Bragg-Grating (CFBG) [13]. This then becomes an innovative, compact and inexpensive way to reduce the optical chirp within the cavity, consequently, increasing the peak power, stability and potential number of optical time division multiplexing channels.

a)

I_{inj}=0-500 mA

V_r=0-7 V

b)

I_{inj}=0-500 mA

I_{Inj}=0-250 mA

FIB

V_r=0-7 V
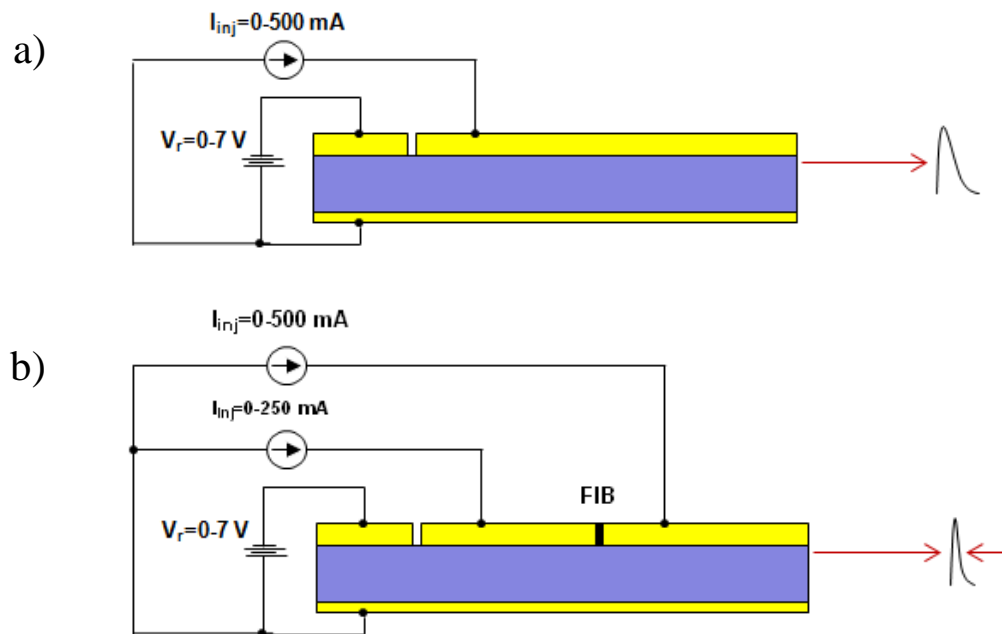
Figure 6-2. a) Schematic of a traditional two-section passively mode-locked laser. b) Three-section mode-locked laser design for intra-cavity chirp compensation. A FIB etch creates electrical isolation between adjacent gain contacts.

A schematic representation of the traditional two-section mode-locked laser and the proposed three-section mode-locked laser is given in Fig. 6-2. The section adjacent to the absorber would be biased heavily to create the negative α condition. To simplify determination of the threshold condition, the remaining section would need to be biased to transparency. This section looks like passive waveguide to the optical mode. The third section will be reverse biased to create the saturable absorber. Proper design of the three-section cavity geometry requires experimental data of the modal gain and loss profiles. This data was collected on the 788 series devices via the segmented contact method (chapter 3). Initially, the electrical isolation between adjacent gain sections can be created with a Focused Ion Beam (FIB) etch. Ultimately proton implantation would create a higher resistance between the adjacent gain sections as it would eliminate the current path though the p-type AlGaAs layer. The following expression for the threshold condition is used to determine the appropriate length of the two gain sections:

$$L_a\left[a_o + \alpha_i + \alpha_m\right] = L_g\left[g_o(J) - \alpha_i - \alpha_m\right] + L_g{}'\left[g_o(J') - \alpha_i - \alpha_m\right] \quad \text{(6-2)}$$

where L_a is the absorber section length, L_g is the length of the heavily biased gain section and $L_g{}'$ is the length of the gain section that his biased to transparency. a_o is the unsaturated absorption, α_i is the internal cavity loss, α_m is the mirror loss and $g_o(J)$ is the modal gain at current density J. By definition the losses equal the gain at transparency and thus the $L_g{}'$ term drops out. Rearranging Eqn. (6-2), the following expression is formed:

$$L_g = L_a \frac{\left[a_o + \alpha_i + \alpha_m\right]}{\left[g_o(J) - \alpha_i - \alpha_m\right]} \qquad (6\text{-}3)$$

c. Proof of Concept Demonstration

Eqn. (6-3) is used to determine the length of the heavily biased section. A proof of concept experiment has been performed on a two-section mode-locked laser having a 1.6-mm saturable absorber (ZLG788 AH16). Using the modal gain and absorption data from chapter 3, the calculated length of L_g is 1.4-mm. J_{sat} is approximately 1300 A/cm^2, and the width of the waveguide is 5 μm. Accordingly, a forward injection current of 91 mA must be applied to this section. Transparency current density is equal to 100 A/cm^2 at T=20 ºC thus the L_g' section, which has a length of 5-mm must be biased at 25 mA. In accordance with the calculations from Eqn. (6-3), a 5-mm section was electrically isolated from a 1.4-mm section via a FIB etch in the L_a=1.6-mm device, An SEM image of the cut is shown in Fig. 6-3. The gold metallization layer was completely removed; however, current can still pass through the p-type AlGaAs cladding layer. Accordingly electrical DC resistance was only measured to be about 90 Ω. Never-the-less differential pumping of the adjacent gain sections could still be performed on this device.

Preliminary Frequency Resolved Optical Gating (FROG) measurements were captured on the three-section device to verify operability (there was some concern about the effect of Ga incorporation after the FIB), and to see if pulse narrowing could be observed. In Fig. 6-4 the recovered temporal intensity, phase and chirp are shown for the three-section device under a 264 A/cm^2 uniform bias Fig. 6-4(a, b), and under differential

pumping Fig. 6-4(c, d). In the differential bias method, the short 1.4-mm section adjacent to the absorber was pumped heavily at (438 A/cm^2), while the longer 5-mm section was pumped near transparency (120 A/cm^2). These measurements were performed at T=20 ^{o}C and 0 V reverse bias on the absorber. From Fig. 6-4, improved pulse characteristics were noted. Namely, the differential pumping method had reduced the optical pulse width from 7.71 ps to 5.56 ps. However, the time-bandwidth product had increased from 2.28 in the uniform bias condition, up to 2.76 in the differential pumping condition. It follows that the 3-dB with of the optical spectrum must have increased in the latter case perhaps due to spectral broadening in the heavily biased section. It is noted that the onset of mode-locking occurred at a lower than expected current density. This could be the result of incomplete isolation of the adjacent gain sections, or there may have been some cavity losses that were overestimated.

The potential for narrow pulse generation through differential pumping has been previously examined [14, 15]. In one case a multi-section device was biased in such a way that the laser cavity contained a length of passive waveguide. Reduction in the optical pulse width by as much as 22% was demonstrated with this biasing scheme. The improved characteristics were attributed to an increase in the saturation power of the gain section by running in stronger inversion [15]. A more detailed investigation is required to determine if the observed narrowing of the optical pulse width demonstrated here is the result of intra-cavity dispersion compensation, or arises from effects similar to those in [15]. Never-the-less these results serve as a valuable first step in the demonstration of the intra-cavity chirp compensation concept.

As a next step, it would be useful to create stronger electrical resistance between adjacent gain sections. This could be accomplished with a proton implantation which has been measured to have a resistance of approximately 8 MΩ. Furthermore, the calculations of the three-section cavity geometry should take into consideration different cavity losses associated with different devices. By this it is meant that the internal loss in the 1.2-mm device of 788A might be different than the internal loss of the 1.2-mm device in 788B. If there is no means to measure the internal loss directly, an arbitrary correction factor, α', should be included in Eqn. (6-2) and used to determine the cavity geometry. α' can quickly be derived by comparing the measured threshold current density, to the calculated threshold current density from on the modal gain and absorption data. This being considered, the three section cavity geometry has been derived for the device having L_a=1.2-mm (ZLG788B AH09). The resulting lengths of the heavily biased section and the transparency biased sections are L_g=1.2-mm and L_g' = 5.6-mm, respectively. The appropriate forward injection currents are J=78 mA and J'=28 mA. It would be worthwhile to compare FROG measurements from this device under uniform bias and differential bias conditions.
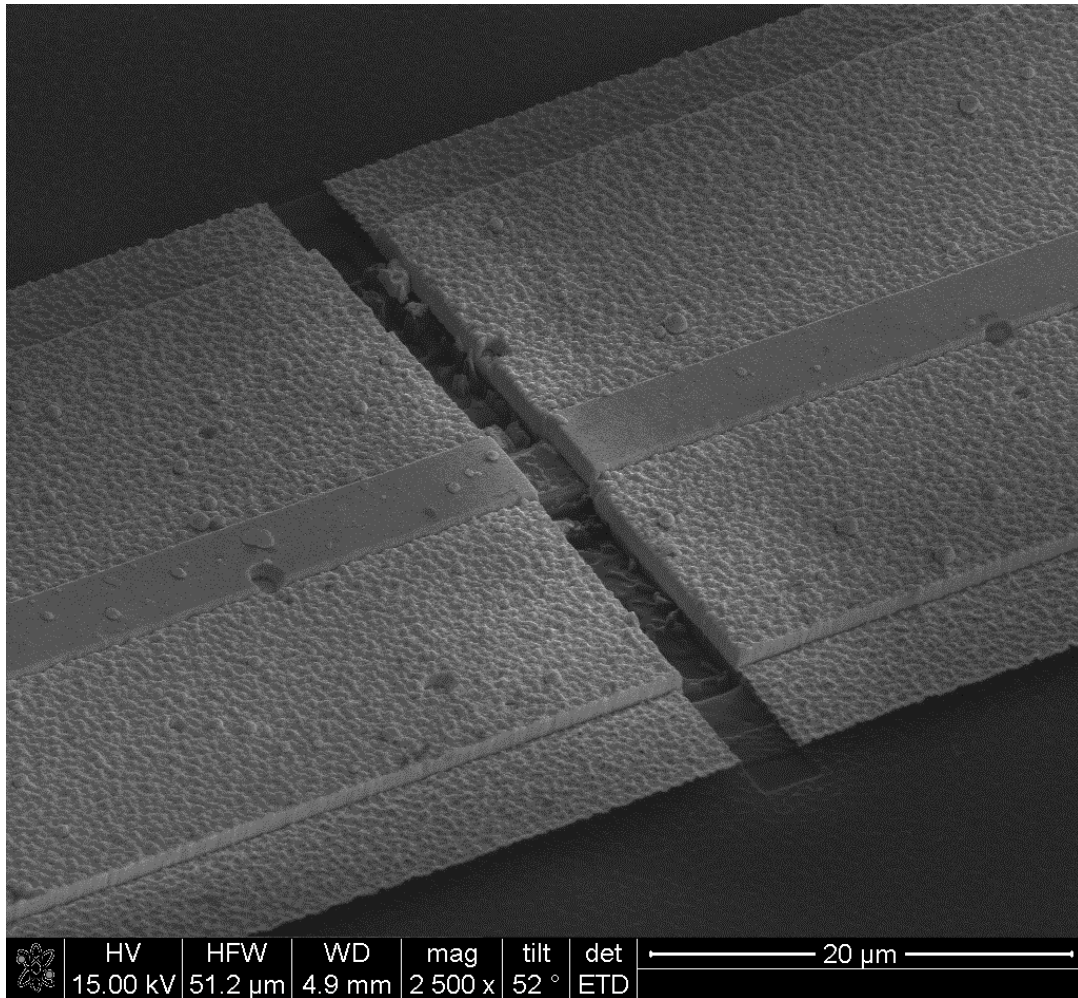
Figure 6-3. SEM image of the Focused Ion Beam (FIB) etch in the L_a=1.6-mm two section quantum dot mode-locked laser. Approximately 90 Ω of resistance was measured between adjacent gain sections. High electrical isolation was not achieved because current can still pass through the p-type AlGaAs layer.
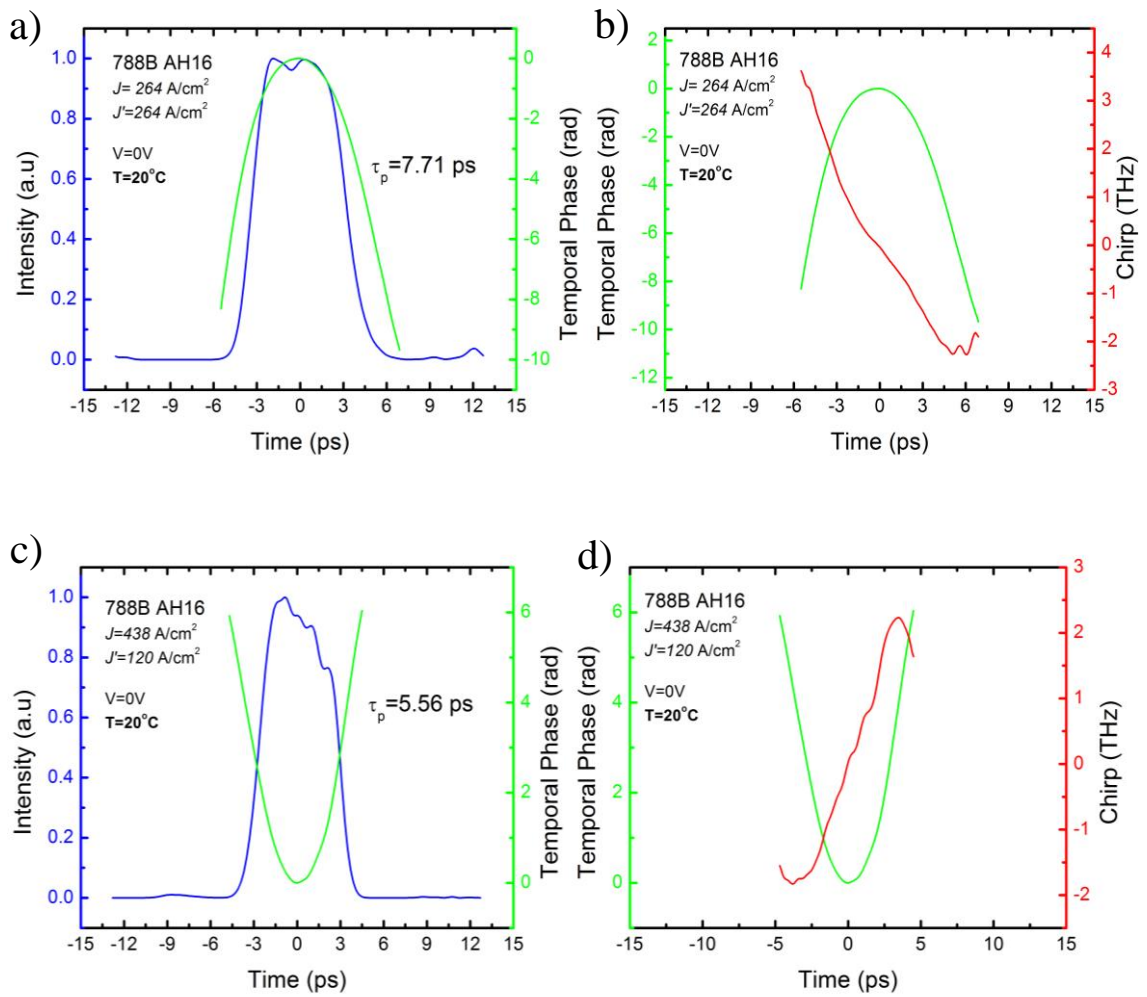
Figure 6-4. Retrieved time-domain pulse characteristics as measured by FROG on the three-section mode-locked laser at T=20 °C with 0 V applied to the saturable absorber. (a,b) Temporal intensity, phase and chirp under uniform bias and (c,d) differential pumping.

REFERENCES FOR CHAPTER 6

[1] Rui Wang, Soon Fatt Yoon, Han Xue Zhao, and Chun Yong Ngo, "Geometrical Effects on Characteristic Temperatrure and Modal Gain of InAs/GaAs Quantum-Dot Lasers," IEEE Phot. Tech. Lett. vol. 23, no. 12 (2011)

[2] Y.-C.Xin, Y. Li, A. Martinez, T. J. Rotter, H. Su, L. Zhang, A. L. Gray, S. Luong, K. Sun, Z. Zou, J. Zilko, P. M. Varangis, and L. F. Lester, "Optical gain and absorption of QD measured using an alternative segmented contact method" IEEE J. Quantum Electron. 42, 725 (2006)

[3] P. Blood, G. M. Lewis, P. M. Smowton, H. Summers, J. Thomson, and J. Lutti, "Characterization of semiconductor laser gain media by the *s*egmented contact method" IEEE J. Sel. Top. Quantum Elect., 9, 1275 (2003)

[4] G.T. Liu, A. Stintz, H. Li, K.J. Malloy and L.F. Lester, "Extremely low room-temperature threshold current density diode lasers using lnAs dots in InGaAs quantum well" Elect. Lett., vol. 35, pp. 1163-1165, (1999)

[5] L. F. Lester, A. Stintz, H. Li, T. C. Newell, E. A. Pease, B. A. Fuchs, K. J. Malloy, "Optical characteristics of 1.24-µm InAs quantum-dot laser diodes," Photonics Technology Letters, IEEE , vol.11, no.8, pp.931-933 (1999)

[6] S W Osborne, P Blood, PM Smowton, Y C Xin, A Stintz, D Huffaker, and L F Lester, "Optical absorption cross-section of quantum dots," J. Phys. Condens. Matter, vol. 16, no. 35, pp. 3749-3756 (2004)

[7] A. A. Aboketaf, L. Cao, D. Adams, A. W. Elshaari, S. F. Preble, M. T. Crowley, L. F. Lester and P. Ampadu, "Hybrid OTDM and WDM for multicore optical communication," IGCC, pp.1-5, (2012)

[8] J. K. Mee, M. T. Crowley, D. Murrell, R. Raghunathan, L. F. Lester, "Temperature Performance of Monolithic Passively Mode-Locked Quantum Dot Lasers: Experiments and Analytical Modeling," Selected Topics in Quantum Electronics, IEEE Journal of , vol.19, no.4, pp.1101110 (2013)

[9] C. H. Henry, "Theory of the Lindwidth of Semiconductor lasers," IEEE J. Quantum. Electronics. vol. QE18, no. 2 pp. 259-264 (1982)

[10] Saito, H.; Nishi, Kenichi; Kamei, A.; Sugou, Shigeo, "Low chirp observed in directly modulated quantum dot lasers," Photonics Technology Letters, IEEE , vol.12, no.10, pp.1298-1300 (2000)

[11] Grillot, F.; Dagens, B.; Provost, J.; Hui Su; Lester, L.F., "Gain Compression and Above-Threshold Linewidth Enhancement Factor in 1.3-μm InAs–GaAs Quantum-Dot Lasers," Quantum Electronics, IEEE Journal of , vol.44, no.10, pp.946-951 (2008)

[12] A. V. Uskov, E. P. O'Reilly, D. McPeake, N. N. Ledentsov, D. Bimberg, and G. Huyet, "Carrier-induced refractive index in quantum dot structures due to transitions from discrete quantum dot levels to continuum states," Appl. Phys. Lett., vol. 84, pp. 272–274 (2004)

[13] K.O. Hill, Y. Fujii, D.C. Johnson, B Kawasaki, "Photosensitivity in optical fiber waveguides: application to reflection fiber fabrication". Appl. Phys. Lett. vol. 32 no. 10, pp. 647 (1978)

[14] K. Brown, B. Wysocki, M. Fanto, J. Malowicki, V. Kovanis, and L. F. Lester, "Control over spectral content via differential pumping of a monolithic passively mode-locked quantum dot laser", Proc. SPIE 6572, Enabling Photonics Technologies for Defense, Security, and Aerospace Applications III, 65720A (2007)

[15] Y.-C Xin, Y. Li, Vassilios Kovanis, A. L. Gray, L. Zhang and L. F. Lester, "Reconfigurable quantum dot monolithic multi-section passive mode-locked lasers," Optics Express, vol. 15, no. 12, pp. 7623-7633 (2007)

APPENDIX A

Complete Modal Gain Data as a function of current density and Temperature

——	I=22 mA
——	I=20 mA
——	I=15 mA
——	I=12 mA
——	I=10 mA
——	I=8 mA
——	I=7 mA
——	I=5.5 mA
——	I=4 mA
——	I=3.5 mA
——	I=3 mA
——	I=2 mA
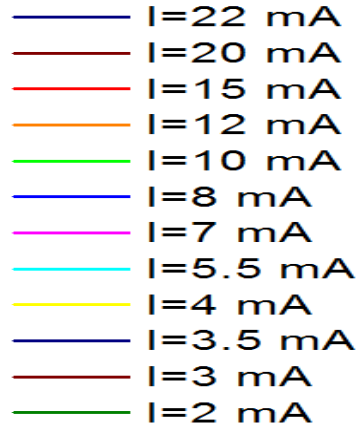
Figure legend for the modal gain data shown in this appendix

788 Multisection
T=80C

788 Multisection
T=100C

788 Multisection
T=110C

788 Multisection
T=120C
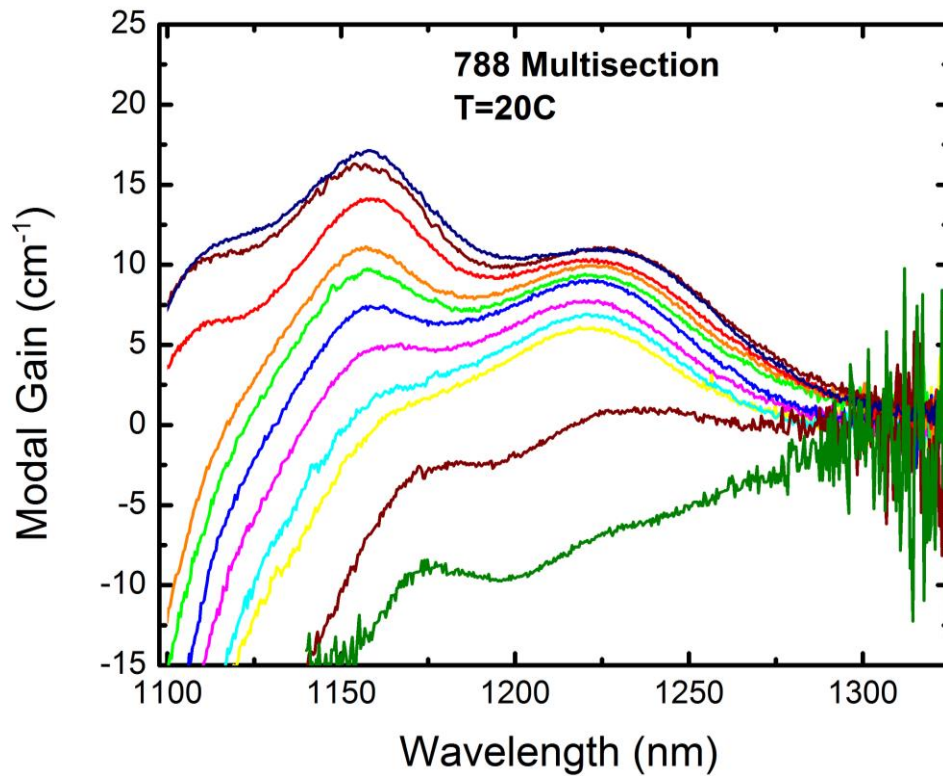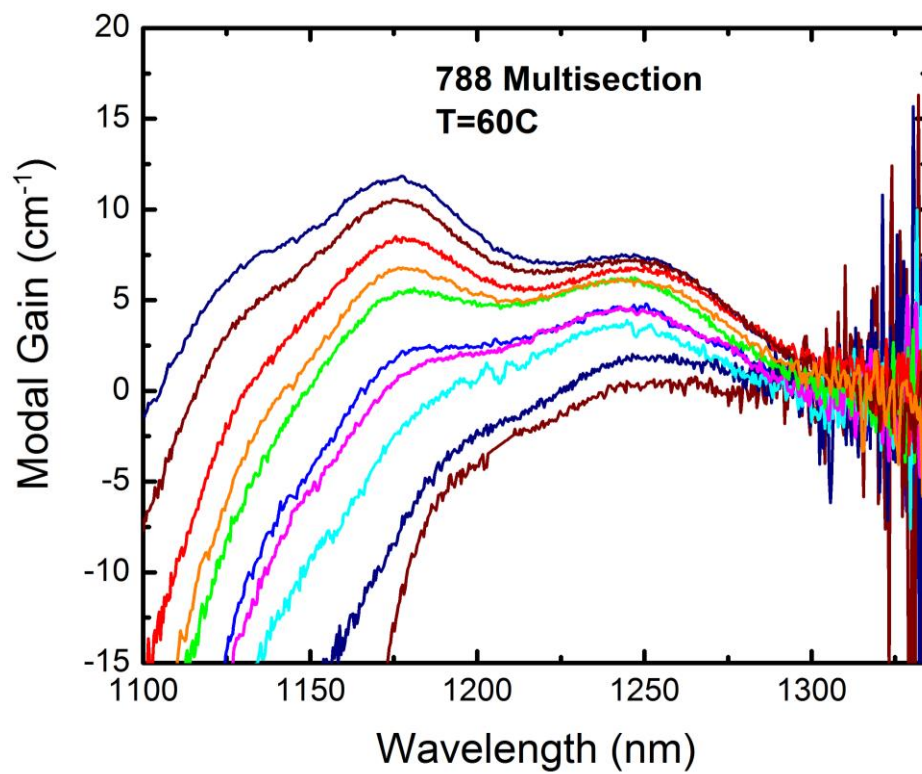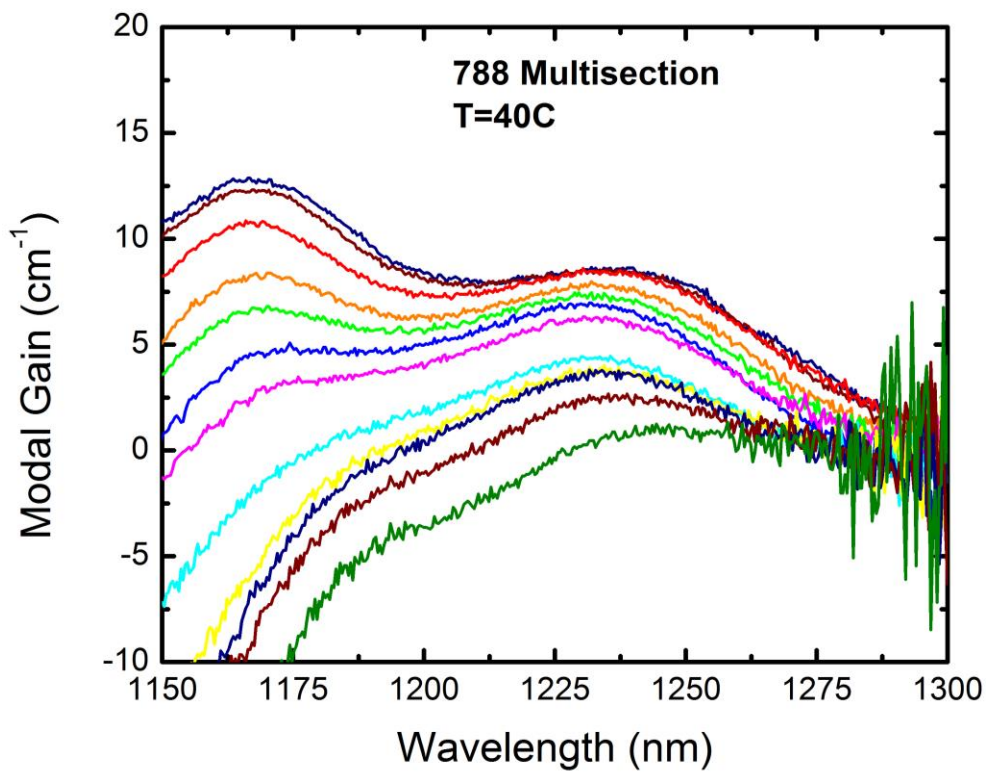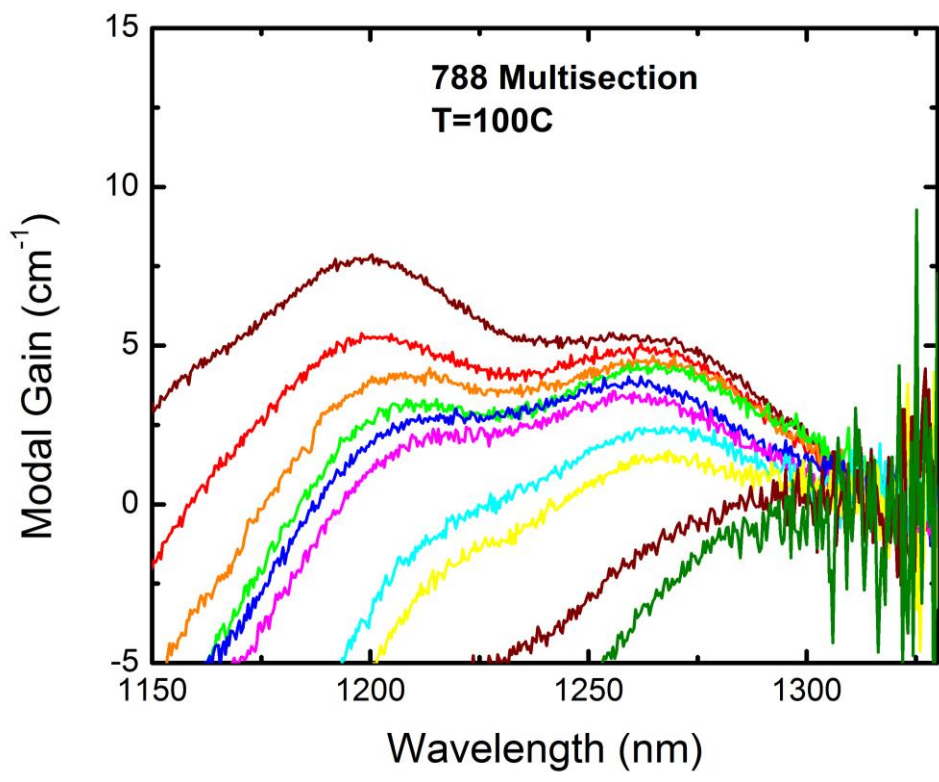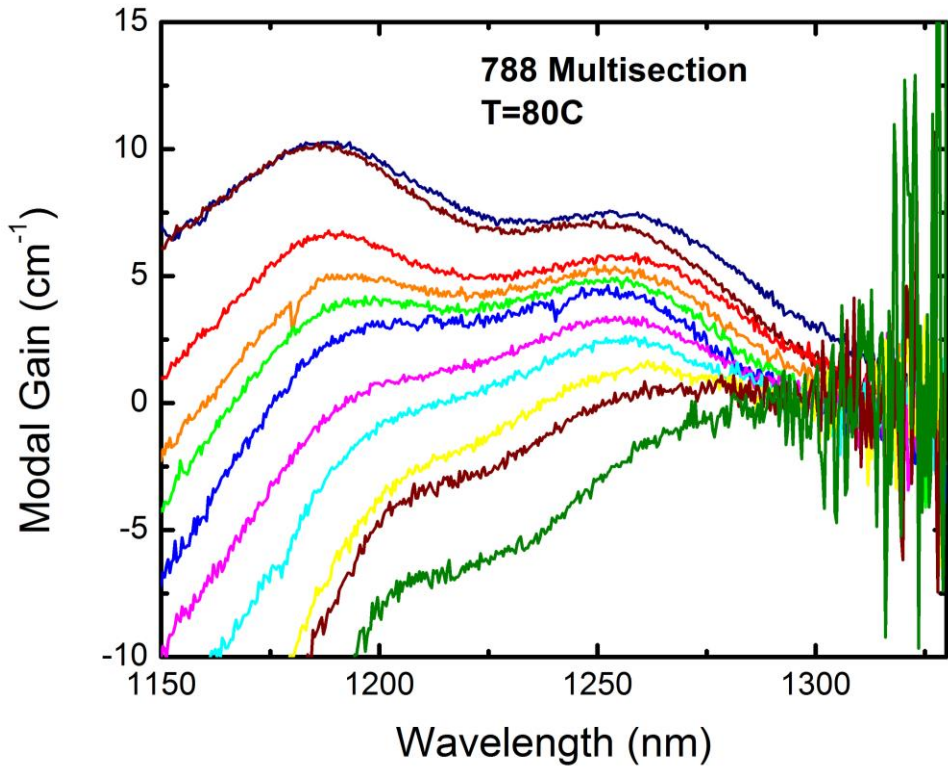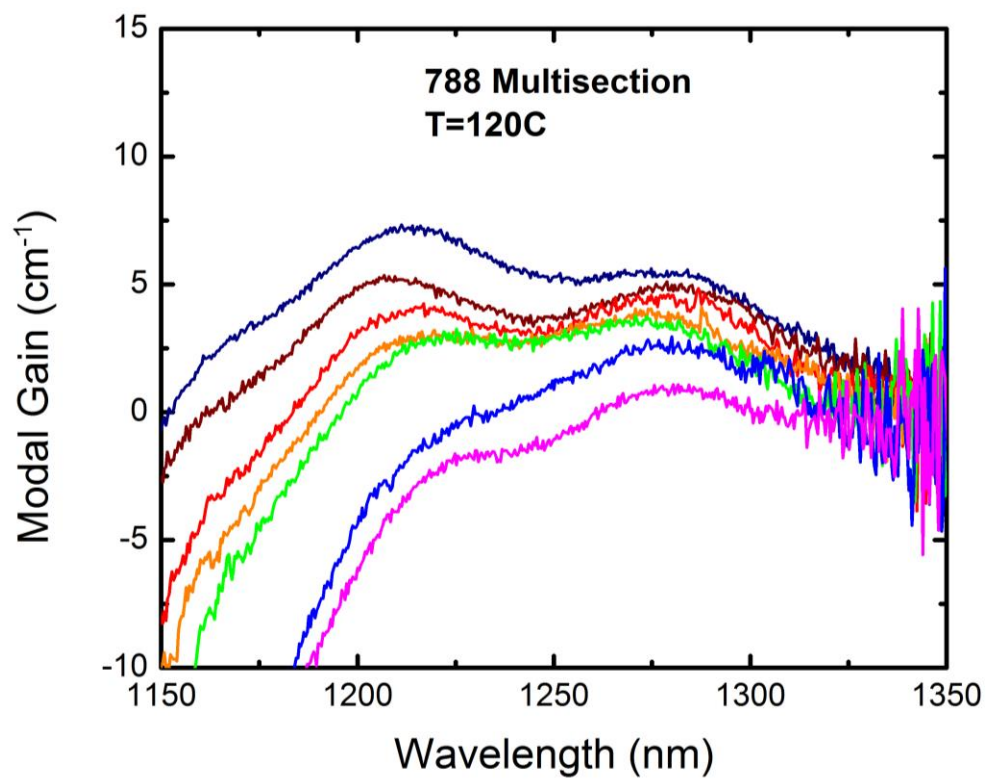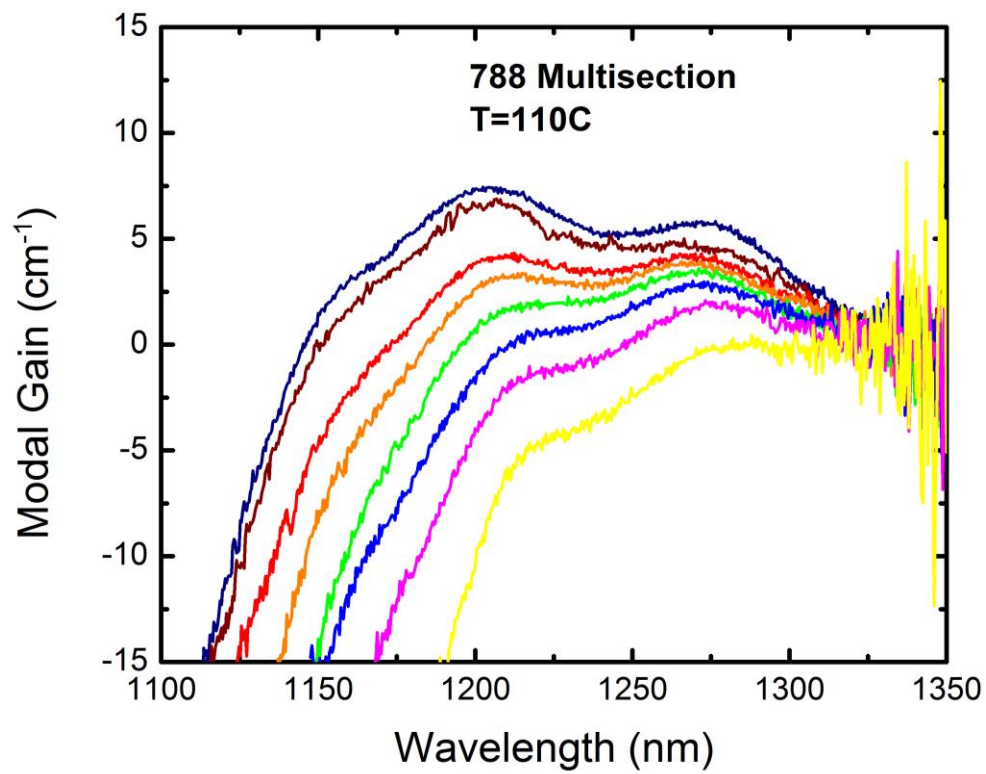
APPENDIX B

Complete Modal Absorption data as a function of reverse voltage and temperature
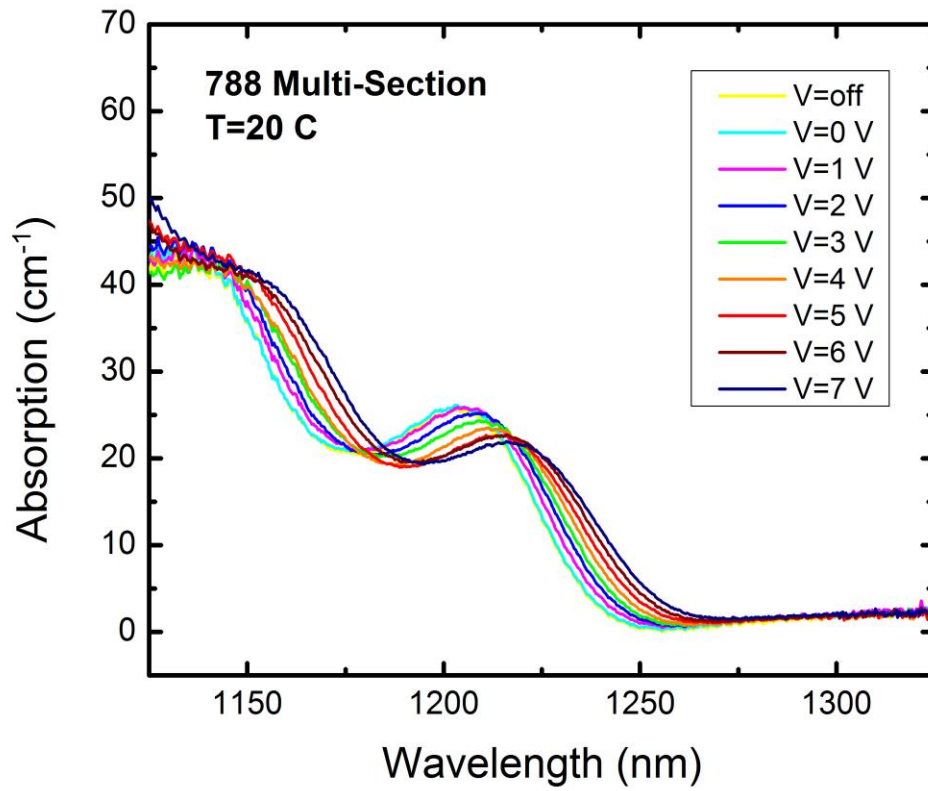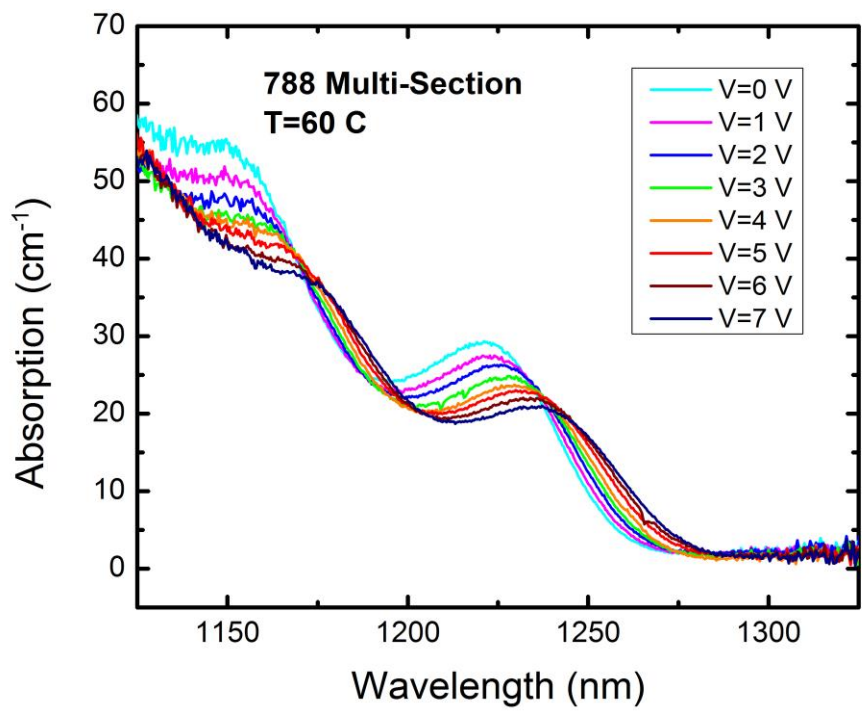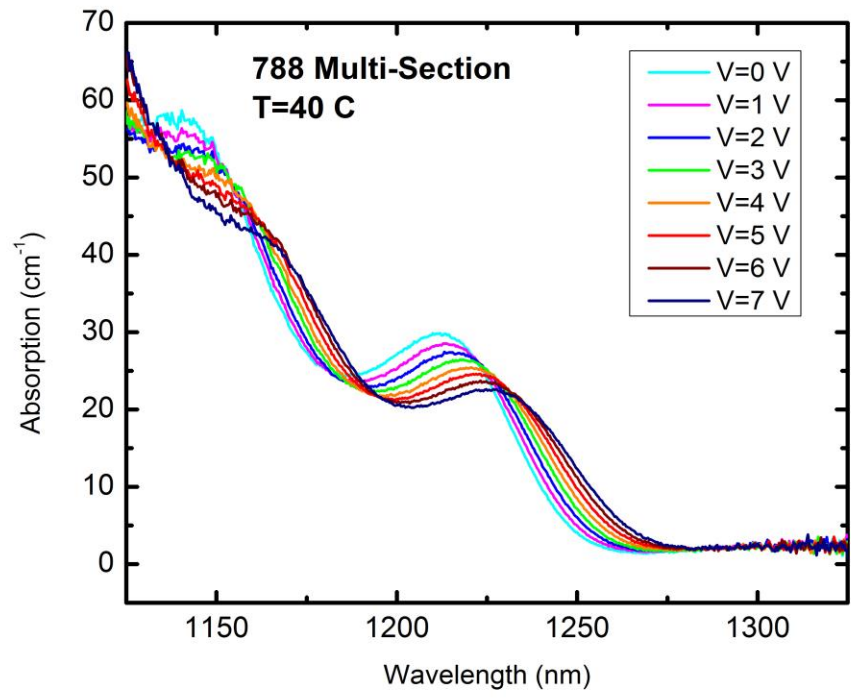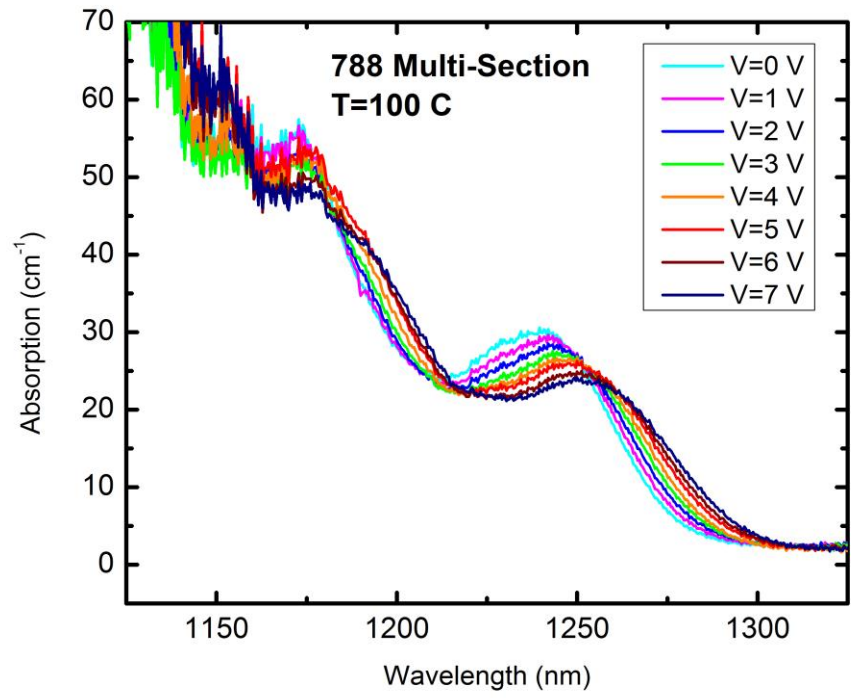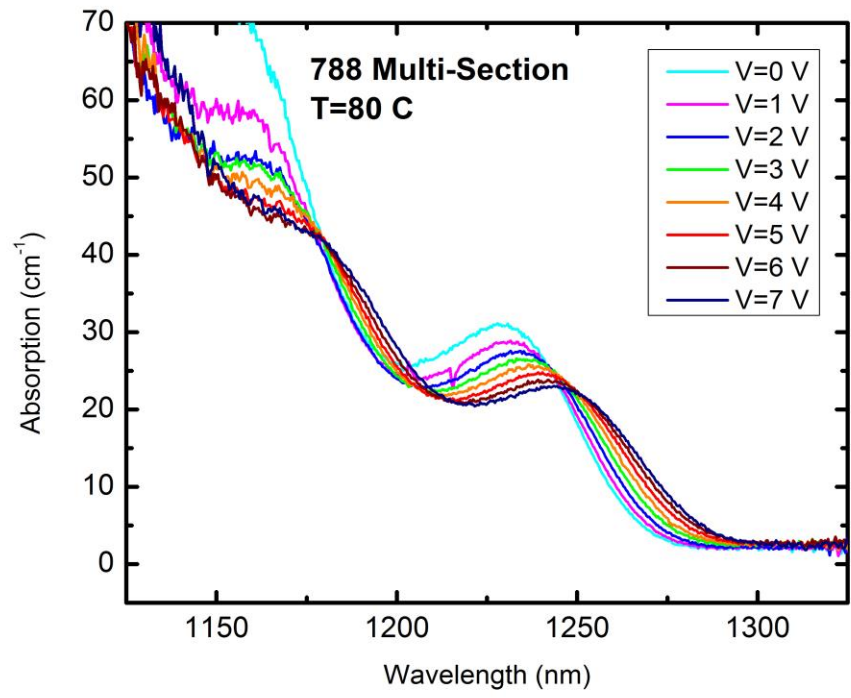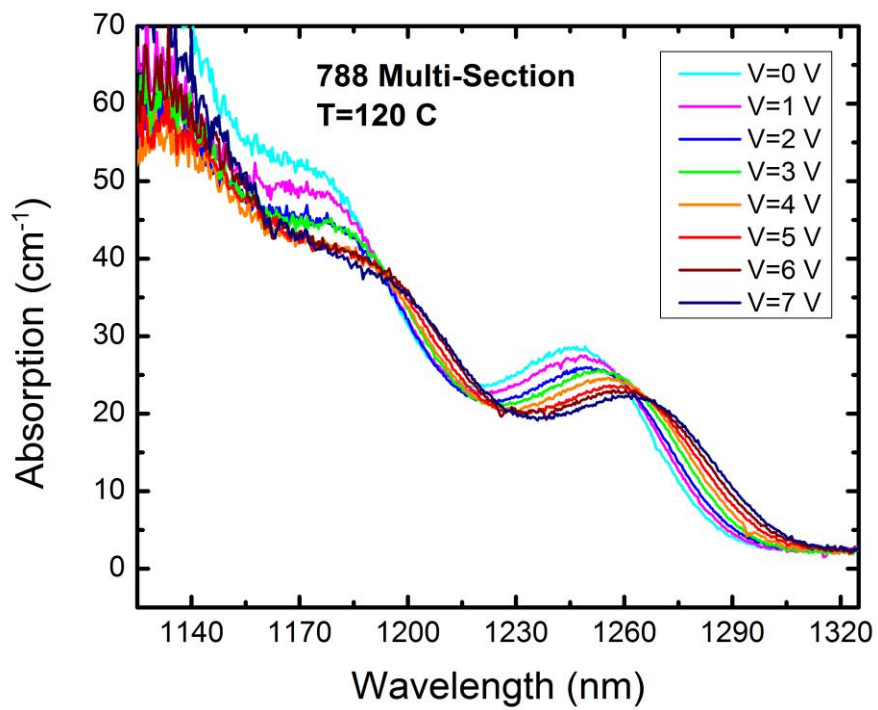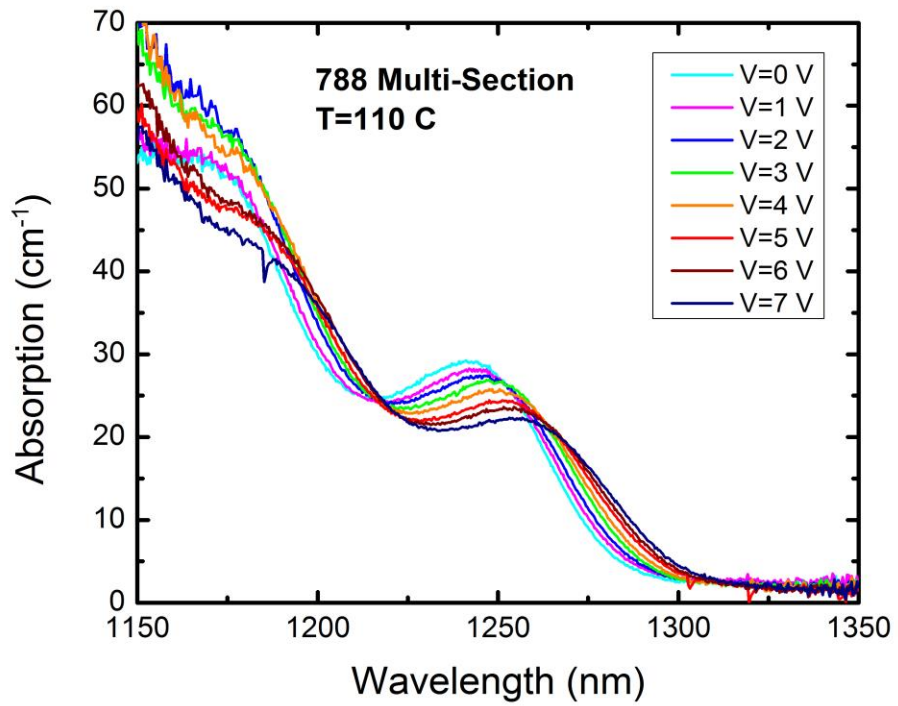
Mode-locked operational maps for saturable absorber voltages of -1 to -7 V
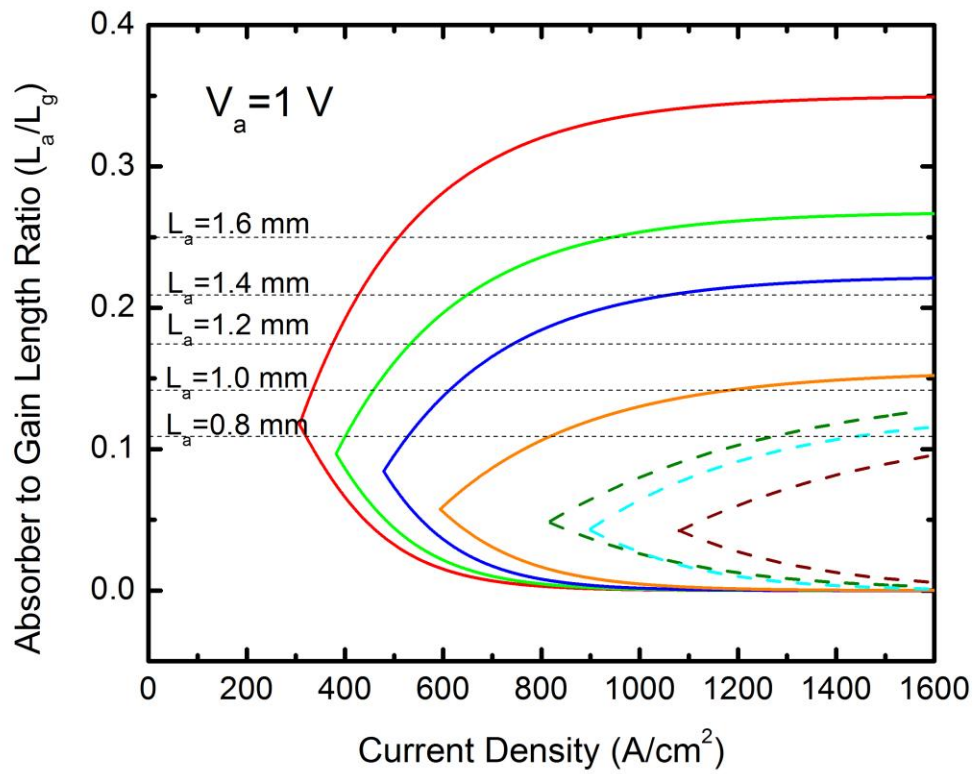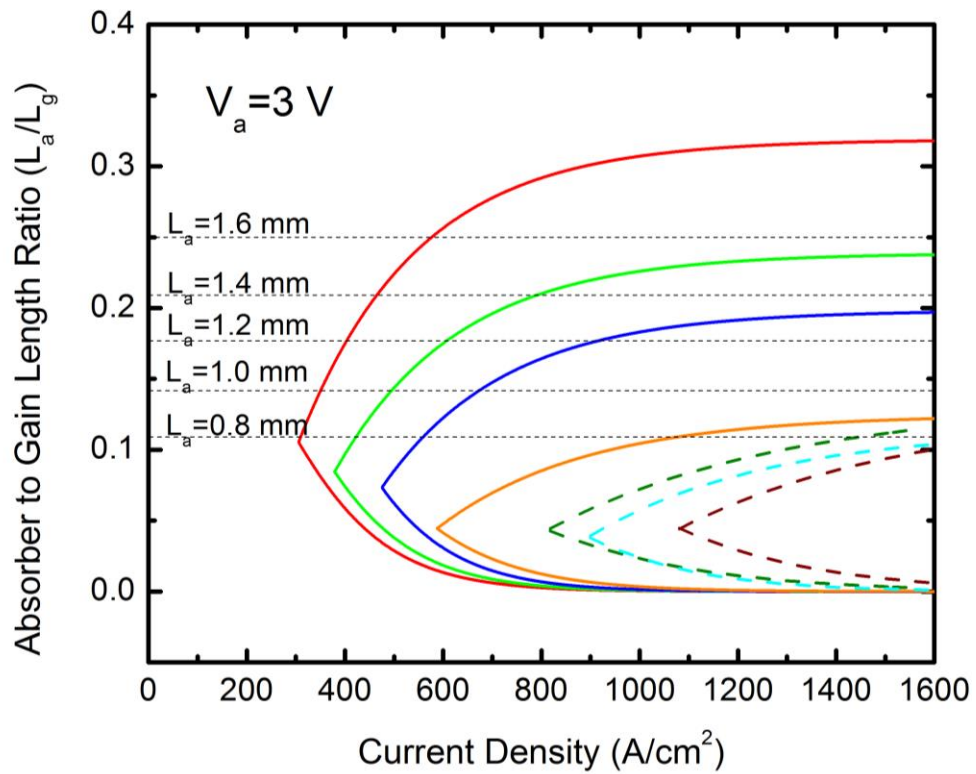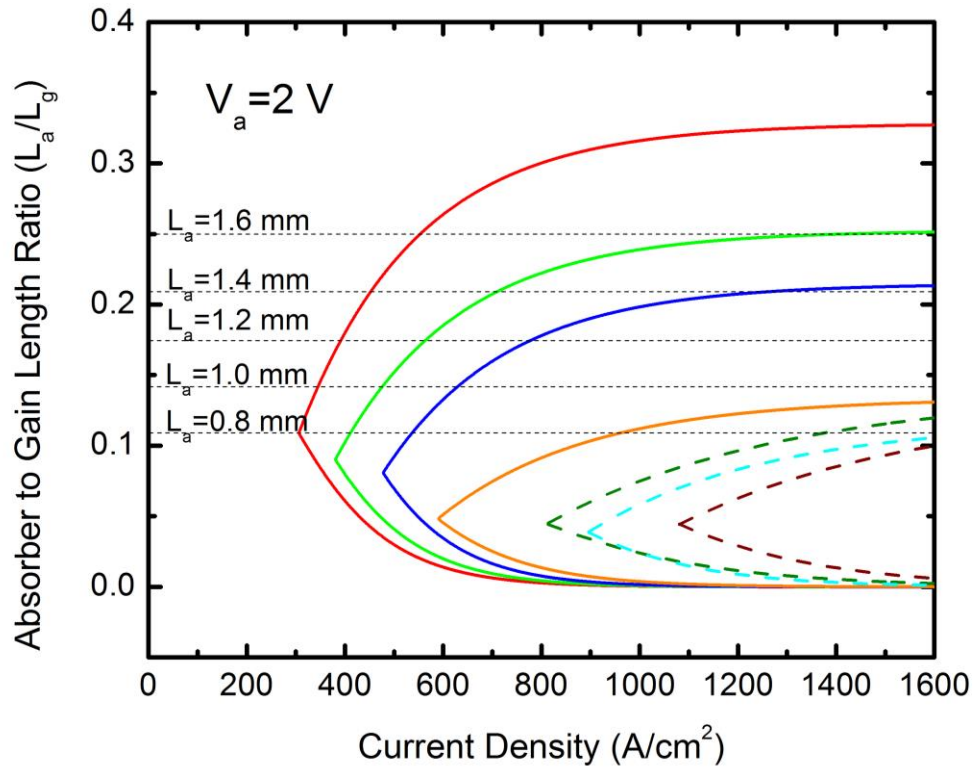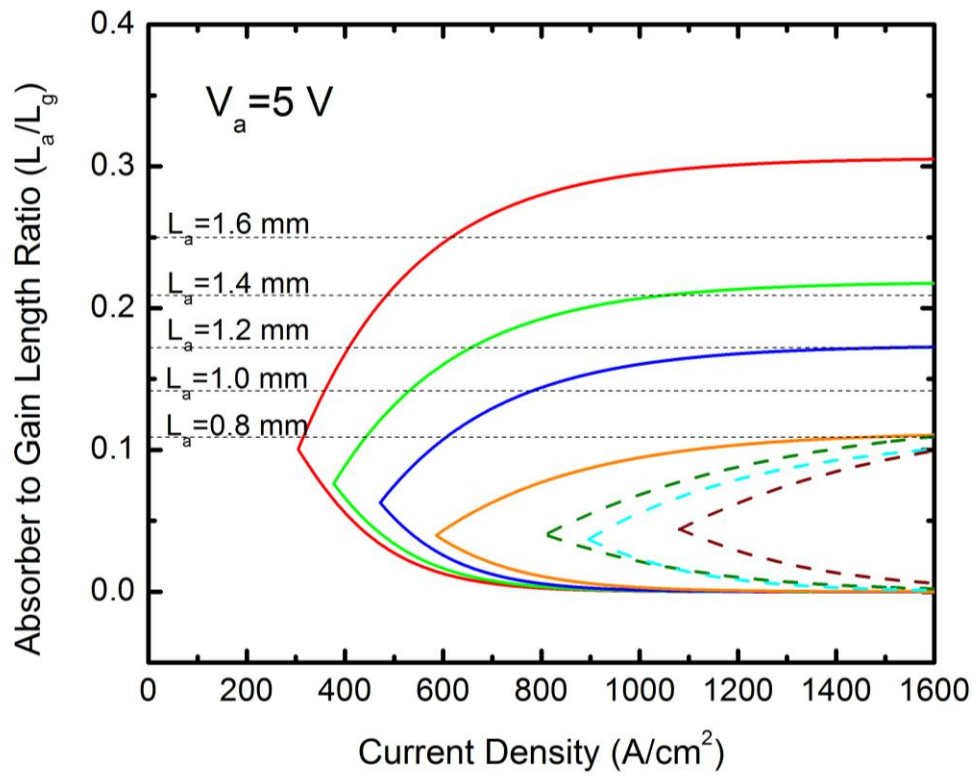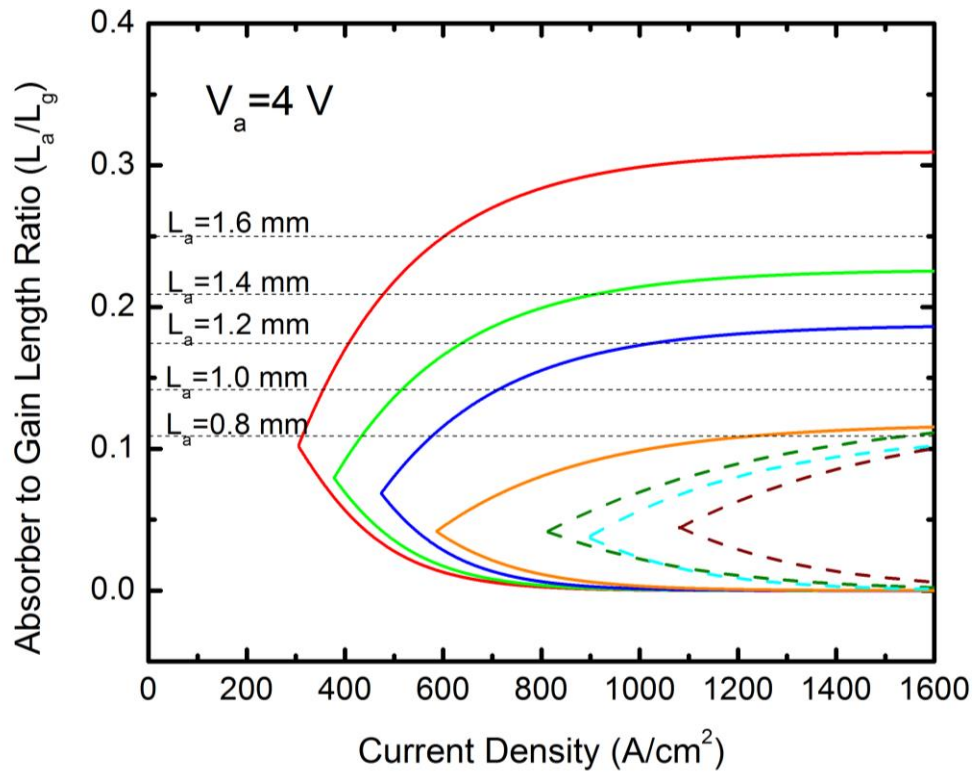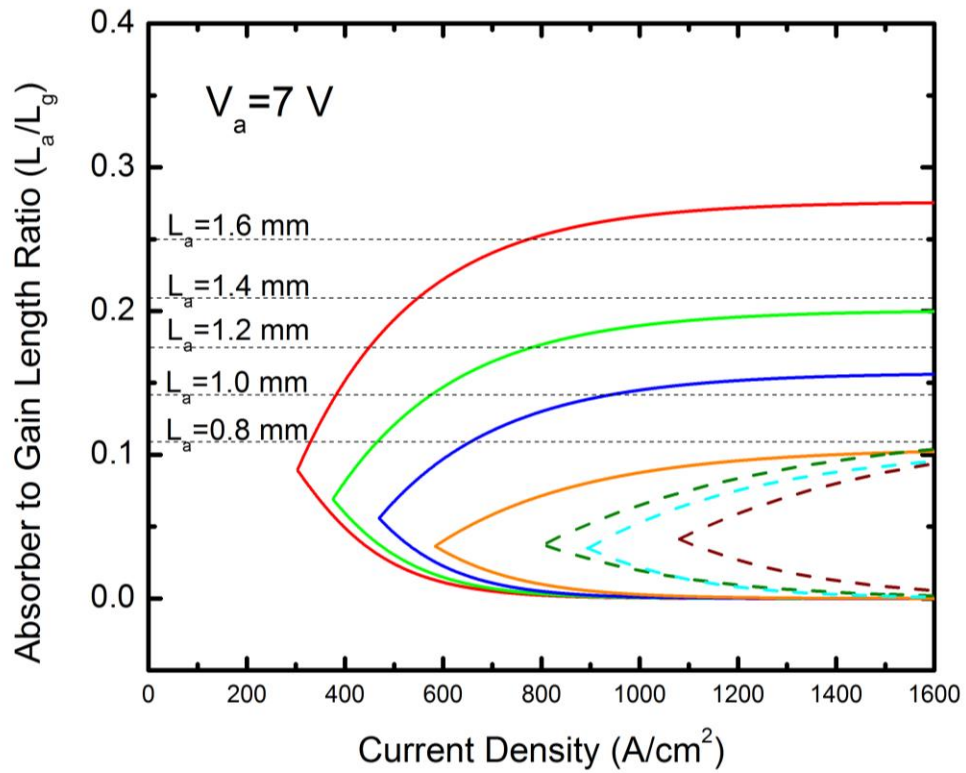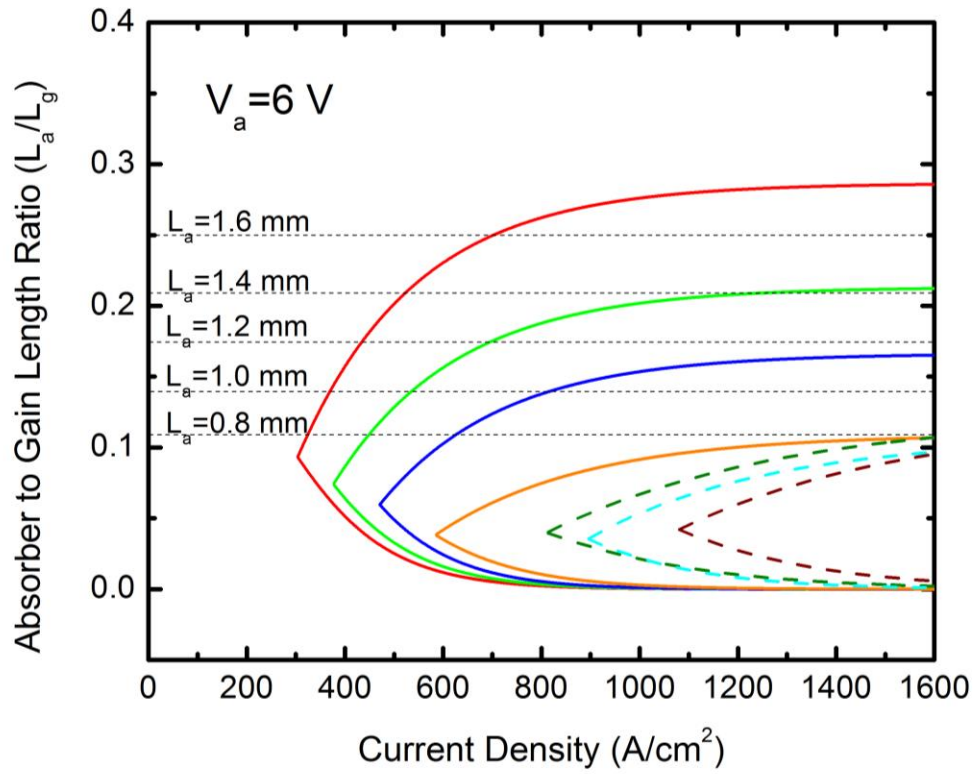
APPENDIX D

Measured temperature dependent optical spectra for the devices having L_a=1.0-mm,

L_a=1.2-mm, L_a=1.4-mm and L_a=1.6-mm

788B AH16 La=1.6-mm